PhD Thesis

MULTIMODAL IMAGING PROBES FOR CANCER DIAGNOSIS AND TREATMENT

Rebecca Rizzo

ACKNOWLEDGEMENTS

Il primo ringraziamento non può che andare al Prof. Enzo Terreno, il quale mi ha permesso di intraprendere questo percorso quasi quattro anni fa e di lavorare con lui. Lo ringrazio soprattutto perché mi ha permesso di esprimere liberamente le mie opinioni, di gestire autonomamente il mio lavoro, essendo comunque presente, facendomi così acquisire indipendenza e senso critico. Lo ringrazio perché non mi ha mai impedito di fare le esperienze che pensavo fossero importanti per la mia carriera, supportandomi sempre.

Ringrazio i miei colleghi e amici per aver reso questi anni leggeri e spensierati. Li ringrazio per le chiacchere, le lamentele che ci hanno alleggerito, i thè delle 17.00 e i biscotti.

Ringrazio il dott. Calogero D'Alessandria che mi ha permesso di trascorrere quasi sette mesi presso il suo gruppo di ricerca a Monaco, facendomi sentire sempre la benvenuta. Lo ringrazio perché mi ha fatta sentire sempre un po' a casa nonostante la lontananza.

Infine, ma non per importanza, non posso che ringraziare la mia Famiglia, nel senso più ampio del termine. Grazie per avermi sempre supportata in questa mia scelta, per sostenermi, per essere pazienti nonostante i miei continui cambi d'opinione. Grazie per avermi concesso il lusso di farlo. Semplicemente, grazie per *esserci*.

Università degli Studi di Torino

Dipartimento di Biotecnologie Molecolari e Scienze della Salute

Dottorato di Ricerca in Scienze Farmaceutiche e Biomolecolari

XXXVI Ciclo

MULTIMODAL IMAGING PROBES FOR CANCER DIAGNOSIS AND TREATMENT

Candidata
Dott.ssa Rebecca Rizzo

Tutor
Prof. Enzo Terreno

Coordinatore della Scuola di Dottorato
Prof.ssa Roberta Cavalli

Anni Accademici 2020-2023

Chapter 1

Chapter 2

Chapter 3

AIM

This doctoral thesis aims to explore the Molecular Imaging applications for Positron Emission Tomography (PET), Optical Imaging (OI) and Computed Tomography (CT).

In **Chapter 1**, the Bi-HPDO3A complex application as CT contrast agent was explored in healthy mice for kidney imaging purposes. After synthesis, the cell viability was checked, the stability was investigated and the CT imaging performances were explored.

In **Chapter 2**, PET application of AAZTA-derived FAP (Fibroblast Activation Protein) inhibitor will be discussed. The gallium 68-radiolabelling protocol was assessed, the stability was checked and the *in vitro* FAP binding was investigated.

In **Chapter 3**, Fluorescence Imaging (FLI) application of IRDye800CW and FNIRTag near-infrared fluorescent dyes based on FAPI-46 FAP inhibitor will be investigated. The spectrophotometric and fluorimetric characteristics of the synthetized fluorescent dyes were explored, as well as the stability and the *in vitro* uptake on FAP-expressing cells. The albumin binding *in vitro* was measured and the *in vivo* fluorescence imaging on breast cancer murine model was conducted.

Fundamentals concerning CT, PET, FLI, FAP-targeting imaging tracers are briefly reported in the **Introduction** part.

INTRODUCTION

Molecular Imaging is the visualization, characterization, and measurement of biological processes at the molecular and cellular levels in humans and other living systems[1]. Molecular imaging represents a multidisciplinary aid to medicine that involves, but not limited to, biological, chemical, physical, engineering, informatics contribution[2]. Beyond the different definitions, molecular imaging allows the visualization of complex biochemical processes involved in normal physiology and disease states, in real time, in living cells, tissues, and intact subjects[3]. The cooperation among different imaging modalities in the form of multimodal imaging approach has provided a great advance in early diagnosis, treatment, therapy response and follow-up. However, early cancer diagnosis and complete tumor resection remain the best options for some patient’s outcomes.

Molecular imaging involves five imaging modalities, including X-ray computed tomography imaging (CT), optical imaging (OI), radionuclide imaging (involving PET and SPECT), ultrasound (US) imaging and magnetic resonance imaging (MRI)[4]. This doctoral thesis aims to explore the Molecular Imaging applications in Positron Emission Tomography, Optical Imaging and Computed Tomography.

Molecular Imaging and cancer

Cancer management is indissolubly linked to biomedical imaging techniques, from diagnosis[5], to image guided treatment[6], to therapy response[7,8] or personalized medicine adjustments[3,9]. Although the last improvements in imaging modalities sensitivity and resolution thanks to the tumor-targeted contrast agents use, in 2020 cancer remained the second leading cause of death after heart diseases[10]. Hence, the development of new molecular imaging probes still represents a hot topic in the cancer management field. While conventional diagnostic and therapeutic approaches have predominantly focused on tumor cells, it is increasingly recognized that the tumor stroma, a component of the tumor microenvironment (TME), plays a crucial role in cancer development and progression[11].

Positron Emission Tomography (PET)

Positron Emission Tomography is one of the most used molecular imaging modalities in current clinical routine[12]. For PET purposes, a radiopharmaceutical in nanomolar concentrations is intravenously injected into the patient. The administered radio-agent contains a positron-emitter such as ^{18}F or ^{68}Ga, an unstable radionuclide that decays to a more stable state emitting positrons (β^+). Because of positrons-electrons interactions in the surrounding tissues, two 511 keV ɣ-rays 180° apart are emitted and then detected from a PET camera. The detector surrounding the subject is designed to detect the signal and convert the resulting electrical signal into sinograms that are rebuilt into tomographic images[13] (**Figure 1**).

Because of its high sensitivity of $10^{-11} \sim 10^{-12}$ mol/L, limitless depth of penetration, and quantitative capabilities, PET represents a powerful tool for clinical diagnosis and basic research including neurology, cardiology, and oncology[4] (**Figure 2**). In the clinic, PET is crucial for cancer detection and staging, as well as evaluation of response to therapy.

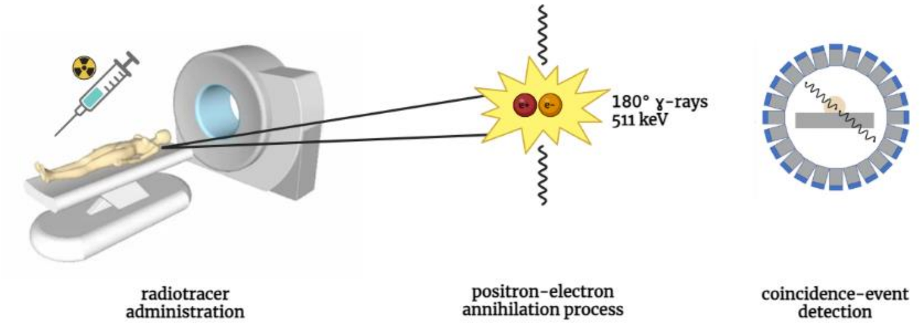

Figure 1 Schematic representation of PET functioning.

^{18}F-FDG ([18F]-2-fluoro-2-deoxy-D-glucose) is undoubtedly the main PET agent used routinely. ^{18}F-FDG is a glucose analogue that is taken into cells by glucose transporters. After phosphorylation into the cell, it cannot cross the cell membrane again or continue through the glycolytic pathway. Since increased glucose metabolism is seen in certain disease processes, such as many malignant tumors or inflammation due to overexpression of glucose transporters, and higher levels of hexokinase, ^{18}F-FDG accumulation enables tumor PET imaging[12]. Although ^{18}F-

FDG PET represents the standard of care in cancer diagnosis, staging and therapy response assessment, there is the need for further information. In fact, ^{18}F-FDG is not tumor selective, the early stage of metastasis cannot be visualized since tiny amount of tumor cells in the niche[15] and tissue with a high FDG uptake background such as the brain may cause difficulties in image interpretation[16].

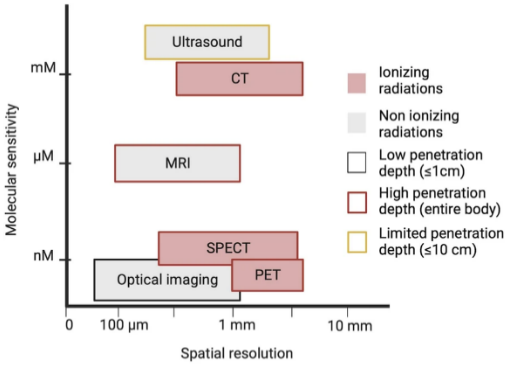

Figure 2 The graph shows the sensitivity and spatial resolution ranges of the different imaging modalities. Adapted from Bortot *et al*. [14] (*J. Nanobiotechnology* **21**, 1–23 (2023)).

Because of these undeniable findings, several tumor-targeted tracers have been developed and compared head-to-head with FDG; with regards to the hallmarks of cancer, they can be divided into different groups such as hypoxia[17], angiogenesis[18], treatment specific tracers[19], metabolism[20], tracers targeting the tumor microenvironment[21], proliferation[22].

As object of this doctoral thesis, FAP-targeting imaging tracers, part of the tracers targeting the tumor microenvironment, will be discussed further in the specific sub-chapter.

Optical Imaging (OI)

Optical Imaging has been increasingly establishing as pivotal clinical imaging technique[23]. Over the past several years, the field of pre-operative imaging techniques (radiography, CT, MRI, PET, SPECT) has made notable progresses, but these methodologies are mainly not applicable to intraoperative tumor surgery. Palpation and visual inspection remain the predominant methods for surgeons to deal with tumor surgery however, positive margins are detected in 20-40% of patients after BCS (breast-conserving surgery) procedures, necessitating additional surgical intervention and resulting in inconvenience to the patient and additional expense to the national health care system[24]. Thus, intraoperative molecular imaging offers a much more straightforward perspective to locate tumors in fluorescence guided surgery (FGS), enabling support to the surgeon with real-time response on tumor site and margin status[25].

Briefly, Fluorescence Imaging requires the administration of a fluorescent molecules that, properly excited with a laser with a specific wavelength, emits fluorescence radiations collected by a sensitive camera (**Figure 3**). Tumor-targeted, near-infrared fluorescent (NIRF) imaging is an emerging field of real-time intraoperative cancer imaging based on tumor-targeted NIRF dyes and it has become relevant also in breast cancer as demonstrated from clinical trials largely in phase 1-2[26]. The use of near-infrared light has allowed a qualitative leap in the field because of deeper penetration in the tissues (millimeters up to centimeters)[27] and almost no-autofluorescence of the tissues in the NIR (Near-Infrared) region[28].

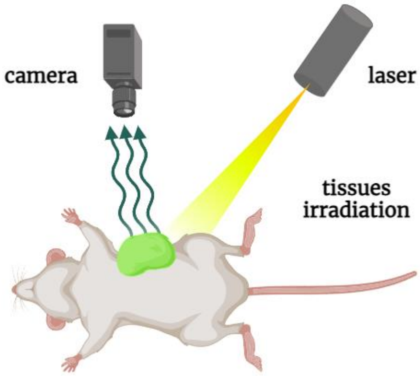

Figure 3 Schematic representation of fluorescence imaging (FLI) functioning.

Non-specific fluorescent agents, used for the assessment of blood flow and sentinel lymph node detection, have so far dominated the field[29]. Indocyanine green (ICG), methylene blue (MB) and 5-ALA are the only NIR fluorescent dyes approved by the FDA (chemical structures reported in **Figure 4**). Among them, ICG and MB provide contrast via passive mechanisms and 5-ALA, just clinically approved in 2017, enables targeted fluorescence imaging of cancer. ICG has been used as a contrast agent for intraoperative fluorescence imaging of different cancers thanks to Enhanced Permeability Retention (EPR) effect[30]. MB allows the visualization of neuroendocrine tumors[31], stains parathyroid glands and

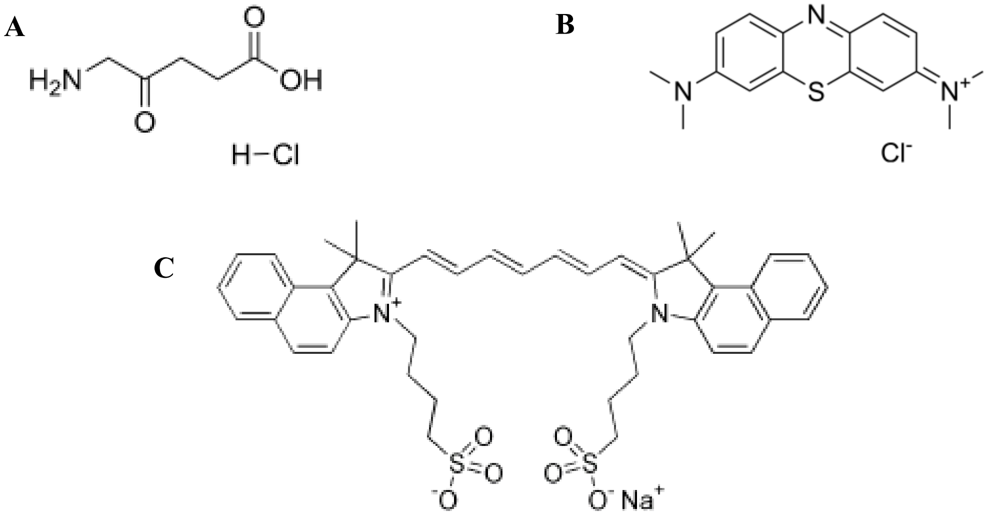

Figure 4 Chemical structures of (A) 5-ALA HCl (5-aminolevulinic acid hydrochloride), (B) MB (chloride salt) and (C) ICG (sodium salt).

insulinomas[32]. 5-ALA has improved high grade glioma complete resection rates almost two-fold over white light imaging alone, resulting in increased overall progression free survival[33]. However, unbound tracers can lead to nonspecific background fluorescence and decreased signal-to-background ratios. Hence, new advanced targeting FGS contrast agents are needed[34].

Currently, the two most common classes of biological targets studied are cancer associated surface receptors and enzymes[23]. For this purpose, fluorescent dyes are chemically conjugated with targeting moieties such as peptides, antibodies, or sugars, which are systemically metabolized and accumulate in lesion sites. These fluorescent dyes show potential as markers of cancer cells, tumor angiogenesis, and tumor microenvironments[35].

Organic fluorescent dyes can be distinguished by their molecular structures as coumarins, boron dipyrromethene, naphthalimides, benzothiazoles, rhodamines, and cyanines. Among these, cyanine dyes have longer absorption and emission wavelengths due to their rigid plane, push–pull electronic structure, and high conjugation. One of the most common ways to categorize cyanines follows the length of their polymethine chains[36]: monocyanines, trimethylcyanines, pentamethine cyanines, heptamethine cyanines, and so on. Because of their spectral properties, heptemethine cyanine dyes (Cy7) are advantageous in biological applications (**Figure 5**). Due to its benefits, NIR absorbing/emitting probes have found extensive applications in medical science for preclinical imaging, diagnostics, and fluorescence-guided surgery (FGS).

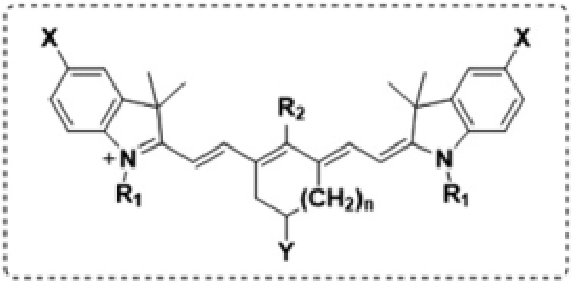

Figure 5 General structural formula of the heptamethine cyanine dye. Adapted from Feng *et al. Org. Biomol. Chem.* **18**, 9385–9397 (2020).

Imaging with fluorophores that emit in the NIR-I window (700-950 nm) provides a resolution on a micron scale at a depth of 0.2 mm, whereas NIR-II (950-1700 nm) emitting probes at 1-3 mm depth[37]. Improved tissue deep penetration, low background noise/auto-fluorescence from cellular materials and solvent (water), and great spatial and temporal resolution represent the main reasons for the great interest in the NIR region in the biomedical field[38].

Fluorophore conjugation is not without pitfalls and often alters the properties of both the fluorophore and the molecule to which it is attached[39]. Specifically, important parameters such as brightness, target binding, *in vivo* stability, and pharmacokinetics (PK) are often impacted[40]. Hence, fluorophore spectral properties preservation should not be taken for granted when a novel dye-targeting mojety have developed, thus expecting different properties both *in vitro* and *in vivo*.

FAP-targeting imaging tracers

Fibroblast activation protein is a transmembrane protein part of the DPP4 family[41]. Unique from other members of this enzymatic family, FAP exhibits both endopeptidase and dipeptidyl activities[42]. FAP is able to hydrolyse a prolyl bond that is two amino acids from the N-terminus of a protein or a prolyl bond after glycine-proline residue[43]. In **Figure 6** is reported a schematic representation of cleavage processes by FAP. FAP exhibits its dipeptidyl peptidase activity by cleaving the post-proline amidic bond with proline as the penultimate aminoacid. The endopeptidase activity is showed by cleaving a post-proline bond preferentially to the Gly-Pro-“X” sequence (**Figure 6**), with the most effective cleavage when “X” is Phe (phenylalanine) or Met (methionine) and the least effective one when “X” is His (histidine) or Glu (glutamic acid)[44].

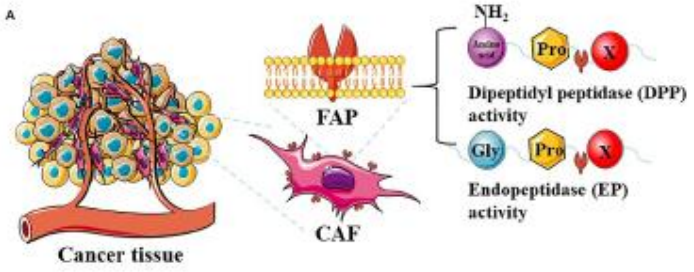

Figure 6 FAP enzymatic activity – adapted from Xin *et al*. *Front. Oncol.* **11**, (2021).

FAP was discovered in 1986 by Wolfgang Rettig using a monoclonal antibody (F19), which reacted with activated fibroblasts *in vitro*[45]. Busek *et al.* later reported that generally FAP is not expressed in healthy adult mammalian tissues, although some FAP$^+$ cells are present in the placenta and uterine stroma[46]. Moreover, FAP expression has been observed during mouse embryogenesis[47] and in the resorbing tadpole tail[48]. These observations suggest a role for FAP in normal developmental processes and tissue remodelling. FAP expression has been observed during wound healing[49] and it is strongly expressed by cancer-associated fibroblasts (CAFs) (**Figure 7**) in the tumor stroma of over 90% epithelial carcinomas[50], including breast[51], colorectal[52], pancreatic[53], lung[54], brain[55], intrahepatic bile duct[56], and

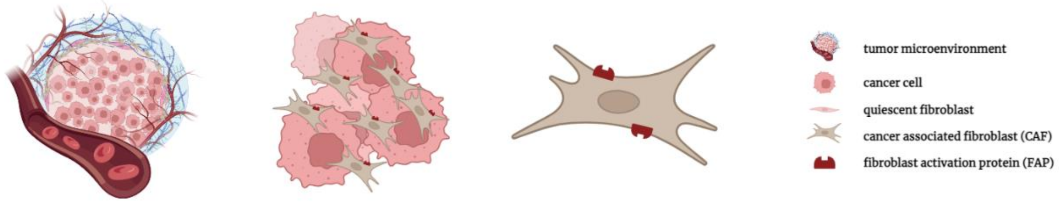

Figure 7 Schematic representation of tumor microenvironment with FAP expression on CAFs.

ovarian cancers[57]. Although several studies have been conducted, the pro-tumor and anti-tumor effect of FAP expression have not been so far entirely elucidated. The cumulative results indicate that FAP expression influences tumor growth by impacting tumor cell proliferation and invasion, angiogenesis, epithelial-to-mesenchymal transition, immunosuppression, and drug resistance[44].

In this context, an extensive effort has been placed on the development of diagnostic and/or therapeutic agents targeting the FAP. Among these, radiopharmaceuticals based on FAP-specific inhibitors (FAPIs) have become of great interest in the theranostic field, by leading to the development of several diagnostic and therapeutic agents.

Different strategies have been investigated for targeting FAP, as antibodies, polypeptides, and inhibitors. Although the first relevant studies on FAPIs date back to the end of the 90's, the first class of selective FAPIs that showed a selectivity index (the ratio between IC_{50} value for FAP and for PREP or DDPIV) > 10^3 for the other enzymes belonging to the same enzymatic family (PREP and DDP IV above all) was identified in 2013 by Jansen and co-workers[58]. Starting from this new class of FAP inhibitors, based on N-(4-quinolinoyl)-Gly-(2-cyanopyrrolidine) scaffold (**Figure 8**)[59], several PET tracers have been developed, showing high tumor/background ratio and FAP specificity *in vivo*.

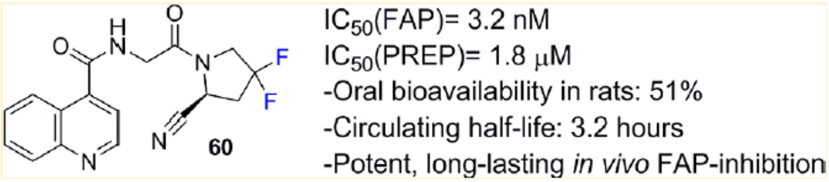

IC_{50}(FAP)= 3.2 nM
IC_{50}(PREP)= 1.8 μM
-Oral bioavailability in rats: 51%
-Circulating half-life: 3.2 hours
-Potent, long-lasting *in vivo* FAP-inhibition

Figure 8 4,4-difluoro substituted 2-cyanopirrolidine ring of N-(4-quinolinoyl)-Gly-(2-cyanopyrrolidine) scaffold represent the most potent class of FAP inhibitor to date. Adapted from Jansen *et al. J. Med. Chem.* **57**, 3053–3074 (2014).

In details, the nitrile group is responsible for the enzymatic active site binding; the difluoro-substitution has found to increase the binding, the quinoline structure ensures the selectivity and the glycine-proline mimics the enzyme substrates. Moreover, the position of both the nitrogen in the quinoline ring and the R substituent (5' position) in the FAPI tracer are pivotal.

The first remarkable FAP-inhibitors for PET purposes were the FAPI-02 and FAPI-04, used as lead compound to further improve the development of this class of probes. Indeed, among several developed FAPI radiotracers, using ^{68}Ga-labeled FAPI, ^{68}Ga-FAPI-04 being the most frequently applied (>60%), followed by ^{68}Ga-FAPI-02 and ^{68}Ga-FAPI-46[60] (structures in **Figure 9**).

Radiolabelled FAPIs have been suggested as a therapeutic target in recent years[61,62], in combination with a broad range of radioisotopes for treatment, such as ^{177}Lu-DOTAGA.(SA.FAPI), ^{177}LuDOTA.SA.FAPI, ^{225}Ac-FAPI-04, ^{153}Sm-FAPI-46, ^{90}Y-FAPI-04 (structures in **Figure 9**) and many more[11]. In the field of nuclear medicine, the radioisotopes mentioned above act as therapeutics because of β- radiations (^{177}Lu,^{90}Y,^{153}Sm) or alpha particles (^{225}Ac) emitted by unstable radionuclides.

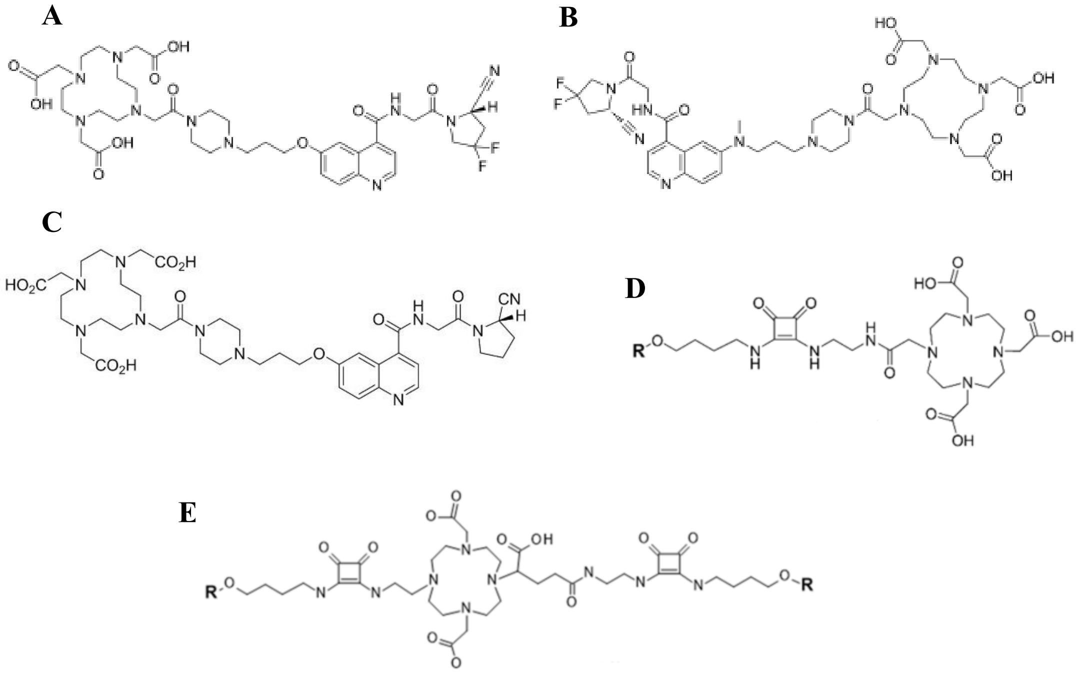

Figure 9 Chemical structures of (A) FAPI-04, (B) FAPI-46, (C) FAPI-02, (D) DOTA.SA.FAPI and (E) DOTAGA.(SA.FAPI)$_2$.

Computed Tomography (CT)

CT remains the diagnostic imaging technique of choice for diverse clinical questions, from trauma events to cancer management, owing to its wide availability, high efficiency and low cost[63]. Moreover, CT is used as morphological support to nuclear medicine in the development of hybrid imaging systems such as PET/CT and SPECT/CT.

A CT system consists of an X-ray source and X-ray detector, between which the subject is placed. As the result of collision between accelerated electrons across a high voltage and an anode composed of a high atomic number material (commonly tungsten), X-rays are produced with a broad energy spectrum[64]. After travelling through the subject, not-absorbed X-rays reach the detector (**Figure 10**).

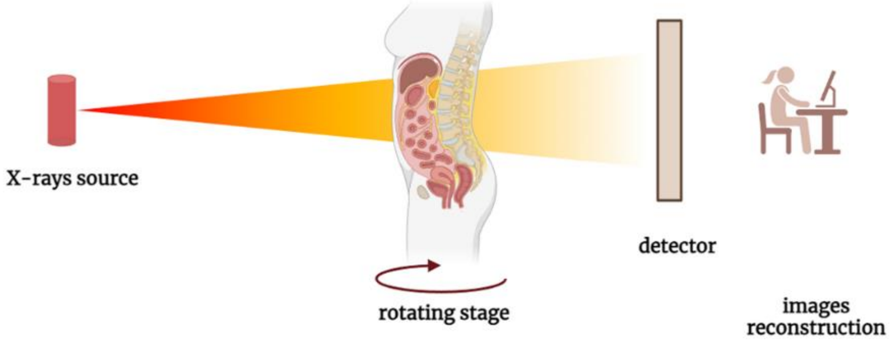

Figure 10 Schematic representation of CT functioning.

The absorption of X-rays is dependent on the thickness of the material and on the material-dependent attenuation coefficient[2].

The main limitation of CT is its low sensitivity to image soft tissues which are devoid of high atomic number atoms, thus a contrast agent is desirable. Current CT contrast agents are based on high-Z elements and may be classified in two major categories: small molecular agents and nanoparticulate agents.

Molecule-based contrast agents (ionic or non-ionic) mainly relied on iodine atoms (Z=53); in medical applications, iohexol, iopamidol, iosimenol, iodixanol, and iotrolan are used. Nanosized agents have been developed to increase the blood residence time, then are called "blood-pool" agents and include nanosuspensions, nanoemulsions, microspheres, liposomes, micelles, polymeric particles, nanospheres, and nanocapsules[65].

Although iodine has historically represented the first choice in CT imaging field, clinically employed iodinated contrast agents suffer from low sensitivity, poor spectral CT, potential allergy, and renal toxicity[66–68]. Hence, the development of improved CT contrast agents is still subject matter of interest. To date, the development of Bi-based CT agents is mostly focused on the design of nanosized systems because of their superior contrast, higher circulation times and versatility for targeting purposes[69]. Remarkable examples are the Bi_2S_3 nanoparticles labelled with the cyclic nine amino acids peptide LyP-1 for targeting breast cancer[66] and the MUC-16 aptamer targeted Bi-DOTA-PEG nanoparticles to image cervical cancer[67]. However, despite the promising preclinical results, no clinical translation has been reported so far for nanoparticulate agents, unlike small metal chelate-based contrast agents. On the other side, Bi-based small molecules have not been sufficiently emphasized, with just a few examples reported, such as Bi-DPTA[70] and Bi-DOTA[71].

CT is the latest molecular imaging technique to be included in the field because of the lack of targeted and specific imaging agents developed. The primary limitation for CT in molecular imaging applications is the quantity of imaging agent reaching the target sites causing an X-ray attenuation[3]. However, several examples of CT molecular imaging agents have been developed in the recent years. As early as 2008, Popovtzer *et al.* developed immuno-targeted gold nanoprobes[72] in an *in vitro* proof of principle demonstration for head and neck cancer. By functionalizing the surface of gold nanoparticles (GNPs) with a prostate-specific membrane antigen (PSMA) RNA aptamer that binds to PSMA, Kim *et al.* established a multifunctional nanoparticle for targeted molecular CT imaging and therapy of prostate cancer[73]. In 2018, a new class of ABPs (activity-based probes) attached to iodinated polymeric dendrimers for detection of solid tumors using X-ray CT was developed by Gaikwad and co-workers[74]. Hence, the need of specifically targeting disease biomarkers is the driving force to the development of new CT molecular imaging contrast agents.

References

[1] S.H. Crayton, A.K. Chen, J.F. Liu, E.M. Higbee-Dempsey, C.H. Huang, A. Tsourkas, Z. Cheng, 3.20 Molecular imaging, Compr. Biomater. II. (2017) 424–466.

[2] M.F. Kircher, J.K. Willmann, Molecular body imaging: MR imaging, CT, and US. Part I. Principles, Radiology. 263 (2012) 633–643.

[3] M.L. James, S.S. Gambhir, A molecular imaging primer: Modalities, imaging agents, and applications, Physiol. Rev. 92 (2012) 897–965.

[4] Z.Y. Chen, Y.X. Wang, Y. Lin, J.S. Zhang, F. Yang, Q.L. Zhou, Y.Y. Liao, Advance of molecular imaging technology and targeted imaging agent in imaging and therapy, Biomed Res. Int. 2014 (2014).

[5] J. V. Frangioni, New technologies for human cancer imaging, J. Clin. Oncol. 26 (2008) 4012–4021.

[6] C. Li, Z. Ding, Y. Han, Mn-Doped Nano-Hydroxyapatites as Theranostic Agents with Tumor pH-Amplified MRI-Signal Capabilities for Guiding Photothermal Therapy, Int. J. Nanomedicine. 18 (2023) 6101–6118.

[7] J. Hunger, K. Schregel, B. Boztepe, D.A. Agardy, V. Turco, I. Weidenfeld, Y. Streibel, M. Fischer, V. Sturm, R. Santarella-mellwig, T. Bunse, M. Bendszus, M. Platten, M.O. Breckwoldt, In vivo nanoparticle-based T cell imaging can predict therapy response towards adoptive T cell therapy in experimental glioma, Theranostics. 13 (2023).

[8] A. Puyalto, M. Rodríguez-Remírez, I. López, F. Iribarren, J.A. Simón, M. Ecay, M. Collantes, A. Vilalta-Lacarra, A. Francisco-Cruz, J.L. Solórzano, S. Sandiego, I. Peñuelas, A. Calvo, D. Ajona, I. Gil-Bazo, A novel [89Zr]-anti-PD-1-PET-CT to assess response to PD-1/PD-L1 blockade in lung cancer, Front. Immunol. 14 (2023) 1–11.

[9] Y. Wang, J.N. Staudinger, T.L. Mindt, G. Gasser, Theranostics with photodynamic therapy for personalized medicine : to see and to treat, Theranostics. 13 (2023).

[10] R.L. Siegel, K.D. Miller, N.S. Wagle, A. Jemal, Cancer statistics, 2023, CA. Cancer J. Clin. 73 (2023) 17–48.

[11] B.M. Privé, M.A. Boussihmad, B. Timmermans, W.A. van Gemert, S.M.B. Peters, Y.H.W. Derks, S.A.M. van Lith, N. Mehra, J. Nagarajah, S. Heskamp, H. Westdorp, Fibroblast activation protein-targeted radionuclide therapy: background, opportunities, and challenges of first (pre)clinical studies, Eur. J. Nucl. Med. Mol. Imaging. 50 (2023) 1906–1918.

[12] Dr . Ur Metser Dr . Amit Singnurkar Dr. Noam Tau, Medical Imaging for Health Professionals: Technologies and Clinical Applications, First, John Wiley & Sons, Inc, 2019.

[13] M.E. Phelps, Positron emission tomography provides molecular imaging of biological processes, Proc. Natl. Acad. Sci. U. S. A. 97 (2000) 9226–9233.

[14] B. Bortot, A. Mangogna, G. Di Lorenzo, G. Stabile, G. Ricci, S. Biffi, Image-guided cancer surgery: a narrative review on imaging modalities and emerging nanotechnology strategies, J. Nanobiotechnology. 21 (2023) 1–23.

[15] F. Ding, C. Huang, C. Liang, C. Wang, J. Liu, D. Tang, 68Ga-FAPI-04 vs. 18F-FDG in a

longitudinal preclinical PET imaging of metastatic breast cancer, Eur. J. Nucl. Med. Mol. Imaging. 49 (2021) 290–300.

[16] U. Haberkorn, A. Markert, W. Mier, V. Askoxylakis, A. Altmann, Molecular imaging of tumor metabolism and apoptosis, Oncogene. 30 (2011) 4141–4151.

[17] D. Hanahan, R.A. Weinberg, Hallmarks of Cancer: The Next Generation, Cell. 144 (2011) 646–674.

[18] J. Liu, L. Wu, Z. Liu, S. Seery, J. Li, Z. Gao, J. Yu, X. Meng, 18F-RGD PET/CT and Systemic Inflammatory Biomarkers Predict Outcomes of Patients With Advanced NSCLC Receiving Combined Antiangiogenic Treatment, Front. Oncol. 11 (2021) 671912.

[19] A.A. Memon, B. Weber, M. Winterdahl, S. Jakobsen, P. Meldgaard, H.H.T. Madsen, S. Keiding, E. Nexo, B.S. Sorensen, PET imaging of patients with non-small cell lung cancer employing an EGF receptor targeting drug as tracer, Br. J. Cancer 2011 10512. 105 (2011) 1850–1855.

[20] D. Hanahan, Hallmarks of Cancer: New Dimensions, Cancer Discov. 12 (2022) 31–46.

[21] S. Ballal, M.P. Yadav, V. Kramer, E.S. Moon, F. Roesch, M. Tripathi, S. Mallick, S.T. ArunRaj, C. Bal, A theranostic approach of [68Ga]Ga-DOTA.SA.FAPi PET/CT-guided [177Lu]Lu-DOTA.SA.FAPi radionuclide therapy in an end-stage breast cancer patient: new frontier in targeted radionuclide therapy, Eur. J. Nucl. Med. Mol. Imaging. (2020) 1–3.

[22] M. Peck, H.A. Pollack, A. Friesen, M. Muzi, S.C. Shoner, E.G. Shankland, J.R. Fink, J.O. Armstrong, J.M. Link, K.A. Krohn, Applications of PET imaging with the proliferation marker [18F]-FLT, Q. J. Nucl. Med. Mol. Imaging. 59 (2015) 95–104.

[23] D. Seah, Z. Cheng, M. Vendrell, Fluorescent Probes for Imaging in Humans: Where Are We Now?, ACS Nano. 17 (2023) 19478–19490.

[24] R.G. Pleijhuis, M. Graafland, J. De Vries, J. Bart, J.S. De Jong, G.M. Van Dam, Obtaining adequate surgical margins in breast-conserving therapy for patients with early-stage breast cancer: Current modalities and future directions, Ann. Surg. Oncol. 16 (2009) 2717–2730.

[25] C. Chi, Y. Du, J. Ye, D. Kou, J. Qiu, J. Wang, J. Tian, X. Chen, Intraoperative imaging-guided cancer surgery: From current fluorescence molecular imaging methods to future multi-modality imaging technology, Theranostics. 4 (2014) 1072–1084.

[26] M. Kedrzycki, M. Leiloglou, P. Thiruchelvam, D. Elson, D. Leff, Fluorescence guided surgery in breast cancer: A systematic review of the literature, Eur. J. Surg. Oncol. 47 (2021) e309.

[27] B. Chance, Near-infrared images using continuous, phase-modulated, and pulsed light with quantitation of blood and blood oxygenation, Ann. N. Y. Acad. Sci. 838 (1998) 29–45.

[28] J. V. Frangioni, In vivo near-infrared fluorescence imaging, Curr. Opin. Chem. Biol. 7 (2003) 626–634.

[29] P. Debie, S. Hernot, Emerging fluorescent molecular tracers to guide intra-operative surgical decision-making, Front. Pharmacol. 10 (2019).

[30] L. van Manen, H.J.M. Handgraaf, M. Diana, J. Dijkstra, T. Ishizawa, A.L. Vahrmeijer, J.S.D. Mieog, A practical guide for the use of indocyanine green and methylene blue in fluorescence-guided abdominal surgery, J. Surg. Oncol. 118 (2018) 283–300.

[31] H.A. Galema, T.M. Van Ginhoven, G.J.H. Franssen, J. Hofland, C.G.O.T. Bouman, C. Verhoef, A.L. Vahrmeijer, M. Hutteman, D.E. Hilling, S. Keereweer, Fluorescence-guided surgery using methylene blue to improve identification of metastatic small intestinal neuroendocrine tumours, Br. J. Surg. 110 (2023) 541–544.

[32] C.J.H. van de Alexander L. Vahrmeijer, Merlijn Hutteman, Joost R. van der Vorst, and J.V.F. Velde, Image-guided cancer surgery using near-infrared fluorescence, Nat Rev Clin Oncol. 10 (2013) 507–518.

[33] T. Picart, M. Berhouma, C. Dumot, J. Pallud, P. Metellus, X. Armoiry, J. Guyotat, Optimization of high-grade glioma resection using 5-ALA fluorescence-guided surgery: A literature review and practical recommendations from the neuro-oncology club of the French society of neurosurgery, Neurochirurgie. 65 (2019) 164–177.

[34] C.W. Barth, S. Gibbs, Fluorescence image-guided surgery: a perspective on contrast agent development, Proc. SPIE - Int. Soc. Opt. Eng. (2020) 18.

[35] E.M. Sevick-Muraca, Translation of near-infrared fluorescence imaging technologies: emerging clinical applications, Annu. Rev. Med. 63 (2012) 217–231.

[36] L. Feng, W. Chen, X. Ma, S.H. Liu, J. Yin, Near-infrared heptamethine cyanines (Cy7): From structure, property to application, Org. Biomol. Chem. 18 (2020) 9385–9397.

[37] M. Lyu, D. Zhu, Y. Duo, Y. Li, H. Quan, Bimetallic nanodots for tri-modal CT/MRI/PA imaging and hypoxia-resistant thermoradiotherapy in the NIR-II biological windows, Biomaterials. 233 (2020) 119656.

[38] A. Haque, M.S.H. Faizi, J.A. Rather, M.S. Khan, Next generation NIR fluorophores for tumor imaging and fluorescence-guided surgery: A review, Bioorganic Med. Chem. 25 (2017) 2017–2034.

[39] J. Pauli, M. Grabolle, R. Brehm, M. Spieles, F.M. Hamann, M. Wenzel, I. Hilger, U. Resch-Genger, Suitable labels for molecular imaging - Influence of dye structure and hydrophilicity on the spectroscopic properties of IgG conjugates, Bioconjug. Chem. 22 (2011) 1298–1308.

[40] J.L. Kovar, M.A. Simpson, A. Schutz-Geschwender, D.M. Olive, A systematic approach to the development of fluorescent contrast agents for optical imaging of mouse cancer models, Anal. Biochem. 367 (2007) 1–12.

[41] J. Park, K. Ajami, D.M.T. Yu, M.D. Gorrell, Dipeptidyl peptidase 8 has post-proline dipeptidyl aminopeptidase and prolyl endopeptidase activities, Adv. Exp. Med. Biol. 575 (2006) 93–102.

[42] K.N. Lee, K.W. Jackson, S. Terzyan, V.J. Christiansen, P.A. McKee, Using substrate specificity of antiplasmin-cleaving enzyme for fibroblast activation protein inhibitor design, Biochemistry. 48 (2009) 5149–5158.

[43] D.M.T. Yu, T.W. Yao, S. Chowdhury, N.A. Nadvi, B. Osborne, W.B. Church, G.W. McCaughan, M.D. Gorrell, The dipeptidyl peptidase IV family in cancer and cell biology, FEBS J. 277 (2010) 1126–1144.

[44] L. Xin, J. Gao, Z. Zheng, Y. Chen, S. Lv, Z. Zhao, C. Yu, X. Yang, R. Zhang, Fibroblast Activation Protein-α as a Target in the Bench-to-Bedside Diagnosis and Treatment of Tumors: A Narrative Review, Front. Oncol. 11 (2021).

[45] O.L. Rettig WJ, Chesa PG, Beresford HR, Feickert HJ, Jennings MT, Cohen J, Oettgen HF,

Differential expression of cell surface antigens and glial fibrillary acidic protein in human astrocytoma subsets, Cancer Res. 46 (1986) 6406–12.

[46] P. Busek, R. Mateu, M. Zubal, L. Kotackova, A. Sedo, Targeting Fibroblast activation protein in cancer - Prospects and caveats, Front. Biosci. - Landmark. 23 (2018) 1933–1968.

[47] M.T. Levy, G.W. McCaughan, C.A. Abbott, J.E. Park, A.M. Cunningham, E. Muller, W.J. Rettig, M.D. Gorrell, Fibroblast activation protein: A cell surface dipeptidyl peptidase and gelatinase expressed by stellate cells at the tissue remodelling interface in human cirrhosis, Hepatology. 29 (1999) 1768–1778.

[48] D.D. Brown, Z. Wang, J.D. Furlow, A. Kanamori, R.A. Schwartzman, B.F. Remo, A. Pinder, The thyroid hormone-induced tail resorption program during Xenopus laevis metamorphosis, Proc. Natl. Acad. Sci. U. S. A. 93 (1996) 1924–1929.

[49] W.J. Rettig, P. Garin-Chesa, H.R. Beresford, H.F. Oettgen, M.R. Melamed, L.J. Old, Cell-surface glycoproteins of human sarcomas: Differential expression in normal and malignant tissues and cultured cells, Proc. Natl. Acad. Sci. U. S. A. 85 (1988) 3110–3114.

[50] P. Garin-Chesa, L.J. Old, W.J. Rettig, Cell surface glycoprotein of reactive stromal fibroblasts as a potential antibody target in human epithelial cancers, Proc. Natl. Acad. Sci. U. S. A. 87 (1990) 7235–7239.

[51] X. Hua, L. Yu, X. Huang, Z. Liao, Q. Xian, Expression and role of fibroblast activation protein-alpha in microinvasive breast carcinoma, Diagn. Pathol. 6 (2011) 1–7.

[52] J.D.C. Leonard R Henry, Hyung-Ok Lee, John S Lee, Andres Klein-Szanto, Perry Watts, Eric A Ross, Wen-Tien Chen, Clinical implications of fibroblast activation protein in patients with colon cancer, Clin. Cancer Res. 13 (2007) 1736–41.

[53] T.P. Sandberg, M.P.M.E. Stuart, J. Oosting, R.A.E.M. Tollenaar, C.F.M. Sier, W.E. Mesker, Increased expression of cancer-associated fibroblast markers at the invasive front and its association with tumor-stroma ratio in colorectal cancer, BMC Cancer. 19 (2019) 1–9.

[54] K.X. Limin Wang, Limin Cao, Huimin Wang, Boning Liu, Qicheng Zhang, Zhaowei Meng, Xiang Wu, Qinghua Zhou, Cancer-associated fibroblasts enhance metastatic potential of lung cancer cells through IL-6/STAT3 signaling pathway, Oncotarget. 8 (2017) 76116–76128.

[55] J.B.& A.S. Petr Busek, Eva Balaziova, Ivana Matrasova, Marek Hilser, Robert Tomas, Martin Syrucek, Zuzana Zemanova, Evzen Krepela, Fibroblast activation protein alpha is expressed by transformed and stromal cells and is associated with mesenchymal features in glioblastoma, Tumor Biol. 37 (2016) 13961–13971.

[56] R.H. 6 Yuli Lin 1, Bingji Li 2, Xuguang Yang 3, Qian Cai 2, Weiren Liu 4, Mengxin Tian 4, Haoyang Luo 2, Wei Yin 2, Yan Song 2, Yinghong Shi 5, Fibroblastic FAP promotes intrahepatic cholangiocarcinoma growth via MDSCs recruitment, Neoplasia. 21 (2019) 1133–1142.

[57] Z.W. Yuan Zhang 1, Huijuan Tang, Jing Cai, Ting Zhang, Jianfeng Guo, Dilu Feng, Ovarian Cancer- Associated Fibroblasts Contribute to Epithelial Ovarian Carcinoma Metastasis by Promoting Angiogenesis, Lymphangiogenesis and Tumor Cell Invasion, Cancer Lett. 303 (2011) 47–55.

[58] K. Jansen, L. Heirbaut, J.D. Cheng, J. Joossens, O. Ryabtsova, P. Cos, L. Maes, A.M. Lambeir, I. De Meester, K. Augustyns, P. Van Der Veken, Selective inhibitors of fibroblast activation protein (FAP) with a (4-quinolinoyl)-glycyl-2-cyanopyrrolidine scaffold, ACS

Med. Chem. Lett. 4 (2013) 491–496.

[59] K. Jansen, L. Heirbaut, R. Verkerk, J.D. Cheng, J. Joossens, P. Cos, L. Maes, A.M. Lambeir, I. De Meester, K. Augustyns, P. Van Der Veken, Extended structure-activity relationship and pharmacokinetic investigation of (4-quinolinoyl)glycyl-2-cyanopyrrolidine inhibitors of fibroblast activation protein (FAP), J. Med. Chem. 57 (2014) 3053–3074.

[60] S. Taralli, M. Lorusso, E. Perrone, G. Perotti, L. Zagaria, M.L. Calcagni, PET/CT with Fibroblast Activation Protein Inhibitors in Breast Cancer: Diagnostic and Theranostic Application—A Literature Review, Cancers (Basel). 15 (2023) 1–22.

[61] F.L. Giesel, C. Kratochwil, T. Lindner, M.M. Marschalek, A. Loktev, W. Lehnert, J. Debus, D. Jäger, P. Flechsig, A. Altmann, W. Mier, U. Haberkorn, 68 Ga-FAPI PET/CT: Biodistribution and preliminary dosimetry estimate of 2 DOTA-containing FAP-targeting agents in patients with various cancers, J. Nucl. Med. 60 (2019) 386–392.

[62] A. Loktev, T. Lindner, E.M. Burger, A. Altmann, F. Giesel, C. Kratochwil, J. Debus, F. Marmé, D. Jäger, W. Mier, U. Haberkorn, Development of fibroblast activation protein-targeted radiotracers with improved tumor retention, J. Nucl. Med. 60 (2019) 1421–1429.

[63] N. Lee, S.H. Choi, T. Hyeon, Nano-sized CT contrast agents, Adv. Mater. 25 (2013) 2641–2660.

[64] J.R. Ashton, J.L. West, C.T. Badea, In vivo small animal micro-CT using nanoparticle contrast agents, Front. Pharmacol. 6 (2015) 1–22.

[65] H. Lusic, M.W. Grinstaff, X-ray-computed tomography contrast agents, 2013.

[66] O. Rabin, J.M. Perez, J. Grimm, G. Wojtkiewicz, R. Weissleder, An X-ray computed tomography imaging agent based on long-circulating bismuth sulphide nanoparticles, Nat. Mater. 5 (2006) 118–122.

[67] A. Tarighatnia, M.R. Fouladi, M.R. Tohidkia, G. Johal, N.D. Nader, A. Aghanejad, H. Ghadiri, Engineering and quantification of bismuth nanoparticles as targeted contrast agent for computed tomography imaging in cellular and animal models, J. Drug Deliv. Sci. Technol. 66 (2021) 102895.

[68] M.H. Oh, N. Lee, H. Kim, S.P. Park, Y. Piao, J. Lee, S.W. Jun, W.K. Moon, S.H. Choi, T. Hyeon, Large-scale synthesis of bioinert tantalum oxide nanoparticles for X-ray computed tomography imaging and bimodal image-guided sentinel lymph node mapping, J. Am. Chem. Soc. 133 (2011) 5508–5515.

[69] M. Algethami, B. Feltis, M. Geso, Bismuth Sulfide Nanoparticles as a Complement to Traditional Iodinated Contrast Agents at Various X-Ray Computed Tomography Tube Potentials, J. Nanomater. Mol. Nanotechnol. 06 (2017) 2–10.

[70] J.J. Fu, J.J. Guo, A.P. Qin, X.Y. Yu, Q. Zhang, X.P. Lei, Y.G. Huang, M.Y. Chen, J.X. Li, Y. Zhang, J.P. Liu, Y.Y. Dang, D. Wu, X.Y. Zhao, Z.X. Lin, Y.L. Lin, S.P. Li, L.Y. Zhang, Bismuth chelate as a contrast agent for X-ray computed tomography, J. Nanobiotechnology. 18 (2020) 1–10.

[71] G. Dai, Y. Zhang, X. Wang, X. Wang, J. Jia, F. Jia, L. Yang, C. Yang, Small-Molecule Bi-DOTA Complex for High-Performance CT and Spectral CT Bioimaging, Front. Oncol. 12 (2022) 1–11.

[72] R. Popovtzer, A. Agrawal, N.A. Kotov, A. Popovtzer, J. Balter, T.E. Carey, R. Kopelman, N.

Lett Author manuscript, Targeted Gold Nanoparticles enable Molecular CT Imaging of Cancer NIH Public Access Author Manuscript, Nano Lett. 8 (2008) 4593–4596.

[73] D. Kim, Y.Y. Jeong, S. Jon, A drug-loaded aptamer - Gold nanoparticle bioconjugate for combined ct imaging and therapy of prostate cancer, ACS Nano. 4 (2010) 3689–3696.

[74] H.K. Gaikwad, D. Tsvirkun, Y. Ben-Nun, E. Merquiol, R. Popovtzer, G. Blum, Molecular Imaging of Cancer Using X-ray Computed Tomography with Protease Targeted Iodinated Activity-Based Probes, Nano Lett. 18 (2018) 1582–1591.

Chapter 1

Bi-HPDO3A as novel CT contrast agent for X-ray computed tomography

Adapted from: Bi-HPDO3A as novel CT contrast agent for X-ray computed tomography

Rebecca Rizzo, Martina Capozza, Carla Carrera, Enzo Terreno

Sci. Rep. 13 (2023) 1–8.

ABSTRACT

A new bismuth-based CT agent was synthesized through a facile synthesis strategy. The *in vitro* stability, toxicity and CT performance were evaluated. The *in vivo* imaging performance was investigated using three different doses (0.5, 1.2 and 5 mmol/kg) and the result obtained at 1.2 mmol/kg was compared with the clinically approved CT agent iopamidol at the same dosage.

INTRODUCTION

Bismuth is a naturally monoisotopic (^{209}Bi) element that is commonly considered the heaviest stable element of the Periodic Table due to the extremely long theoretical half-life of 1.9×10^{9} years[1]. Over the years, bismuth have found many applications in different fields starting from the preparation of non-toxic pigments and catalysts, the synthesis of biocompatible additives in dental materials[2], and the development of therapeutics against *H. pylori* infections or in the treatments of ulcera gastritis and dyspepsia[3]. More recently, bismuth compounds have also been demonstrated active against coronavirus including both SARSCoV-1 and SARS-CoV-2, through the inhibition of a zinc enzyme helicase[4]. The biomedical applications of Bi were further implemented in the fields of imaging, cancer treatment, drug delivery and biosensing[5]. Beside the natural isotope ^{209}Bi, the artificial ^{212}Bi and ^{213}Bi radioisotopes have been recently attracting interest as potential therapeutic radionuclides in targeted alpha therapy[6]. Especially, the nuclear properties of ^{213}Bi are very suited for dosimetry studies and/or to monitor the biodistribution of the nuclide using single photon emission computed tomography (SPECT)[7]. However, Bi shows the highest X-ray absorption among the heavy metals at any energy of incident X-ray photons, thus making it a perfect candidate for designing X-ray Contrast Agents (XCAs)[8]. Moreover, Bi-compounds exhibit relatively low toxicity, when compared to other heavy metals[5]. Computed Tomography (CT) has been widely employed in both medical and non-medical applications since the discovery of X-rays in 1895[9]. The technique relied on X-rays absorption by matter and the X-ray attenuation depends on tissues composition, in particular density and atomic number of the tissue components[10]. Whereas CT imaging of hard tissues such as bones and cartilages are very sensitives to X-rays, imaging of soft structures (fatty tissues or neoplastic formations) required contrast agents to improve the image performance[11]. Currently, the use of a CT agent requires the administration of the probe in the molar range, which represents one of the major downsides of this diagnostic tool compared to other imaging techniques such as MRI (sub-molar conc. range), nuclear and optical imaging (μmolar conc. range)[10], especially in the field of molecular imaging CT contrast agents are based on high-Z elements and may be classified in two major categories: small molecular agents (typically based on iodine or lanthanides) and nanoparticulate agents. Although iodine (Z = 53) has historically been the atom of choice for CT imaging applications, clinically employed iodinated contrast agents (e.g., iohexol, ioversol, and iopamidol) suffer from low sensitivity, poor spectral CT, potential allergy, and renal toxicity[12–14]. Hence, the development of improved CT contrast agents is still subject matter of interest. To date, the development of Bi-based CT agents is mostly focused on the design of nanoparticle systems because of their greater contrast density, longer circulation times and versatility for targeting purposes[11]. Representative examples are the Bi_2S_3 nanoparticles labelled with the cyclic nine amino acids peptide LyP-1 for targeting breast cancer[13] and the MUC-16 aptamer targeted Bi-DOTA-PEG nanoparticles for imaging cervical cancer[14]. However, despite the promising preclinical results, no clinical translation has been reported so far for nanoparticulate agents, unlike small metal chelate-based contrast agents. On the other side, Bi-based small molecules have not been still sufficiently emphasized, with just a few examples reported, such as Bi-DPTA[4] and Bi-DOTA[15]. On these premises, the aim of this study is to develop a new potential Bi-based small complex using the ligand HPDO3A (**Figure 1**). HPDO3A is successfully used in MRI clinical exams since 2003, when its Gd(III) complex (Gadoteridol, marketed as ProHance®) received the approval for clinical use.

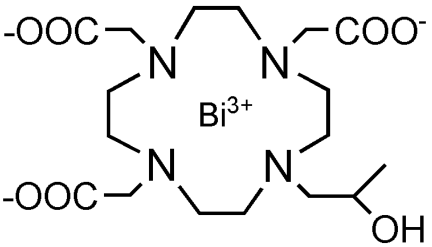

Figure 1 Bi-HPDO3A chemical structure.

A very important advantage of Bi-HPDO3A over the previously reported Bi-DOTA and Bi-DTPA complexes, is represented by its electroneutrality that may allow the administration of a higher dosage without affecting the osmolarity of the injected solution, and, as it has been clearly demonstrated for the complexation of lanthanide ions, without reducing the thermodynamic and kinetic stabilities of the metal complex[16]. The synthesis of Bi-HPDO3A is simple and cost-effective, and the ligand can be easily modified to allow the conjugation of the complex to targeting vectors[17]. In this work, the newly proposed agent has been characterized both *in vitro* and *in vivo* in terms of biocompatibility and CT imaging performance, using iopamidol as reference.

EXPERIMENTAL SECTION

Chemicals

All chemicals were purchased from Sigma-Aldrich, all the solvents from VWR, HPDO3A and Iopamidol (Isovue 370) were kindly provided by Bracco Imaging S.p.A.

UPLC-MS of Bi-HPDO3A was obtained on a Waters system (Acquity UPLC H class Plus). ^{1}H-NMR spectra and ^{13}C-NMR spectra were measured on a Bruker Avance spectrometer (600 MHz) instrument. Chemical shifts are reported in parts per million (ppm) and are referenced to tetramethylsilane.

UV/Vis spectrophotometric measures were performed on a UV/Vis spectrophotometer (6715, Jenway).

Cell cultures and animals

Monocyte-macrophages (J774 cells) were purchased from ATCC. Cells were cultured until confluence using DMEM (Euroclone) medium supplemented with glutamine (2 mM), 10% fetal bovine serum (FBS, Sigma-Aldrich, St. Louis, MO, USA) and penicillin/streptomycin antibiotics (10000 IU/mL penicillin, 10,000 IU/mL streptomycin, Corning Cellgro, Manassas, VA). MTT Cell Proliferation Kit was purchased from OZ Bioscience.

5-weeks-old BALB/C male mice were obtained from the animal facility of the Department of Molecular Biotechnology and Health Sciences (University of Turin, Italy). Animal manipulation and experimental procedures were carried out in accordance with the European Community guidelines (directive 2010/63) and under the approval of the Italian Ministry of Health (authorization #229/2016).

Synthesis and characterization of Bi-HPDO3A

Bi-HPDO3A complex was synthesized starting from HPDO3A ligand and bismuth(III) carbonate in a 2:1 molar ratio, respectively (**Figure 2**). 1 g (2.36 mmol) of ligand was solubilized in 15 mL of deionized water prior to bismuth carbonate addition (0.75g, 1.18 mmol) and the mixture was heated at 95°C for 3 weeks.

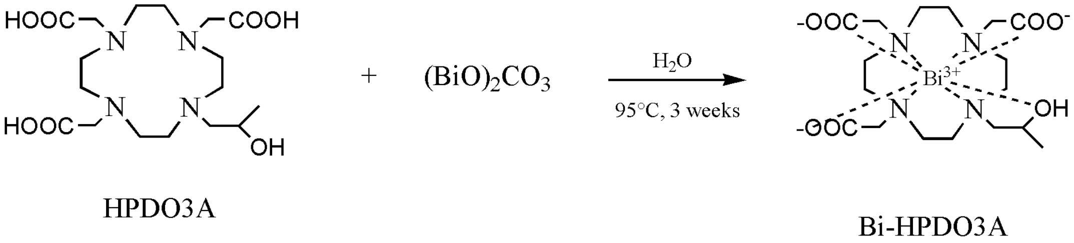

Figure 2 Bi-HPDO3A synthetic procedure.

The xylenol orange test was performed[18] to monitor the reaction progress and a small amount of ligand was added to have a free metal quantity not exceeding 0.1%. The reaction suspension was filtered (0.45 µm pore size) and the filtrated was lyophilized to obtain a white solid. The compound was then used without further purification.

The metal chelate was characterized by NMR, UV-Vis spectrophotometry, and ultra-performance liquid chromatography coupled to mass spectrometry (UPLC-MS). The new bismuth agent was dissolved in deionized water and diluted to the concentration of 0.4 mM for UV/Vis measurements (200-500 nm range). For NMR characterization, the complex was dissolved in D_2O to a final concentration of 3 mg/mL and, the ^{1}H- and ^{13}C-NMR spectra were acquired at room temperature. The complex was also characterized by ESI–MS, and UPLC-UV/Vis spectra were recorded to assess the purity.

Stability measurements over time and transmetallation with Zn(II)

Physical stability of an aqueous solution of the complex was checked within 14 days to assess colloids formation. Stability in PBS and human serum at 37°C was monitored within 24h by measuring the absorbance of the Bi-complex (0.123M) at 305 nm at 3 different times (3, 6 and 24 h). Transmetallation of Bi-HPDO3A towards Zn(II) ions was investigated by measuring the absorbance of the Bi-complex at 305 nm at 3 different times (3, 6 and 24 h) after mixing equimolar amount (20 mM) of Bi-HPDO3A and Zn(II) at 37°C and pH 7.4.

In vitro cytotoxicity

Cellular methyl thiazolyl tetrazolium (MTT) assay was carried out to evaluate the cytotoxicity of Bi-HPDO3A *in vitro*. J774 cells (50k cells/well) were incubated in a 96-wells plate for 24 h. The medium was then replaced by fresh one containing different concentrations of Bi-HPDO3A (3, 6, 12.5, 25, 50, 125, 250, and 500 µM). After the incubation, cells were incubated with MTT reagent for 3h. Then, the solubilization solution was added to dissolve the purple formazan crystals. After 30-mins of mild shaking, the absorbance value at 600 nm of each well was recorded through a microplate reader. The experiment was conducted in triplicate in 3 different experimental sessions.

CT imaging

Aqueous solutions at different Bi-HPDO3A concentrations (3-400 mM range) were prepared, and *in vitro* CT imaging was performed (MiLabs VECTor^6, 65 kV, 0.25 mA, 45 ms). A commercially available solution of iopamidol (Isovue-370® Bracco Imaging), properly diluted, was used as reference.
For *in vivo* CT imaging experiments, mice were anaesthetized with isoflurane (1.5%–2.5%, 1 ml/min oxygen flow rate) and then scanned before and after the injection via the tail vein of 100 µL of Bi-HPDO3A or iopamidol solutions to reach a dose of 0.5, 1.2 and 5 mmol Bi/kg bw or 1.2 mmol I/kg bw, respectively. CT scans were acquired at different time points (0, 1 min, 5 min, 20 min, 40 min, 1 h). The parameters were set as follows: field of view 54x140 mm, tube current 0.25 mA, tube voltage 65 kV, exposure time 45 ms. VOIs analysis for kidneys and bladder were performed to semi-quantify the complex distribution in these main involved organs.

Histology

To verify possible acute toxicity effects of Bi-HPDO3A on kidneys, hematoxylin-eosin (HE) staining was carried out on mice kidneys explanted 7 days and 14 days after the administration of the agent (5 mmol Bi/kg bw).

RESULTS and DISCUSSION

Characterization of Bi-HPDO3A

The Bi-HPDO3A complex was characterized by multiple analytical methods. The ^{1}H-NMR spectra (600 MHz, D_2O, pH=6.5, 298K) of Bi-HPDO3A showed the following signals (TMS as reference): 1.19 ppm (d, 3H, methyl group), 3.10-3.67 ppm (m, 19H, ethyl groups), 3.81 ppm (m, 3H, ethyl group), 4.05 ppm (d, 1H, hydroxyl), 4.36-4.49 ppm (m, 3H, acetic pendant arms) (See Appendix I **Fig. S3** and **S4**).

The ESI-MS spectrum of Bi-HPDO3A was characterized by m/z peaks found at 306.02, 611.16 and 1221.44, which correspond to, $[M + 2H]^{2+}$, $[M + H]^{+}$ and $[2M+H]^{+}$, respectively. Furthermore, as calculated from the UPLC-UV/Vis spectrum, the metal complex was obtained with a purity > 99%. (See Appendix I **Fig. S1** and **S2**).

In vitro stability

The stability of a solution of Bi-HPDO3A 0.123M (1.2 mmol/kg) was checked within 14 days after storage at room temperature. The solution remained clear without any precipitation event after centrifugation at 4000 rpm for 10 minutes. Structural stability of the bismuth complex was investigated by means of UV-vis measurements. The complex proved to remain intact both in PBS and HS for 24 h at 37°C (Fig. **S11**). Crucial aspect to be considered for the potential clinical translation of a metal complex is to check the stability towards transmetallation.

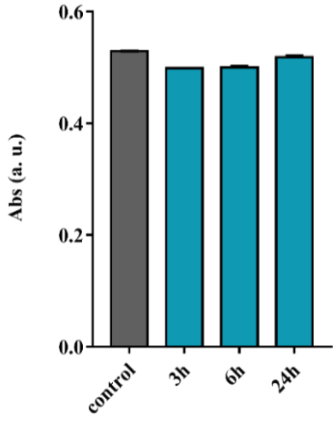

Figure 3 UV measurements at λ=305 nm for transmetallation study of Bi-HPDO3A (20 mM) with Zn^{2+} (20 mM).

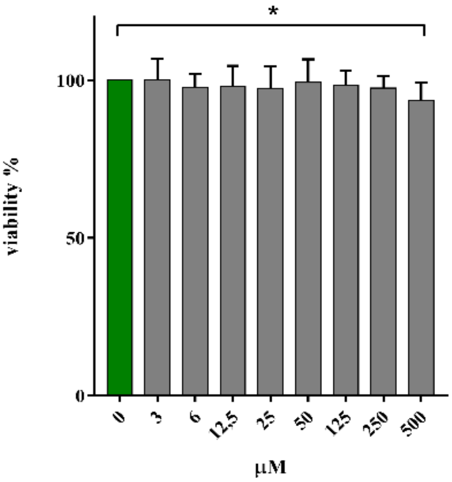

Figure 4 Viability % on J774 cells treated with Bi-HPDO3A (24h, 0-500 μM). P* = 0.044.

Due to the relatively high blood concentration (55-125 μM) and the high affinity to polyamino-polycarboxylic ligands, Zn(II) is typically used as competitor endogenous metal ion to predict the in vivo stability of metal complexes[19].
A calibration curve was preliminary assessed for Bi-HPDO3A (**Figure S4**) and the whole UV-vis spectrum was recorded to establish the maximum absorption wavelength (λ_{max}, 305 nm) of the complex. **Figure 3** indicates that the absorbance of Bi-HPDO3A at 305 nm in presence of an equimolar amount of Zn(II) ions was not affected after one day of incubation at 37°C and pH 7.4. This result fully agrees with the high thermodynamic and kinetic stability expected for Bi-HPDO3A complex. In fact, it has been reported that Bi(III) forms octacoordinated highly stable complexes and log K_{ML} values of 30.3 and 26.8 have been reported for DOTA and an HPDO3A-like ligand, respectively[20].

Cytotoxicity

The cytotoxicity of Bi-HPDO3A was assessed by the standard MTT test on a murine cell line of macrophages (J774). Cells were incubated for 24 h with different concentrations of the Bi-complex (0-500 µM range).

The result of the MTT test (**Figure 4**) revealed an excellent biocompatibility with cell viability values attesting from 90% to 100% with no statistically significant differences (statistical analyses were conducted using the one-way ANOVA method and statistical significance was defined at P values less than 0.05) in the examined concentration range except for the concentration of 500 µM.

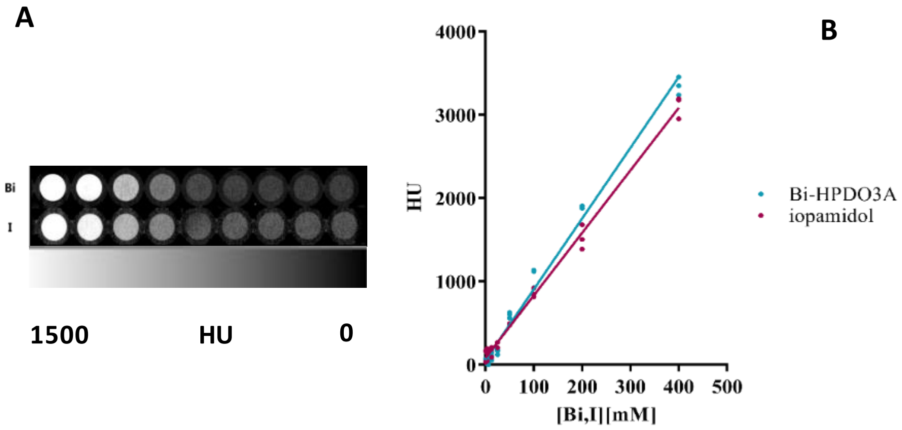

Figure 5 (A) Phantom CT imaging. **(B)** Comparison between Bi-HPDO3A and iopamidol *in vitro* CT attenuation capabilities.

In vitro CT imaging performances

The *in vitro* CT performance of Bi-HPDO3A was evaluated by measuring the X-ray attenuation as a function of the probe concentration in the 0-400 mM range (**Figure 5**). Data were compared with solutions of iopamidol containing iodine concentrations in the same interval. The expected linear correlation between HU units and atom concentration was found for both agents. Unfortunately, the voltage limitations imposed by the available scanner (65 kV) prevented to exploit the larger X-ray attenuation coefficient of Bi at higher voltage, and in this acquisition setting, the two agents performed very similarly.

In vivo CT imaging experiments and toxicity assessment

The promising properties observed *in vitro* for Bi-HPDO3A prompted us to preliminarily test the *in vivo* performance of the agent on healthy mice.

The first dosage of 5 mmol/kg of Bi-HPDO3A were intravenously injected into BALB/C mice to assess biodistribution and *in vivo* X-ray attenuation capability of the agent. A high CT contrast was observed both in kidneys and bladder (**Figures 6A** and **6B**). Kidneys were already lighted up 1-minute post injection, and within 60 minutes the bladder CT contrast signal increased linearly. Interestingly, after a rapid increase, the enhancement of the renal signal remained largely unchanged after 20 min post injection. Encouraged from this positive result, a lower injected dose (1.2 mmol/kg) was tested. This value was calculated starting from the clinical injected dose of the MRI agent Gadoteridol, scaled down to mice, taking into account the difference in body surface area between the two organisms [24]. Despite the expected lower CT contrast, a clear signal was detected in the renal collecting system (calyx and ureter, **Figures 7A** and **S7**). To further challenge the attenuation capability of the Bi-HPDO3A complex, a further dose reduction (down to 0.5 mmol/kg) was attempted (**Figure S6**). Expectedly, the CT contrast was the lowest among the three conditions explored, and the signal decreased according to the dose (**Figure 8**). The signal was only detected on the calyx portion of the collecting system with a maximum peak 5-minutes post injection to finally disappear 40-minutes post injection.

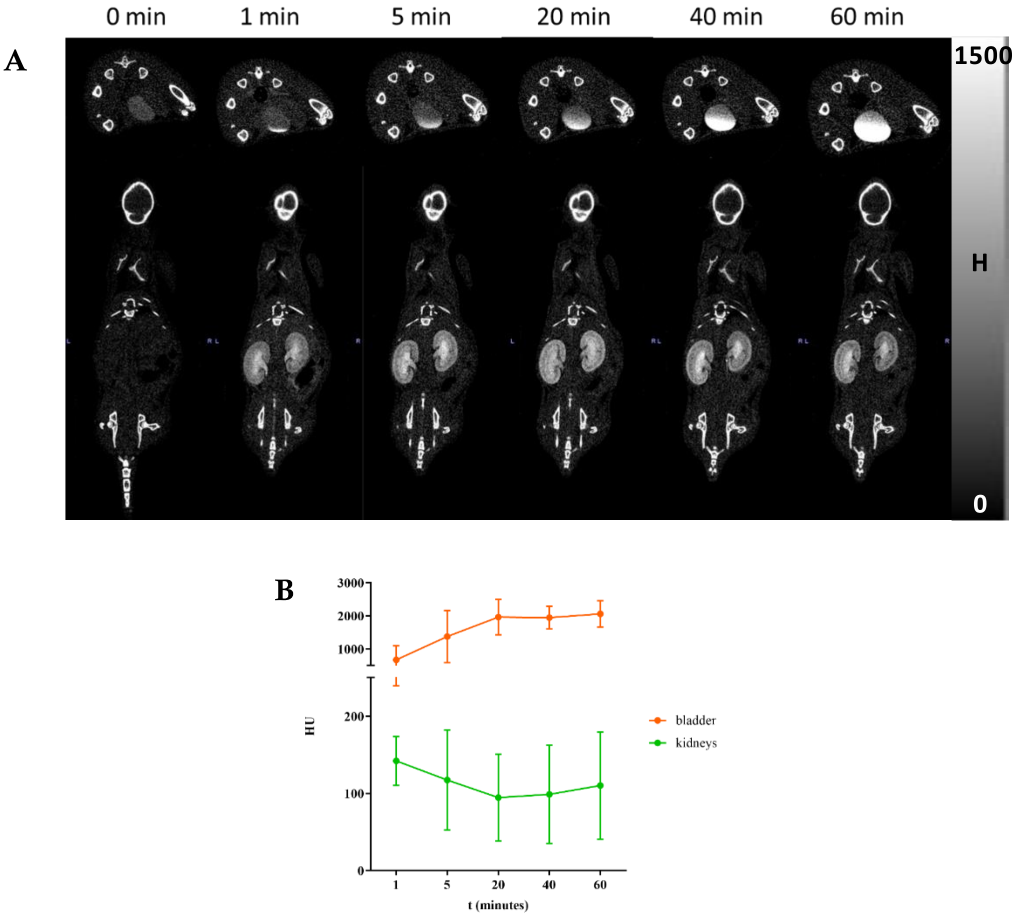

Figure 6 (A) *In vivo* CT imaging after *i.v.* administration of 5 mmol/kg of Bi-HPDO3A. Bladder and kidneys CT contrast are displayed. **(B)** VOIs analysis on bladder and kidneys for a dose of 5 mmol/kg of Bi-HPDO3A.

For comparative purposes, the imaging performance of Bi-HPDO3A was challenged with the clinically approved iodine-based iopamidol, using the injected dose of 1.2 mmol/kg.

Iopamidol allowed for the visualization of the whole renal region (**Figure S8**, A) and, when compared to Bi-HPDO3A, displayed a slower renal clearance (**Figure S8**, B)

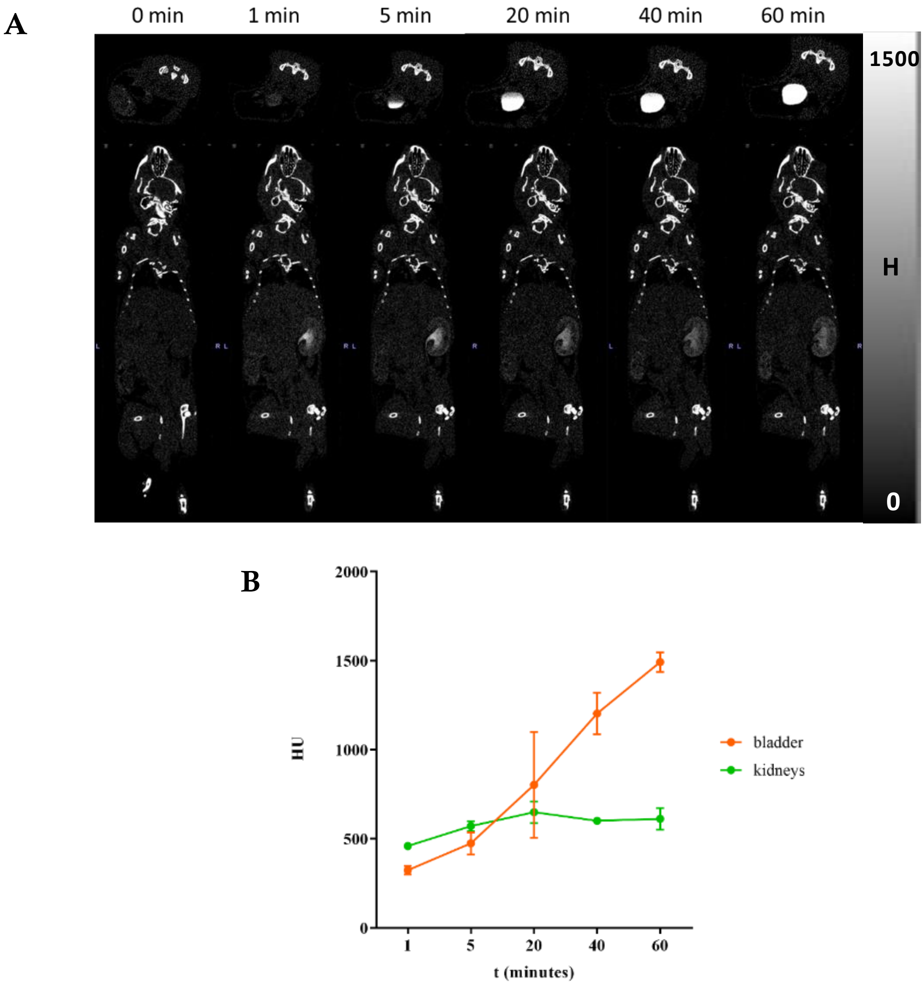

Figure 7 (A) *In vivo* CT imaging after i.v. administration of 1.2 mmol/kg of Bi-HPDO3A. Bladder and kidneys CT contrast are displayed. **(B)** VOIs analysis on bladder and kidneys for a dose of 1.2 mmol/kg of Bi-HPDO3A.

with the kidney contrast that progressively increased in the first hour post- injection, in agreement with literature data[21].

The different contrast dynamics displayed by the two probes in the kidneys is reported in **Figure 8**.

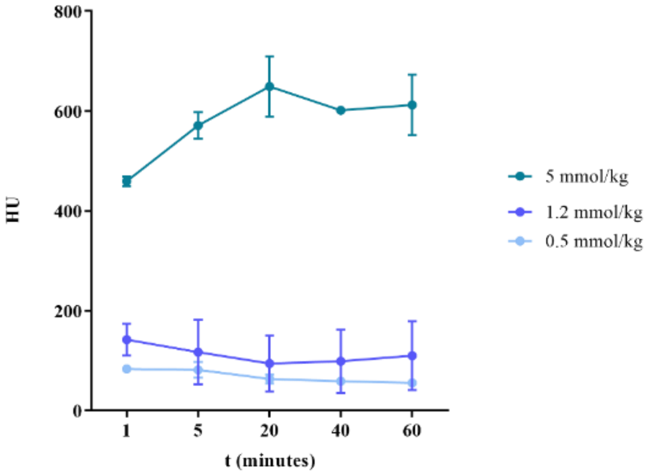

Figure 8 Dynamics of the kidney CT contrast for the three different injected doses of Bi-HPDO3A.

Considering that the amount of the injected probes was equal, the higher contrast detected for iopamidol is primarily due to the higher molar concentration of attenuating atoms (3 iodine atoms/molecule vs 1 Bi atom/molecule), whereas the different dynamics can be explained in terms of the different hydrophilicity of the two agents, with the more hydrophilic Bi-HPDO3A complex that showed a faster renal clearance. To preliminary investigate the *in vivo* acute toxicity of the new compound in the main excretory organ, HE staining of the kidneys of mice injected with the highest dose (5 mmol/kg) of agent was performed. No tissue-damaging effects were found (**Figure S10**), thus confirming the good safety profile of the new probe.

CONCLUSIONS

This study presents a novel bismuth-based potential CT contrast agent based on the HPDO3A ligand. The high X-ray attenuation coefficient of bismuth, its wide safety profile, and the well-known characteristics as chelating agent of HPDO3A, already clinically employed, makes it an excellent candidate for this purpose. Although the sub-optimal voltage (65 kV) of the available scanner, Bi-HPDO3A has proved to have a good potential as CT contrast agent for imaging kidneys and bladder. The high-water solubility of this agent led to a rapid renal excretion, faster than

Iopamidol, thus reducing possible risks of toxicity caused by unwanted tissue accumulations. The results reported herein suggest further investigations. Multimeric versions of this ligand, or similar macrocyclic ligands forming neutral complexes with trivalent metals, have been already reported, which could improve detection sensitivity, in analogy to what has been done with iodinated agents[22,23] Furthermore, HPDO3A ligand is suitable of conjugation with chemicals for modulating and optimizing the biodistribution of the agent, thus opening new potential applications, in addition to image renal diseases.

APPENDIX I

UPLC-UV/Vis-MS

The chromatographic runs were performed using a Kinetex F5 column 100 x 2.1 mm, 1.7 µm (Phenomenex). The column oven was maintained at 25°C and the elution solvents were water/trifluoroacetic acid 0.1% (solvent A) and acetonitrile/trifluoroacetic acid 0.1% (solvent B). The gradient was isocratic at 99% A for 8 min, then the composition was varied by a linear gradient (A:B, v/v) from 99:1 to 0:100 in 2 min to elute possibly present hydrophobic compounds (retention

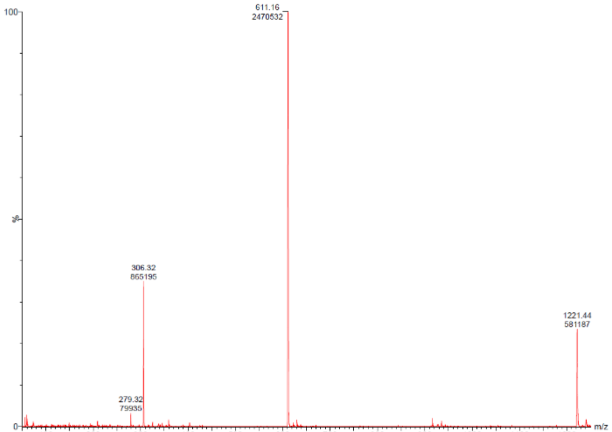

Figure S1 ESI-MS spectrum of Bi-HPDO3A. [2M-H]+ = 1221.44 m/z, [M-H]+ = 611.16 m/z, [M-2H]2+ = 306.02

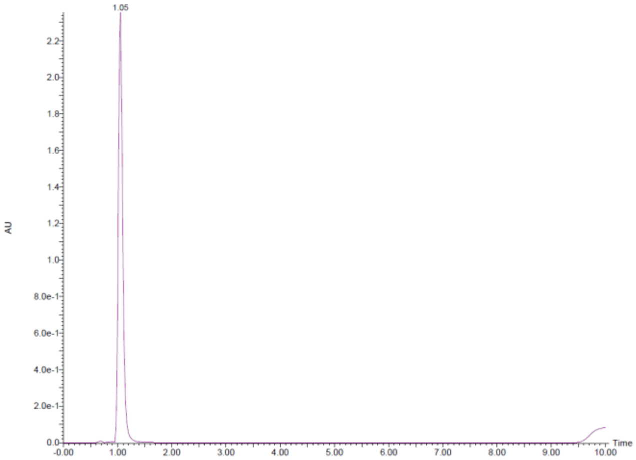

Figure S2 UPLC-UV/Vis spectrum at 214 nm of Bi-HPDO3A.

time of Bi-HPDO3A 1.05 min, **Figure S2**). The flow rate was 0.4 mL/min, and the total run time was 10 min.

The Waters 3100 Mass Detector was operated with an electrospray ion source in positive ion mode with a cone voltage of 20V. The intervals of mass scan were 50–1250 m/z. MS (ESI+): $[2M+H]^+$ 1221.44 (obsd) 1221.44 (calcd); $[M+H]^+$ 611.16 (obsd) 611.16 (calcd); $[M+2H]^{2+}$ 306.32 (obsd) 306.32 (calcd) (Figure S1).

UV/Vis spectra was recorded at 214 and 254 nm. The reported UV/Vis spectra (**Figure S2**) was recorded at 214 nm.

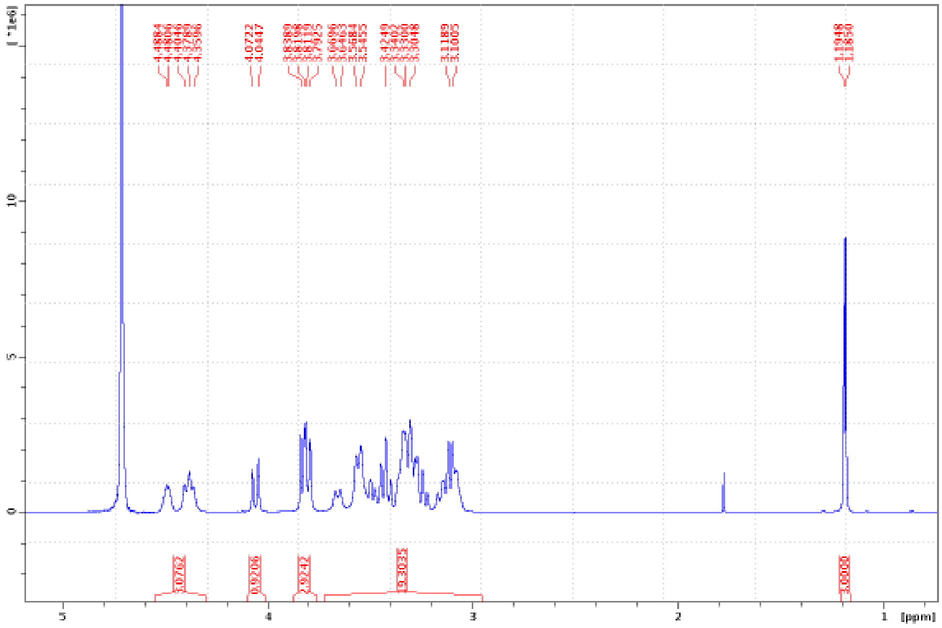

Figure S3 ^{1}H-NMR (600 MHz) spectrum of Bi-HPDO3A in D_2O (pH=6,5, T=298K). Chemicals shift (in ppm) and integrations are reported: δ 1.19 (d, 3H), δ 3.10-3.67 (m, 19H), δ 3.81 (m, 3H), δ 4.05 (d, 1H), δ 4.36-4.49 (m, 3H).

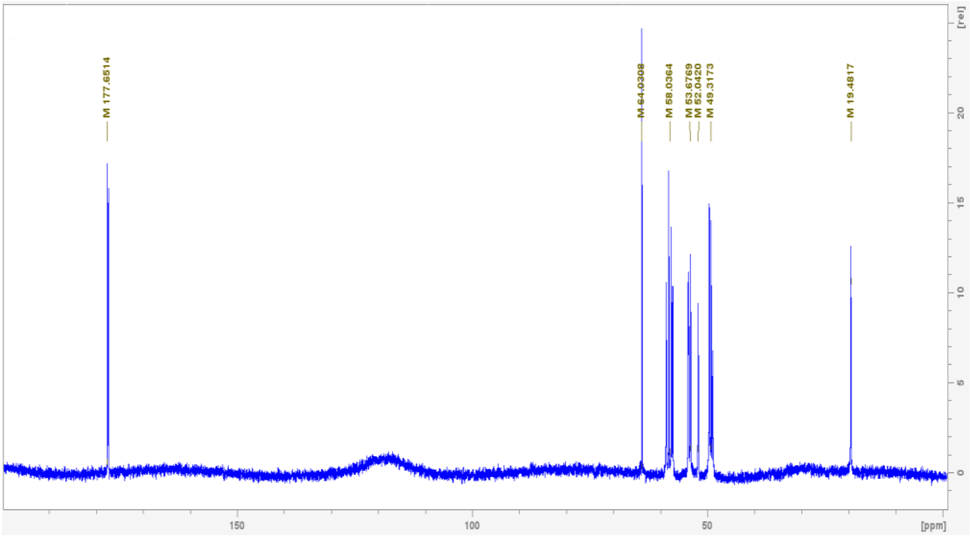

Figure S4 ^{13}C-NMR (600 MHz) spectrum of Bi-HPDO3A in D_2O (pH=6,5, T=298K). Chemicals shift (in ppm) are reported: δ 19.48, δ 49.32, δ 52.04-53.68, δ 58.04, δ 64.04, δ 177.65.

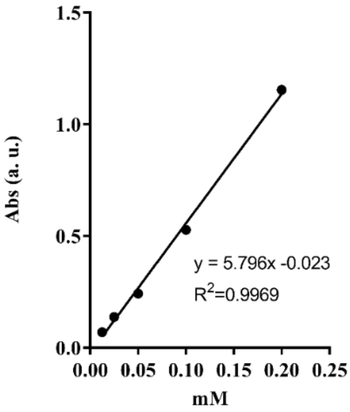

Figure S5 Calibration curve of Bi-HPDO3A at 305 nm for transmetallation study.

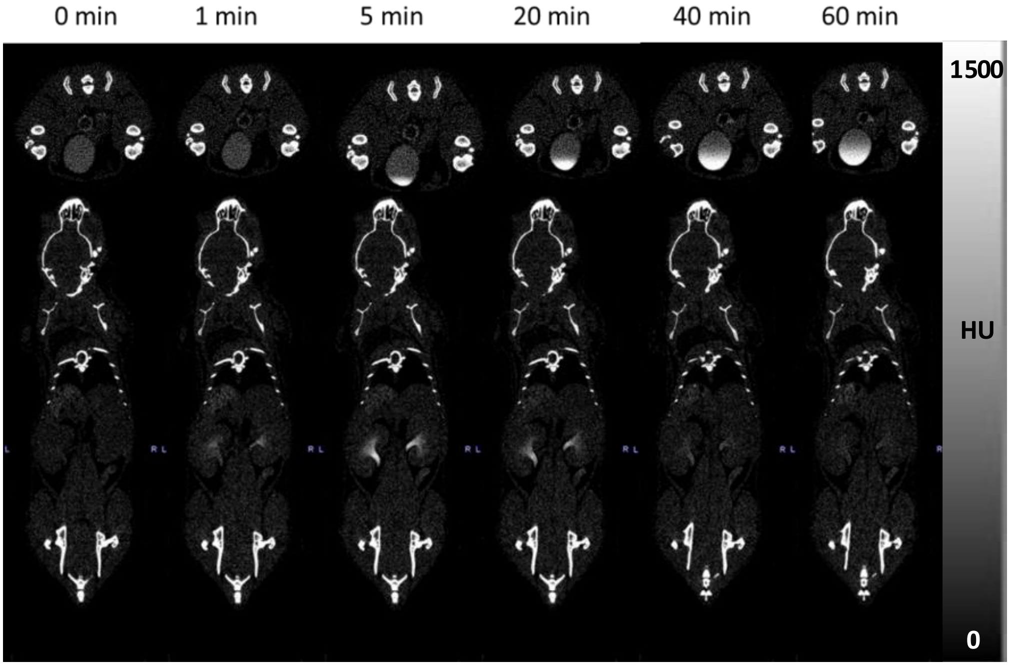

Figure S6 *In vivo* CT imaging after *i.v.* administration of 0.5 mmol/kg of Bi-HPDO3A. Bladder and kidneys CT contrast are displayed.

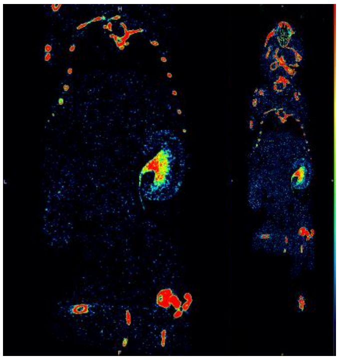

Figure S7 Ureter CT enhancement after *i.v.* administration of Bi-HPDO3A 1.2 mmol/kg (5 min).

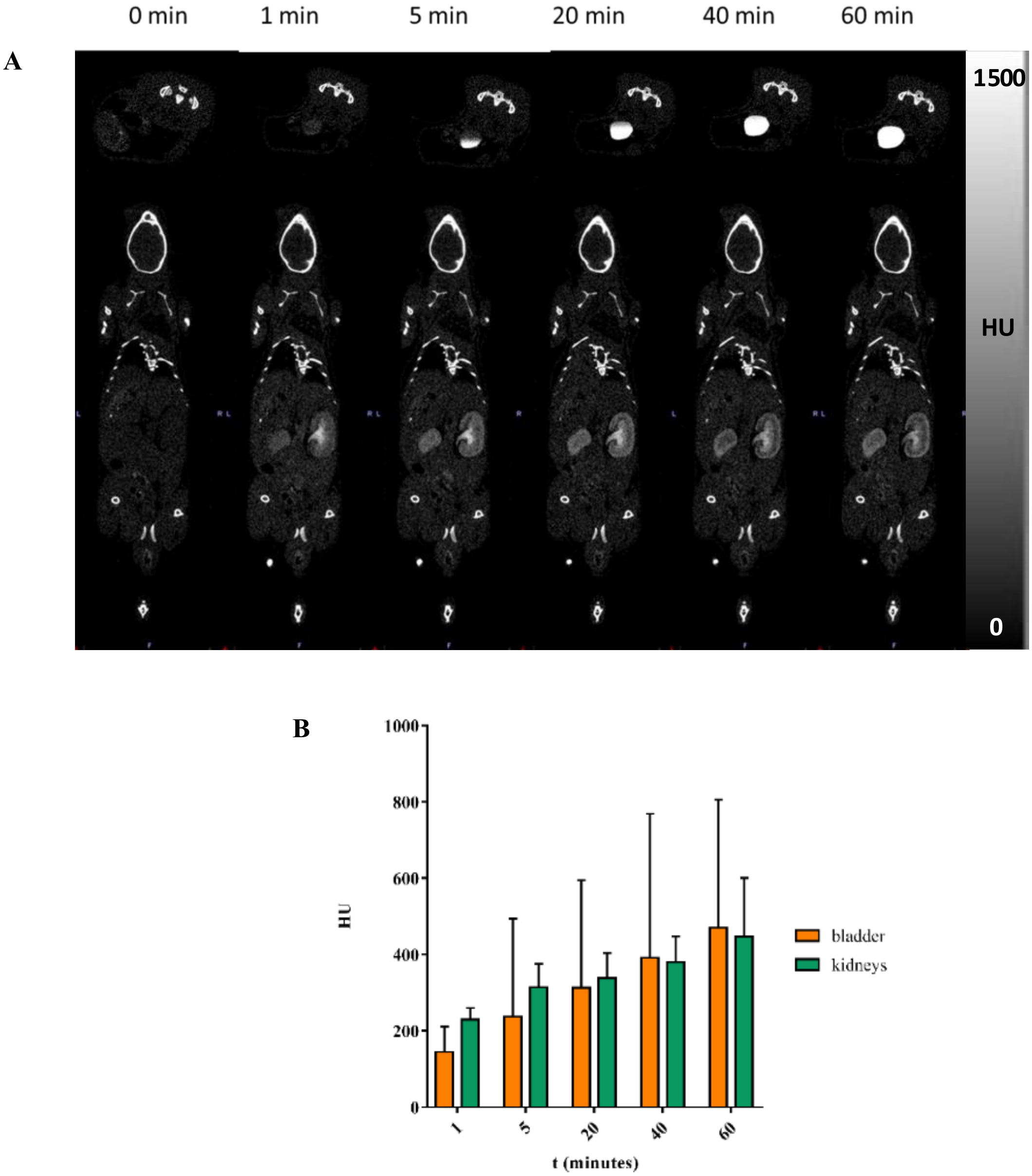

Figure S8 (A) *In vivo* CT imaging after *i.v.* administration of 1.2 mmol/kg of iopamidol. Bladder and kidneys CT contrast are displayed. **(B)** VOIs analysis on bladder and kidneys for a dose of 1.2 mmol/kg of iopamidol.

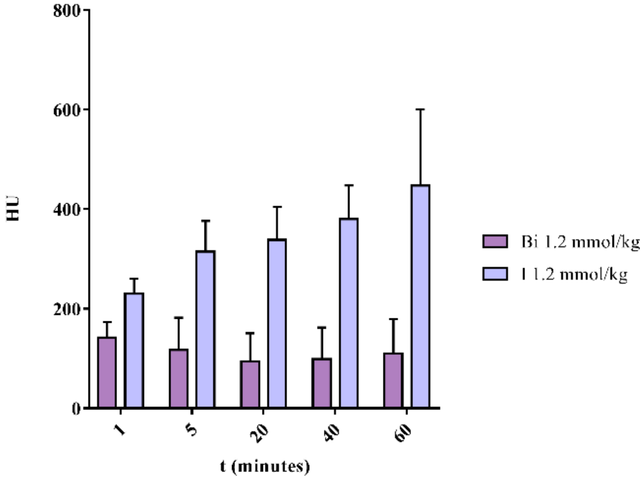

Figure S9 VOIs comparison analysis in the kidneys after *i.v.* administration of 1.2 mmol/kg of Bi-HPDO3A (purple) or Iopamidol (lilac).

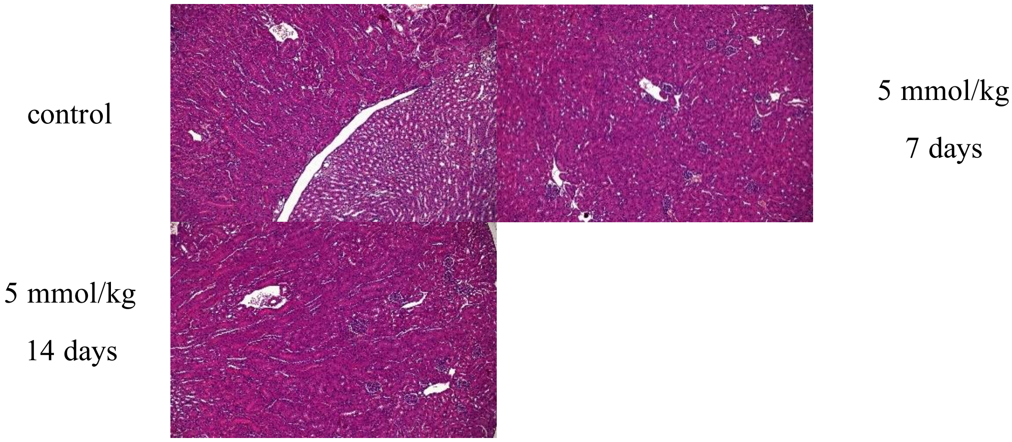

Figure S10 HE staining of kidneys after intravenous administration of 5 mmol/kg of Bi-HPO3A after different time points (7 and 14 days) (10x).

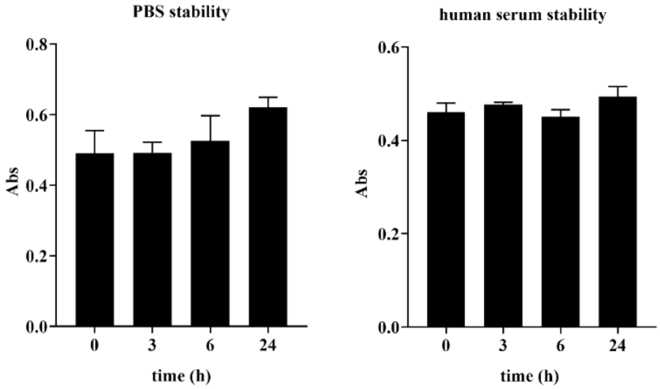

Figure S11 Stability in HS and PBS of Bi-HPDO3A 0.123M at 37°C within 24h.

References

[1] P. De Marcillac, N. Coron, G. Dambier, J. Leblanc, J.P. Moalic, Experimental detection of α-particles from the radioactive decay of natural bismuth, Nature. 422 (2003) 876–878.

[2] S. Ahenkorah, I. Cassells, C.M. Deroose, T. Cardinaels, A.R. Burgoyne, G. Bormans, M. Ooms, F. Cleeren, Bismuth-213 for targeted radionuclide therapy: From atom to bedside, Pharmaceutics. 13 (2021) 1–25.

[3] G.G. Briand, N. Burford, Bismuth Compounds and Preparations with Biological or Medicinal Relevance, Chem. Rev. 99 (1999) 2601–2658.

[4] J.J. Fu, J.J. Guo, A.P. Qin, X.Y. Yu, Q. Zhang, X.P. Lei, Y.G. Huang, M.Y. Chen, J.X. Li, Y. Zhang, J.P. Liu, Y.Y. Dang, D. Wu, X.Y. Zhao, Z.X. Lin, Y.L. Lin, S.P. Li, L.Y. Zhang, Bismuth chelate as a contrast agent for X-ray computed tomography, J. Nanobiotechnology. 18 (2020) 1–10.

[5] D.M. Griffith, H. Li, M. V. Werrett, P.C. Andrews, H. Sun, Medicinal chemistry and biomedical applications of bismuth-based compounds and nanoparticles, Chem. Soc. Rev. 50 (2021) 12037–12069.

[6] M.R. Gill, K.A. Vallis, Transition metal compounds as cancer radiosensitizers, Chem. Soc. Rev. 48 (2019) 540–557.

[7] S. Franchi, V. Di Marco, M. Tosato, Bismuth chelation for targeted alpha therapy: Current state of the art, Nucl. Med. Biol. 226 (2022).

[8] C. Gomez, G. Hallot, S. Laurent, M. Port, Medical applications of metallic bismuth nanoparticles, Pharmaceutics. 13 (2021) 1–26.

[9] M.M. Koç, N. Aslan, A.P. Kao, A.H. Barber, Evaluation of X-ray tomography contrast agents: A review of production, protocols, and biological applications, Microsc. Res. Tech. 82 (2019) 812–848.

[10] H. Lusic, M.W. Grinstaff, X-ray-computed tomography contrast agents, 2013.

[11] M. Algethami, B. Feltis, M. Geso, Bismuth Sulfide Nanoparticles as a Complement to Traditional Iodinated Contrast Agents at Various X-Ray Computed Tomography Tube Potentials, J. Nanomater. Mol. Nanotechnol. 06 (2017) 2–10.

[12] Z. Baranyai, F. Uggeri, A. Maiocchi, G.B. Giovenzana, C. Cavallotti, A. Takács, I. Tóth, I. Bányai, A. Bényei, E. Brucher, S. Aime, Equilibrium, kinetic and structural studies of AAZTA complexes with Ga3+, In3+ and Cu2+, Eur. J. Inorg. Chem. (2013) 147–162.

[13] O. Rabin, J.M. Perez, J. Grimm, G. Wojtkiewicz, R. Weissleder, An X-ray computed tomography imaging agent based on long-circulating bismuth sulphide nanoparticles, Nat. Mater. 5 (2006) 118–122.

[14] A. Tarighatnia, M.R. Fouladi, M.R. Tohidkia, G. Johal, N.D. Nader, A. Aghanejad, H. Ghadiri, Engineering and quantification of bismuth nanoparticles as targeted contrast agent for computed tomography imaging in cellular and animal models, J. Drug Deliv. Sci. Technol. 66 (2021) 102895.

[15] G. Dai, Y. Zhang, X. Wang, X. Wang, J. Jia, F. Jia, L. Yang, C. Yang, Small-Molecule Bi-

DOTA Complex for High-Performance CT and Spectral CT Bioimaging, Front. Oncol. 12 (2022) 1–11.

[16] P. Hermann, J. Kotek, V. Kubíček, I. Lukeš, Gadolinium(III) complexes as MRI contrast agents: Ligand design and properties of the complexes, Dalt. Trans. 9226 (2008) 3027–3047.

[17] A. Barge, E. Cappelletti, G. Cravotto, A. Ferrigato, L. Lattuada, F. Marinoni, L. Tei, Synthesis of functionalised HP-DO3A chelating agents for conjugation to biomolecules, Org. Biomol. Chem. 7 (2009) 3810–3816.

[18] P.C.A. Jerónimo, A.N. Araújo, M.C.B.S.M. Montenegro, D. Satinský, P. Solich, Colorimetric bismuth determination in pharmaceuticals using a xylenol orange sol-gel sensor coupled to a multicommutated flow system, Anal. Chim. Acta. 504 (2004) 235–241.

[19] S. Laurent, L. Vander Elst, C. Henoumont, R.N. Muller, How to measure the transmetallation of a gadolinium complex, Contrast Media Mol. Imaging. 5 (2010) 305–308.

[20] Ä. Csajbo, Z. Baranyai, J. Platzek, B. Radu, M. Scha, Equilibrium , 1 H and 13 C NMR Spectroscopy , and X-ray Diffraction Studies on the Complexes Bi (DOTA) - and Bi (DO3A-Bu), 42 (2003) 2342–2349.

[21] M. Bourin, P. Jolliet, F. Ballereau, An overview of the clinical pharmacokinetics of x-ray contrast media, Clin. Pharmacokinet. 32 (1997) 180–193.

[22] J. Lohrke, M. Berger, T. Frenzel, C.S. Hilger, G. Jost, O. Panknin, M. Bauser, W. Ebert, H. Pietsch, Preclinical Profile of Gadoquatrane: A Novel Tetrameric, Macrocyclic High Relaxivity Gadolinium-Based Contrast Agent, Invest. Radiol. 57 (2022) 629–638.

[23] E. Di Gregorio, G. Ferrauto, E. Gianolio, S. Aime, Gd loading by hypotonic swelling: An efficient and safe route for cellular labeling, Contrast Media Mol. Imaging. 8 (2013) 475–486.

Chapter 2

Synthesis, radiolabelling and *in vitro* validation of a [^{68}Ga]Ga-AAZTA tracer for FAP imaging by PET

ABSTRACT

The aim of this work was to demonstrate the suitability of AAZTA chelator conjugated to a FAPI-46-derived FAP inhibitor and labelled with gallium-68 as a potential PET tracer. This work reports the synthesis of the AAZTA-FAPI-46 ligand, the optimization of the radiolabelling procedure (both manual and automatic) with the gallium-68 radioisotope. The new radiotracer was characterized in terms of $\log D_{7.4}$, (radio)chemical stability in PBS, EDTA and human serum. Moreover, *in vitro* biological tests on FAP-expressing cells were performed to assess IC_{50} and cellular internalization.

INTRODUCTION

In the era of radio-theranostics, the AAZTA chelator (**Figure 1**) has been attracting increasing interest thanks to its ability to complex diagnostic and therapeutic trivalent radiometals (such as ^{68}Ga, ^{44}Sc and ^{177}Lu) using mild labeling conditions[1,2]. In fact, the most widely used chelators for radiometals (macrocyclic derivatives based on DOTA and NOTA (chemical structures reported in **Figure 1**)) typically requires high or moderate temperatures to achieve high labelling yields. Moreover, for theranostic strategies involving ^{177}Lu, only DOTA can be used, requiring labelling at temperatures close to 100 °C, temperature at which many molecular targeting vectors (e.g., those based on proteins) are unstable. Among a panel of candidates for room temperature radiolabelling[3] (*e.g.*, HBED[4] N,N'-bis(2-hydroxybenzyl)ethylenediamine-N,N'-diacetic acid, THP[5] (tris(hydroxypyridinone), DATA[6] (6-amino-1,4-diazapine-triacetate), AAZTA was reported to successfully chelate not only Ga-68 but also lutetium-177 and scandium-44, making it suitable for theranostic applications. AAZTA (an heptadentate aminopolycarboxylate ligand with a 1,4-diazepine scaffold) has been extensively studied as chelator of Gd^{3+} ions for MRI applications[7,8]. This ligand has already been proven to form thermodynamically stable and kinetically inert Ga^{3+} complexes[9], therefore several AAZTA conjugates were developed over the last years. As examples, Manzoni *et al.* already demonstrated the formation of ^{68}Ga-AAZTA-RGD complex at room temperature in acetate buffer at pH 3.8[10], and CyAAZTA was successfully radiolabelled with gallium-68 in acetate buffer at pH 3.8, in 15 minutes at room temperature by Vagner and coworkers[11]. In the field of theranostics, over the last 10 years the pan-cancer biomarker Fibroblast Activation Protein (FAP) has gained increasing attention[12]. FAP, known also as seprase[13], is a transmembrane type-II protein belonging to the family of dipeptidyl peptidases[14].

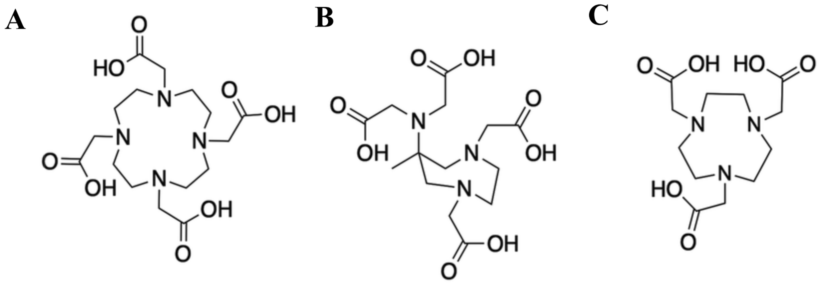

Figure 1 Chemical structures of DOTA (A), AAZTA (B) and NOTA (C).

FAP has been recently attracting interest since its involvement in angiogenesis, growth, aggressiveness, progression, and prognosis of cancer[15]. Low basal levels of FAP expression might be found in many tissues, including the bone marrow, adipose, and skin[16]. Being involved in the extra-cellular matrix (ECM) tissue remodeling processes[17], FAP was found to be present also in such non-cancer disease like fibrosis[18], arthritis[19], atherosclerosis[20] and infarction[21]. But more importantly, FAP is considered to be absent in healthy tissues[22], and it is overexpressed by CAFs (cancer associated fibroblasts) in more than 90% of epithelial tumors[23], including breast, lung, pancreas, brain and colon cancer[24]. Since the development of the most potent FAP inhibitor named UAMC1110[25], several radiopharmaceuticals have been developed for PET, SPECT and therapy purposes [26–28] Remarkable examples include FAPI-04[29] and FAPI-46[30] agents. This work mainly aims at synthetizing a new AAZTA-based FAP inhibitor based on FAPI-46 structure and optimizing the radiolabeling with gallium-68 for PET purposes. Moreover, the tracer was characterized in terms of (radio)stability in different media and affinity towards FAP expressing cells.

EXPERIMENTAL SECTION

Materials

All chemicals were purchased from Sigma-Aldrich, all the solvents from VWR. UPLC-MS of AAZTA-FAPI-46 was obtained on Waters system (Acquity UPLC H class Plus). Purification of AAZTA-FAPI-46 was carried out on HPLC system. ^{1}H-NMR spectrum of AAZTA-FAPI-46 were measured on a Bruker Avance spectrometer (400 MHz) instrument. Chemical shifts are reported in parts per million (ppm) and are referenced to tetramethylsilane. Radio-HPLC quality controls on radiolabeled AAZTA-FAPI-46 were performed on a Waters HPLC-MS system equipped with a Waters 1525 binary pump. Gel 60 F_{254} strips (Merck KGaA, Darmstadt, Deutschland) and ITLC-SG strips (Agilent Technologies, Didcot, UK) were used for radio-TLC quality controls. Sep-Pak C18 Light Cartridges (Waters) were used to purify the crude of reaction.

Synthesis of AAZTA-FAPI-46 chelator

The synthesis of the AAZTA-FAPI-46 was partially based on already published data[30]. The amide coupling between the simil-FAPI-46 precursor and the AAZTA^5 chelator was performed through a standard amide coupling. See Appendix II for synthesis and purification procedures and UPLC-MS spectra.

Gallium-68 manual radiolabelling

Elution of gallium-68 was performed with 0.1 M hydrochloric acid from a ^{68}Ge/^{68}Ga generator (Scintomics, Germany) in a volume of 1-1.2 mL containing the maximum activity of 410-460 MBq. Preliminary tests were conducted by using *ca.* 20 MBq to achieve the optimal experimental conditions. Aqueous solutions of HEPES 0.4 M or sodium acetate 0.4 M were used to adjust the pH of reaction. The reactions were conducted at room temperature.
Gallium-68 labelling of AAZTA-FAPI-46 was optimized by investigating the influence of pH, precursor concentration and time of reaction. Firstly, the optimal value of pH was assessed by using the precursor concentration of 40 µM (6.6 nmol). The different pH values and buffer conditions tested are listed in the Appendix II.

After finding the optimal pH value relying on the maximum % labeling of gallium-68, different AAZTA-FAPI-46 precursor concentrations were tested (0.5, 1, 5, 10, 15, 20, 40, 70, 100 µM). Finally, the kinetic of reaction was studied and aliquots were taken at 1, 3, 5, 10 and 15 minutes to measure the radiochemical yield.
Quality controls were performed by radio-TLC measurements using sodium citrate 1M pH=5 (considering the following retention factors (Rf): [[^{68}Ga]Ga-AAZTA-FAPI-46)] Rf < 0.1; ^{68}Ga colloids: < 0.1; soluble $^{68}Ga^{3+}$ Rf > 0.9) and Silica Gel 60 F_{254} strips and by radio-HPLC measurements. Purification was performed prior to *in vitro* experiments. The crude solution was worked-up by solid-phase extraction. After reaction time, the solution was diluted into 8 ml of water and then load bottom-up on the cartridge. The resulting syringe solution was the first waste solution that has proven to be efficient up to activity of 90 MBq. A second washing step with 10 ml of water was employed when activity greater than 90 MBq was used. ^{68}Ga-

AAZTA-FAPI-46 was eluted from the cartridge with 500 µL of water/ethanol 1:1 solution. Radiochemical yield (RCY%) was assessed by radio-HPLC measurements.

Gallium-68 automated radiolabelling

The preparation of [^{68}Ga]Ga-AAZTA-FAPI-46 was automated on a GallElut^{+} system (Scintomics, Germany). Briefly, the ^{68}Ge/^{68}Ga generator eluate was buffered to pH=3.5 using HEPES 2.7 M. AAZTA-FAPI-46 was then added to the gallium-68 solution (410-460 MBq, ca. 1.2 mL). The mixture was incubated at room temperature for 10 minutes before passing through a SPE cartridge (Waters, tC18 environmental cartridge), previously conditioning by purging with absolute ethanol (5 mL, Ph. Eur.) and water (10 mL, Ultrapure Water). The cartridge was then purged with water (10 mL) and air (10 mL). The labelled product was eluted from the cartridge into a 10 mL flask with a 1:1 mixture of ethanol and water (2 mL), following by purging with PBS buffer (1 mL, pH=7.4) and water (1 mL). The production time was approximately 30 minutes.

Stability studies

Stability studies of [^{68}Ga]Ga-AAZTA-FAPI-46 were performed in human serum, PBS and EDTA 5 mM over a period of 2 hours at 37ºC. 18-22 MBq of gallium-68 were buffered to pH=3.5 with HEPES 0.4 M and reacted with the AAZTA-FAPI-46 precursor (5 µM) for 15 minutes at room temperature. The purified compound obtained with a radiochemical purity greater than 98%, was used for the following stability studies in a ratio of 1:5 (400 µL of human serum, PBS or EDTA 5mM + 100 µL of labelled compound). After the incubation time (0.5 h, 1 h, 2 h) the sample vial was centrifuged for 5 min at 9000 rpm, 50 µL of the supernatant was collected and analysed by radio-HPLC.

Lipophilicity Measurements

Lipophilicity (expressed by the logD$_{7.4}$ value) was determined via the “shake-flask” method. Briefly, after the purification step, the pH of the product solution was adjusted to 7.4 with NaOH 1 M. 2-3 MBq of product were added to a 1 ml of PBS and octanol mixture (1:1). The vials were vortexed for 3 minutes, and then centrifuged for 5 minutes at 13000 rpm. The water and octanol fractions were separated, and the activity measured with a γ-counter (PerkinElmer, Beaconsfield, UK).

In vitro studies

For radioligand binding studies, HEK293T-FAP expressing cells ($3x10^5$ /well) were plated on 96-well plates 24 h prior to the experiment. On the day of the experiment, media was removed, and cells were washed with ice-cold PBS. Competition experiments were performed by simultaneous exposure to unlabelled compound (10^{-11} to 10^{-4}M) and [^{68}Ga]Ga-AAZTA-FAPI-46 (0.5 µM) for 1 h at 4 ºC. After 1 h incubation, the supernatant was collected, the cells were rinsed twice with ice-cold PBS, lysed with NaOH 1 M for 10 minutes and internalized fraction collected into vials. The experiment was performed five times. The radioactivity was assessed using a γ-counter (PerkinElmer, Beaconsfield, UK).

For internalization experiments, HEK293T-FAP expressing cells were incubated for 1 h at 37 ºC with of [^{68}Ga]Ga-FAPI-46. After 20, 40 and 60 minutes of incubation, media and subsequent PBS washings were discarded, and the surface-bound radioactivity was removed by washing the cells with 400 µL of ice-cold 50 mM glycine in 150 mM NaCl (pH=3) for 5 min on ice, followed by two washing with ice-cold PBS. To obtain the cell internalized fraction, cells were lysed with 400 µL of 1M NaOH. The radioactivity in both fractions was measured by a γ-counter.

RESULTS AND DISCUSSION

Manual radiolabelling

Gallium labelling of AAZTA-FAPI-46 (chemical structure reported in **Figure 2**) was first performed with a precursor concentration of 40 µM (6.6 nmol) and time of reaction of 15 minutes to assess the optimal pH value of reaction (**Figure S4**). The reactions conducted at pH value of 3,5 led to the higher radiochemical yield, hence this condition was further tested in triplicate (**Figure 2**). It was found that the labelling conducted ad pH=3,5 led to a minimal colloidal formation as well as a minimal free gallium content. This pH of labelling is in agreement with the Ga^{3+}-AAZTA system speciation diagram (**Figure 4**) obtained from pH-potentiometric titration by Baranyai and co-workers from which it follows that in the pH=3-4 range there is the maximum abundance of Ga^{3+} for complexation with AAZTA chelator and a minim formation of Ga(L)OH precipitation (colloidal species). Different precursor concentrations were then tested, and an almost quantitative incorporation was assessed for amount of precursor of 5 µM (**Figure 5A**).

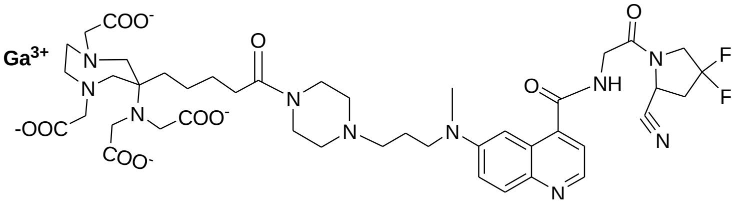

Figure 2 [^{68}Ga]Ga-AAZTA-FAPI-46 chemical structure.

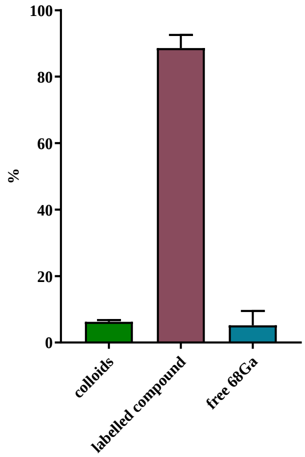

Figure 3 Quantification of free gallium, colloidal and complexed content after Ga-68 complexation of AAZTA-FAPI-46 at RT for 15 minutes with a precursor concentration of 40 µM at pH=3,5.

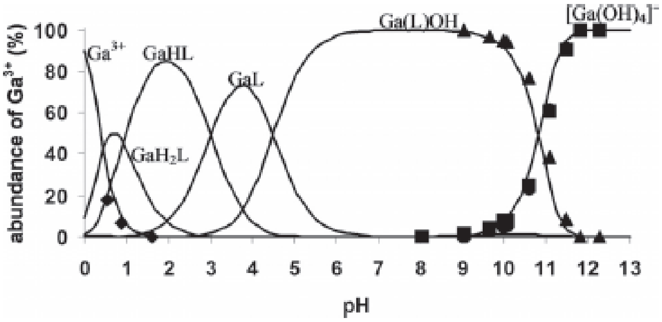

Figure 4 Ga^{3+} speciation for the Ga^{3+}–AAZTA system. Adapted from Baranyai *et al.* (*Eur. J. Inorg. Chem.* 2013, 147–162)

The complexation of AAZTA-FAPI-46 at room temperature with gallium-68 showed very rapid kinetics achieving high incorporation already after 1 minute (> 70%) for precursor concentration of 2.5 µM (0.385 nmol, **Figure 5B**), confirming previous reported data[2,31]. For ligand concentration ≥ 5 µM, no substantial differences were observed, demonstrating an excellent gallium-68 complexation.

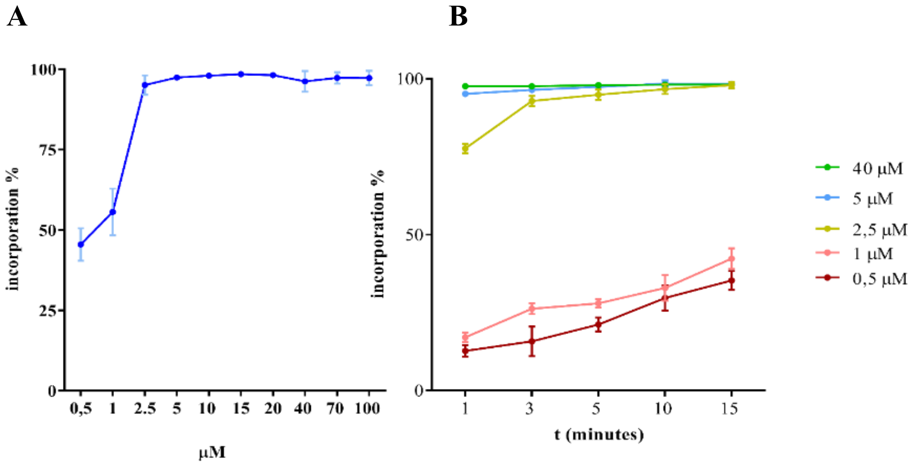

Figure 5 (A) Gallium-68 incorporation of AAZTA-FAPI-46 with different precursor concentration (RT, 15 minutes, pH=3,5). (B) Kinetics of [^{68}Ga]Ga-AAZTA-FAPI-46 at RT for tracer concentration ranging from 0,5 to 40 µM (RT, pH=3,5).

Automated radiolabelling

Optimization of an automated synthesis protocol was performed by measuring the resulting activity into the product vessel, the waste vessel and the SPE cartridge. Radio-TLC and radio-HPLC measurements were done to evaluate the efficiency and the reproducibility of the process. Furthermore, an automated procedure will have greater control over reaction times, temperatures and flow rates and could be quicker and more reproducible than the manual approach. The radiochemical yield was 84.97 ± 1.37 %.

Stability studies

To test the feasibility as PET tracer, stability in different media was investigated at 37°C for 2h. In **Figure 6** the percentage of intact compound after 30, 60 and 120 minutes of incubation was reported. [^{68}Ga]Ga-AAZTA-FAPI-46 proved to remain almost intact both in PBS and EDTA solutions, therefore no transchelation reaction was occurred over 120 minutes. Serum stability was also very high (>84% of intact compound), with a slightly significant difference at 120 min, demonstrating excellent compound stability *in vitro*.

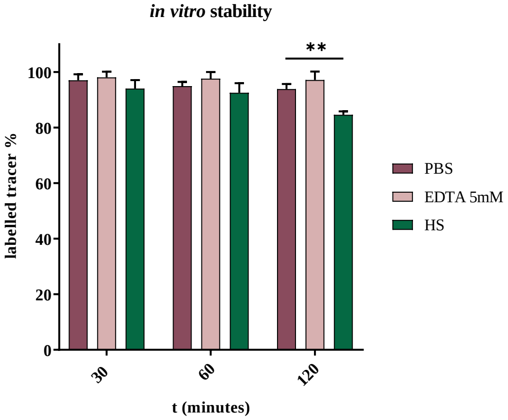

Figure 6 Stability investigation of [^{68}Ga]Ga-AAZTA-FAPI-46 in HS, PBS and EDTA over 2h at 37ºC. (*t*-test, p=0,0012).

Lipophilicity Measurements

The logD$_{7.4}$ value of FAPI-04, containing the DOTA chelator for gallium labelling, is reported in the literature as −2.4 ± 0.28, confirming the hydrophilic character of ^{68}Ga-DOTA complexes. Although the [^{68}Ga]Ga-AAZTA-FAPI-46 net charge was -1 in comparison with the neutral charge of the DOTA analogue, the obtained value of the logD$_{7.4}$ of the [^{68}Ga]Ga-AAZTA-FAPI-46 was -2,48 ± 0,07. Hence, there seems to be no great influence of the gallium-68 labelled DOTA and AAZTA chelates on the lipophilicity of the FAPi radiopharmaceuticals.

In vitro studies

To confirm the ability to target FAP, the new synthetized [^{68}Ga]Ga-AAZTA-FAPI-46 agent was incubated with HEK293T-FAP cells for competition and internalization experiments. AAZTA chelator substitution seems to not influence the binding affinity to FAP protein, as shown from the potency value in the nanomolar range (IC_{50}=4.61 ± 0.21 nM), obtained by fitting the competition assay data with a nonlinear regression algorithm (GraphPad Prism Software), consistent with previously published data for ^{68}Ga-FAPI-46 and other similar radiolabelled FAPI agents[29]. The internalization results were comparable as well with data reported for ^{68}Ga-FAPI-46 that showed an internalized fraction of 97,18% after 1h of incubation in HT-1080-FAP cells[30].

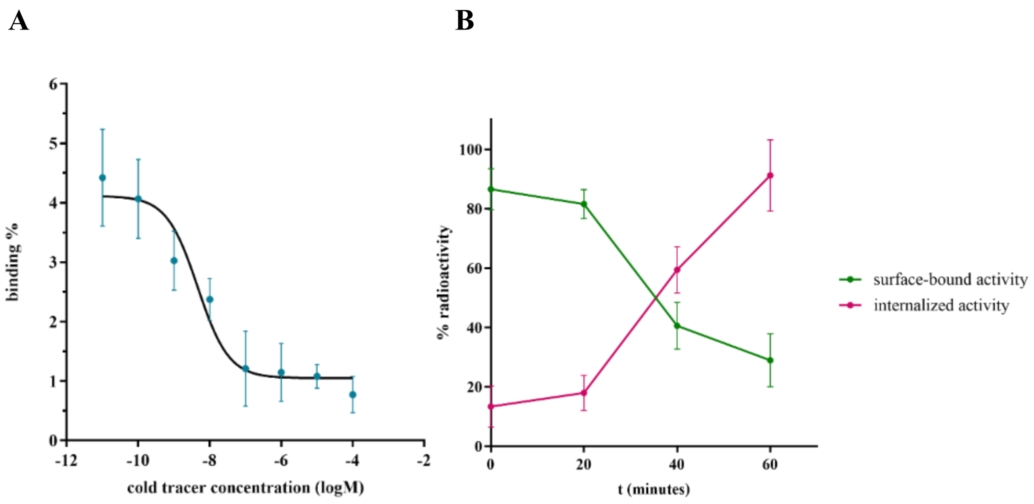

Figure 7 (A) Competition experiment on HEK293T-FAP cells at 4°C for 1h ([^{68}Ga]Ga-AAZTA-FAPI-46 vs unlabelled tracer). (B) Internalization experiment on HEK293T-FAP cells at 37°C for 1h.

CONCLUSIONS

A fast and high-radiochemical yield gallium-68 radiolabelling protocol of AAZTA-FAPI-46 was developed, avoiding heating instrumentations and high-temperature procedure. Hence, the translation of the manual protocol to the automated one was facilitated. The major concern about the replacement of DOTA chelator with the AAZTA chelator was related to the eventual modification on the binding properties of the FAP-inhibitor FAPI-46. Since the IC_{50} results proof that the FAP-specificity remained in the nanomolar range, the AAZTA substitution only led to the advantage of smoother radiolabelling procedure.

APPENDIX II

All chemicals were purchased from Sigma-Aldrich Co. except for the 6-bromoquinoline-4-carboxylic acid that was purchased from Biosynth®Carbosynth. Analytical UPLC-MS were acquired by Waters Acquity® UPLC equipped with TUV and QDa detectors on a BEH C18 column (1.7µm, 2.1x50 mm) equipped with Acquity® UPLC BEH C18 VanGuard™Pre-column (300Å, 1.7µm, 2.1x5mm). ^{1}H-NMR spectrum were carried out on Bruker Avance 400 spectrometer. Preparative HPLC-MS were carried out on a Waters FractionLynx autopurification system equipped with Waters 2996 diode array and Micromass ZQ (ESCI ionization mode) detectors on an Atlantis Prep dC18 OBD™ (5µm, 19x150mm) column. 4,4-difluoro-1-((2-(6-(methyl(3-(piperazin-1-yl)propyl)amino)quinolin-4-yl)-2-oxoethyl)glycyl)pyrrolidine-2-carbonitrile (10) was prepared following a reported procedure[30].

Synthesis of AAZTA-FAPI-46

Synthesis of *tert-butyl 6-bromoquinoline-4-carboxylate* (1-ii)

To a solution of DIC (3.25 ml, 21 mmol, 5.3 eq) in THF (10 ml), *tert*-butanol (2.21 ml, 23.1 mmol, 5.8 eq) and CuI (400 mg, 0.53 mmol, 0.53 eq) were added and the reaction was stirred overnight at room temperature. The suspension was filtrated on celite to eliminate the catalyst and to obtain the *tert-butyl (Z)-N,N'-diisopropylcarbamimidate* (**1**) intermediate. The product was then evaporated *in vacuo* and used without further purification.

To a suspension of *6-bromoquinoline-4-carboxylic acid* (1 g, 3.968 mmol, 1eq) in THF (10 ml), Et_3N was added (255 µl, 1.83 mmol, 0.46 eq) to get a limpid solution. This solution was treated with the intermediate obtained in the previous step and the mixture was stirred overnight at 50°C. The suspension was centrifugated and the supernatant was concentrated *in vacuo*. The residue was purified by chromatography on silica gel column (DCM:MeOH 100:0→ 99:0,5→99:1) to afford the *tert*-butyl ester (719.4 mg, 2.34 mmol, y: 59%).

UPLC-MS: R_t= 9.33 min; $[M+H]^+$ = 307.97 m/z $[M-tBu]^+$ = 252.06 m/z

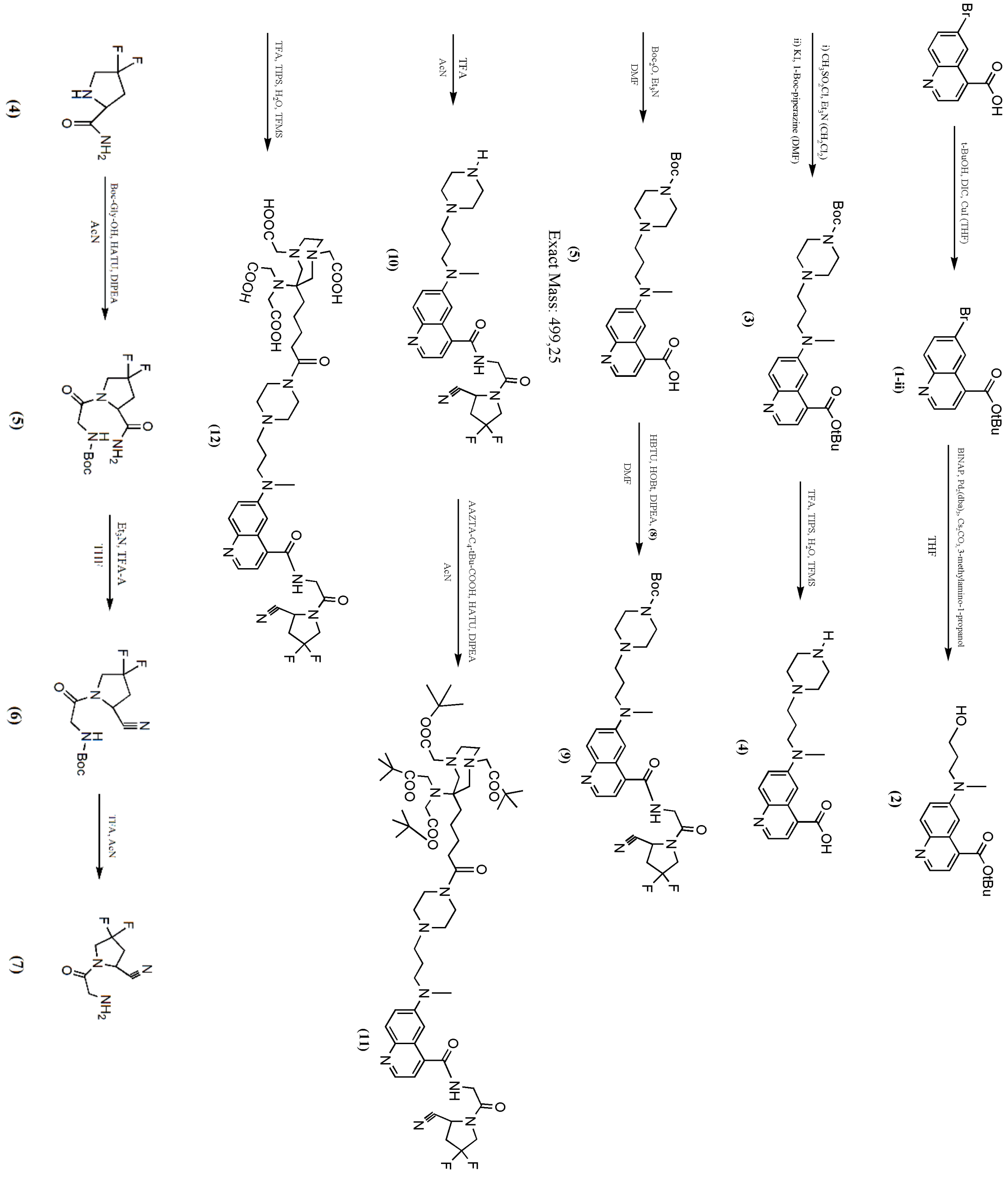

Figure S1 Synthetic scheme of AAZTA-FAPI-46.

Synthesis of *tert-butyl 6-((3-hydroxypropyl)(methyl)amino)quinoline-4-carboxylate* (2)

BINAP (292 mg, 0.468 mmol, 0.2 eq) and $Pd_2(dba)_3$ (215 mg, 0.234 mmol, 0.1 eq) were dissolved in THF (10 ml) and the dark solution was stirred for 10 minutes at 50°C. Then, a solution of *t*-butyl ester intermediate **(1)** (719 mg) in THF (5 ml) was added. The base Cs_2CO_3 (4575 mg, 14.04 mmol, 6eq) and 569 µl of 3-methylamino-1-propanol (5.85 mmol, 2.5 eq) were then added. The mixture was stirred under argon atmosphere at 65 °C overnight. The mixture was concentrated *in vacuo* before purifying by chromatography on silica gel column (DCM:MeOH = 95:5) to afford the desired product (403 mg, 1.28 mmol, y: 55%).

UPLC-MS: R_t= 4.92 min $[M+H]^+$ = 317.31 m/z $[M\text{-}tBu]^+$ = 261.09 m/z

Synthesis of *tert-butyl 6-((3-(4-(tert-butoxycarbonyl)piperazin-1 yl)propyl)(methyl)amino)quinoline-4-carboxylate* (3)

The product (**2**) was dissolved in CH_2Cl_2 (10ml) and Et_3N (586 µl, 4.2 mmol, 3.3eq) were added. CH_3SO_2Cl (129 µl, 1.66 mmol, 1.3 eq) was dropwise added at 0°C and the mixture was stirred at room temperature. Conversion of the -OH group into the mesylate derivate was monitored by TLC (DMC:MeOH = 95:5) and, after the complete conversion was achieved, the 1-*Boc*-piperazine was added (1.25 g, 7.1 mmol, 5.6 eq). The mixture was stirred for 5 minutes and then the solvent was removed under reduced pressure. The mixture was solubilized into 10 ml of DMF and 315 mg of KI (1.9 mmol, 1.5 eq) were added. The temperature of the reaction was increased up to 60°C and the reaction was stirred overnight. The solvent was removed under vacuum and the resulting mixture was suspended in ethyl acetate (10 ml). Then, the organic layer was washed with water (10 ml) and brine (10 ml), in succession. The organic layer was dried over $NaSO_4$ before solvent was removed under vacuum. The residue was purified by chromatography on silica gel column (DCM:MeOH = 98:2) to afford the product (240 mg, 0.496 mmol, y: 39%).

UPLC-MS Rt= 5.34 min; m/z: $[M+H]^+$ = 485.34 , $[M\text{-}Boc]^+$ = 385.41

Synthesis of *6-(methyl(3-(piperazin-1-yl)propyl)amino)quinoline-4-carboxylic acid* (4)

The product (**3**) was reacted with TFA trifluoroacetic acid (2.2 ml), TIPS triisopropylsilane (60 µl), H_20 (60 µl) and TFMSA trifluoromethanesulfonic acid (120 µl) at room temperature for 1 hour or until the reaction was completed as checked-out by TLC (DCM:MeOH = 9:1). After removal of the solvent, the residue was dissolved in diethyl ether to further eliminate TFA residues and to get the precipitation of the red product. The ether was discarded after centrifugation, the product was dissolved into water and lyophilized to afford a red powder (161.1 mg, 0.491 mmol, y: 99%).

UPLC-MS Rt=1.01 m/z: $[M+H]^+ = 329.23$

Synthesis of *6-((3-(4-(tert-butoxycarbonyl)piperazin-1-yl)propyl)(methyl)amino)quinoline-4-carboxylic acid* (5)

The deprotected compound (**4**) was dissolved in DMF (5 ml) and was reacted with Boc_2O (146 mg, 0.67 mmol, 1.35 eq) and Et_3N (121 µl, 0.868 mmol,1.75eq) at room temperature for 2h. The reaction progress was monitored by TLC (DCM: MeOH = 9:1) and, once the completion was achieved, the solvent was removed under vacuum. The residue was dissolved in diethyl ether to further eliminate DMF and to afford the precipitation of the red product. Then, by discarding ether after centrifugation, the product was allowed to air dry. The product was used without further purification.

UPLC-MS Rt= 3.29 min; m/z $[M+H]^+ = 429.44$, $[M\text{-}Boc]^+ = 329.23$

***Synthesis of tert-butyl (2-(2-carbamoyl-4,4-difluoropyrrolidin-1-yl)-2-oxoethyl) carbamate* (6)**

To a suspension of Boc-Gly-OH (1.033 g, 5.895 mmol, 1.1 eq) in acetonitrile (10 ml), 2.242 g of HATU (5.895 mmol, 1.1 eq) and 3.82 ml of DIPEA (21.436 mmol, 4 eq) were dissolved to get a limpid solution; then, 1 g of *4,4-difluoropyrrolidine-2-carboxamide hydrochloride* was added and the solution was stirred at room temperature for 3 hours or until TLC (DCM: MeOH = 97:3) showed the reaction was completed. The suspension obtained was centrifuged and the whitish solid was washed twice with DCM. The solid obtained was used without further purification (752 mg, 2.447 mmol, y:46%).

UPLC-MS R_t= 3.60 min; m/z $[M+Na]^+ = 330.02$, $[M\text{-}Boc]^+ = 208.19$

***Synthesis of tert-butyl (2-(2-cyano-4,4-difluoropyrrolidin-1-yl)-2-oxoethyl) carbamate* (7)**

The previously obtained compound was dissolved into THF (7ml) and 1.7 ml of pyridine (20.8 mmol, 8.5 eq) were added. After leading the temperature to 0°C, a solution of TFA-A trifluoroacetic anhydride (579 µl, 4.16 mmol, 1.7 eq) in THF (3 ml) was dropwise added. The reaction was stirred at 0°C for 90 minutes or until TLC (DCM:MeOH=97.3) showed the conversion of amino group into nitrile group was completed. The solvent was removed under vacuum, the solid was dissolved in ethyl acetate and the organic layer was washed with HCl 2M (3x25ml), a saturated solution of $NaHCO_3$ (30ml) and brine (30ml). The organic layer was dried over $NaSO_4$ before removal of the solvent under vacuum (581 mg, 2.01 mmol, y: 82%).

UPLC-MS R_t= 5.01 min; m/z $[M+Na]^+$ = 312.05 , $[M-Boc]^+$ = 190.08

Synthesis of 4,4-difluoro-1-glycylpyrrolidine-2-carbonitrile **(8)**

To a suspension of (**7**) in acetonitrile, *p*-toluensulfonic acid (574 mg, 3.015 mmol, 1.5eq) was slowly added. The reaction mixture was stirred at room temperature for 24h and, after removing the solvents under reduced pressure, diethyl ether was added at 0°C to get a whitish solid precipitation. After centrifugation, the supernatant was discarded and the solid was used without further purification (372 mg,1.97 mmol, y: 98%).

UPLC-MS R_t= 1.42 min; m/z $[M-Boc]^+$ = 190.08

Synthesis of ***tert-butyl 4-(3-((4-((2-(2-cyano-4,4-difluoropyrrolidin-1-yl)-2-oxoethyl) carbamoyl) quinolin-6-yl)(methyl)amino)propyl)piperazine-1-carboxylate*** **(9)**

The carboxylic acid compound **(5)** was dissolved in DMF (6 ml) and then HOBt (188mg, 1.39 mmol, 2.8 eq), HBTU (235 mg, 0.62 mmol, 1.25 eq) and DIPEA (111 µl,0.62 mmol, 2.8 eq) were added. The reaction mixture was reacted for 15 minutes before adding a solution of the amine compound **(8)** (135 mg, 0.714 mmol, 1.44 eq) in DMF (2ml). The mixture was reacted for 1 h and, once the completion was achieved, the solvent was removed under vacuum and the product was obtained following the precipitation with diethyl ether, as described before. The solid was then purified by chromatography on silica gel column (DCM:MeOH=9:1) to afford a red solid (281 mg, 0.469 mmol, y: 95%).

UPLC-MS Rt= 4.90 min m/z $[M+H]^+$ = 600.26 , $[M-Boc]^+$ = 500.15

Synthesis of *4,4-difluoro-1-((2-(6-(methyl(3-(piperazin-1-yl)propyl)amino)quinolin-4-yl)-2-oxoethyl)glycyl)pyrrolidine-2-carbonitrile* (10)

The previously obtained compound (**9**) was dissolved in acetonitrile (5ml) and reacted with trifluoroacetic acid (10ml) for 1 h, until the deprotection of Boc-group was completed. After reducing solvents under vacuum, the product was precipitated in diethyl ether to afford, after centrifugation, a red powder. The procedure described above was followed. The product was used without further purification (240mg, 0.442 mmol, y: 94 %).

UPLC-MS Rt= 0.87 min, m/z $[M+H]^+$ = 500.20 $[M+2H]^+$ = 250.66

Synthesis of *AAZTA-C_4-(tBu)-FAPi-46* (11)

198 mg of 5-(6-(bis(2-(tert-butoxy)-2-oxoethyl)amino)-1,4-bis(2-(tert-butoxy)-2-oxoethyl)-1,4-diazepan-6-yl)pentanoic acid (0.296 mmol,1.1 eq) were dissolved in 3 ml of ACN and then HATU (113mg, 0.296 mmol, 1.1 eq) and DIPEA (239 µl, 1.34 mmol, 5 eq) were added. After 5 minutes, a solution of compound (**10**) (134 mg, 0.269 mmol, 1 eq) in ACN (2ml) was added to the mixture and the reaction was reacted for 1 hour. After the coupling was completed, the solvent was reduced under vacuum. The mixture was purified by chromatography on silica gel column (DCM:MeOH=9:1) to afford the isolated (**11**) compound (110 mg, 0.0951mmol, y: 35 %).

UPLC-MS Rt= 7.78 min $[M+H]^+$ = 1153.44 m/z, $[M+2H]^+$ = 577.36 m/z

Synthesis of *AAZTA-C_5-FAPi-46* (12)

Finally, the *tert*-butyl groups of AAZTA chelator had to be deprotected. Herein, the compound (**11**) was dissolved in DCM (4 ml) and TFA (4ml) and TIPS (80 µl, 1%) were added. The reaction mixture was shacked for 24 h and, once the total deprotection was achieved, the solvent was removed under reduced pressure. The product was obtained following the precipitation procedure with diethyl ether. After discarding the diethyl ether, the red powder was dissolved in water and lyophilized (81 mg, 0.087 mmol, y: 92%).

UPLC-MS Rt= 3.21 min $[M+H]^+$ = 929.53 m/z, $[M+2H]^+$ = 465.35 m/z

UPLC-MS analytical method

Injection volume 5 µl

Flow 0.4 ml/min

t	% H_2O (0,1% TFA)	%CH_3CN
0	95	5
14	0	100

HPLC-MS preparative method

Injection volume 100 µl

[45 mg/ml]

Flow 20 ml/min

t	% H_2O (0,1% TFA)	%CH_3CN
0	95	5
5	95	5
9	85	15
16	85	15
20	40	60
23	0	100

^{1}H NMR spectrum

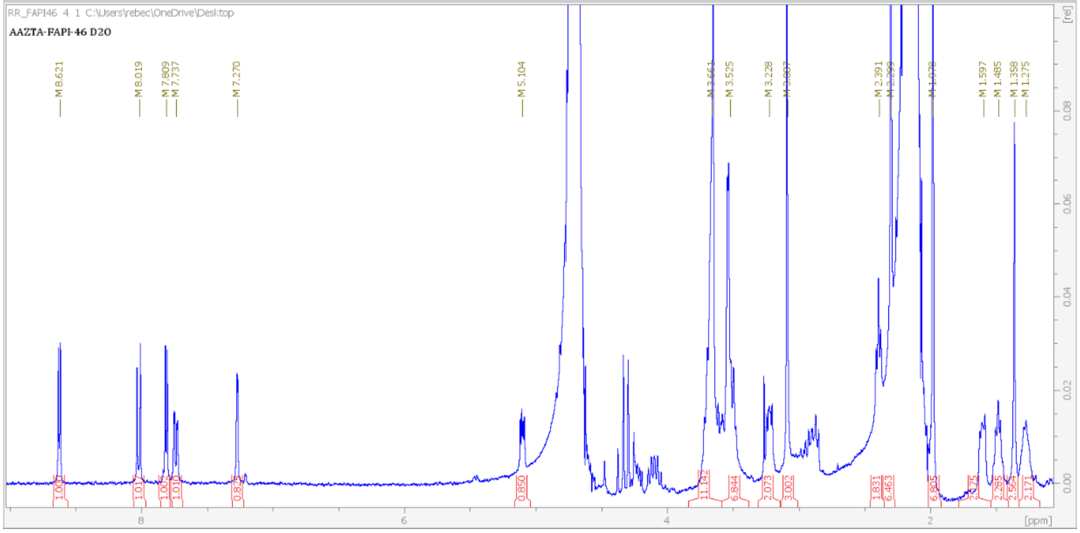

Figure S2 ^{1}H-NMR (400 MHz) spectrum of AAZTA-FAPI-46 in D_2O (T=298K). Chemicals shift (in ppm) and integrations are reported: δ 1.27 (m, 2H), δ 1.36 (s, 2H), δ 1.49 (t, 2H), δ 1.60 (t, 2H), δ 1.98-2.39 (TFA residues), 3.09 (s, 3H), 3.23 (m, 2H), 3.53-3.66 (18H), δ 3.81 (m, 3H), 5.10 (m, 1H), 7.27 (d, 1H), 7.74 (d, 1H), 7.81 (d, 1H), 8.01 (d, 1H), 8.62 (d, 1H).

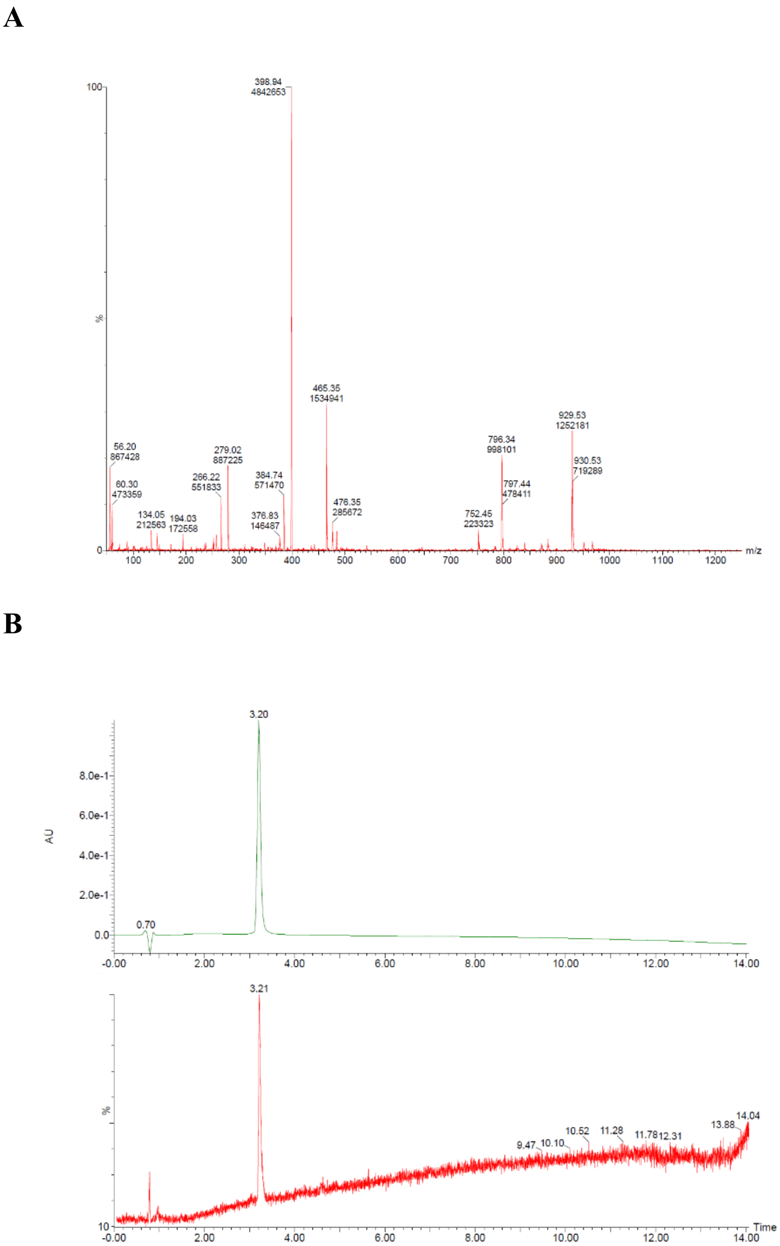

Figure S3 (A) Chromatogram acquired at 254 nm of purified AAZTA-FAPI-46 on Acquity® UPLC BEH C18 column. (B) ESI(+) mass spectrum of AAZTA-FAPI-46.

Buffers for radiolabeling procedure

HEPES 0,4M for pH=3,5; NaOAc 0,4M for pH ranging from 4 to 5.

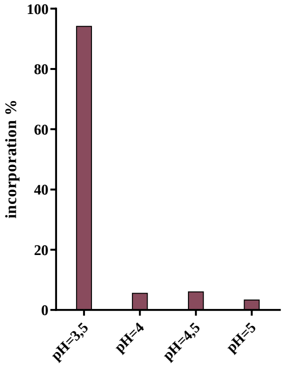

Figure S4 ^{68}Ga-incorporation (sum of labelled AAZTA-FAPI46 and colloidal contribute) at different pH values (RT, 15 minutes, 40 µM) assessed by radio-TLC.

References

[1] G. Nagy, D. Szikra, G. Trencsényi, A. Fekete, I. Garai, A.M. Giani, R. Negri, N. Masciocchi, A. Maiocchi, F. Uggeri, I. Tóth, S. Aime, G.B. Giovenzana, Z. Baranyai, AAZTA: An Ideal Chelating Agent for the Development of44Sc PET Imaging Agents, Angew. Chemie - Int. Ed. 56 (2017) 2118–2122.

[2] J.P. Sinnes, U. Bauder-Wüst, M. Schäfer, E.S. Moon, K. Kopka, F. Rösch, 68Ga, 44Sc and 177Lu-labeled AAZTA5-PSMA-617: synthesis, radiolabeling, stability and cell binding compared to DOTA-PSMA-617 analogues, EJNMMI Radiopharm. Chem. 5 (2020).

[3] M.I. Tsionou, C.E. Knapp, C.A. Foley, C.R. Munteanu, A. Cakebread, C. Imberti, T.R. Eykyn, J.D. Young, B.M. Paterson, P.J. Blower, M.T. Ma, Comparison of macrocyclic and acyclic chelators for gallium-68 radiolabelling, RSC Adv. 7 (2017) 49586–49599.

[4] K.D. Klika, C. Da Pieve, K. Kopka, G. Smith, A. Makarem, Synthesis and application of a thiol-reactive HBED-type chelator for development of easy-to-produce Ga-radiopharmaceutical kits and imaging probes, Org. Biomol. Chem. 19 (2021) 1722–1726.

[5] J.D. Young, V. Abbate, C. Imberti, L.K. Meszaros, M.T. Ma, S.Y.A. Terry, R.C. Hider, G.E. Mullen, P.J. Blower, 68Ga-THP-PSMA: A PET Imaging Agent for Prostate Cancer Offering Rapid, Room-Temperature, 1-Step Kit-Based Radiolabeling, J. Nucl. Med. 58 (2017) 1270–1277.

[6] J.P. Sinnes, J. Nagel, B.P. Waldron, T. Maina, B.A. Nock, R.K. Bergmann, M. Ullrich, J. Pietzsch, M. Bachmann, R.P. Baum, F. Rösch, Instant kit preparation of 68Ga-radiopharmaceuticals via the hybrid chelator DATA: clinical translation of [68Ga]Ga-DATA-TOC, EJNMMI Res. 9 (2019) 48.

[7] G. Gugliotta, M. Botta, G.B. Giovenzana, L. Tei, Fast and easy access to efficient bifunctional chelators for MRI applications, Bioorganic Med. Chem. Lett. 19 (2009) 3442–3444.

[8] S. Aime, L. Calabi, C. Cavallotti, E. Gianolio, G.B. Giovenzana, P. Losi, A. Maiocchi, G. Palmisano, M. Sisti, [Gd-AAZTA]-: A new structural entry for an improved generation of MRI contrast agents, Inorg. Chem. 43 (2004) 7588–7590.

[9] Z. Baranyai, F. Uggeri, A. Maiocchi, G.B. Giovenzana, C. Cavallotti, A. Takács, I. Tóth, I. Bányai, A. Bényei, E. Brucher, S. Aime, Equilibrium, kinetic and structural studies of AAZTA complexes with Ga3+, In3+ and Cu2+, Eur. J. Inorg. Chem. (2013) 147–162.

[10] L. Manzoni, L. Belvisi, D. Arosio, M.P. Bartolomeo, A. Bianchi, C. Brioschi, F. Buonsanti, C. Cabella, C. Casagrande, M. Civera, M. De Matteo, L. Fugazza, L. Lattuada, F. Maisano, L. Miragoli, C. Neira, M. Pilkington-Miksa, C. Scolastico, Synthesis of Gd and 68Ga Complexes in Conjugation with a Conformationally Optimized RGD Sequence as Potential MRI and PET Tumor-Imaging Probes, ChemMedChem. 7 (2012) 1084–1093.

[11] A. Vágner, C. D'Alessandria, G. Gambino, M. Schwaiger, S. Aime, A. Maiocchi, I. Tóth, Z. Baranyai, L. Tei, A rigidified AAZTA-like ligand as efficient chelator for 68Ga radiopharmaceuticals, ChemistrySelect. 1 (2016) 163–171.

[12] J. Calais, FAP: The next billion dollar nuclear theranostics target?, J. Nucl. Med. 61 (2020) 163–165.

[13] P. O'Brien, B.F. O'Connor, Seprase: an overview of an important matrix serine protease,

Biochim. Biophys. Acta. 1784 (2008) 1130–1145.

[14] M.T. Levy, G.W. McCaughan, C.A. Abbott, J.E. Park, A.M. Cunningham, E. Muller, W.J. Rettig, M.D. Gorrell, Fibroblast activation protein: A cell surface dipeptidyl peptidase and gelatinase expressed by stellate cells at the tissue remodelling interface in human cirrhosis, Hepatology. 29 (1999) 1768–1778.

[15] E.J. Hamson, F.M. Keane, S. Tholen, O. Schilling, M.D. Gorrell, Understanding fibroblast activation protein (FAP): Substrates, activities, expression and targeting for cancer therapy, Proteomics - Clin. Appl. 8 (2014) 454–463.

[16] A.A. Fitzgerald, L.M. Weiner, The role of fibroblast activation protein in health and malignancy, Cancer Metastasis Rev. 39 (2020) 783–803.

[17] R.M. Bremnes, T. Dønnem, S. Al-Saad, K. Al-Shibli, S. Andersen, R. Sirera, C. Camps, I. Marinez, L.T. Busund, The role of tumor stroma in cancer progression and prognosis: Emphasis on carcinoma-associated fibroblasts and non-small cell lung cancer, J. Thorac. Oncol. 6 (2011) 209–217.

[18] K.H. Williams, A.J. Viera De Ribeiro, E. Prakoso, A.S. Veillard, N.A. Shackel, Y. Bu, B. Brooks, E. Cavanagh, J. Raleigh, S. V Mclennan, G.W. Mccaughan, W.W. Bachovchin, F.M. Keane, A. Zekry, S.M. Twigg, M.D. Gorrell, Lower serum fibroblast activation protein shows promise in the exclusion of clinically significant liver fibrosis due to non-alcoholic fatty liver disease in diabetes and obesity, (2015).

[19] Z. Wang, J. Wang, T. Lan, L. Zhang, Z. Yan, N. Zhang, Y. Xu, Q. Tao, Role and mechanism of fibroblast-activated protein-α expression on the surface of fibroblast-like synoviocytes in rheumatoid arthritis, Front. Immunol. 14 (2023).

[20] Y. Waumans, L. Baerts, K. Kehoe, A.M. Lambeir, I. De Meester, The dipeptidyl peptidase family, prolyl oligopeptidase and prolyl carboxypeptidase in the immune system and inflammatory disease, including atherosclerosis, Front. Immunol. 6 (2015) 146787.

[21] S.W.M. Van Den Borne, J. Diez, W.M. Blankesteijn, J. Verjans, L. Hofstra, J. Narula, Myocardial remodeling after infarction: the role of myofibroblasts, Nat. Rev. Cardiol. 7 (2010) 30–37.

[22] X. Hua, L. Yu, X. Huang, Z. Liao, Q. Xian, Expression and role of fibroblast activation protein-alpha in microinvasive breast carcinoma, Diagn. Pathol. 6 (2011) 1–7.

[23] A. Costa, Y. Kieffer, A. Scholer-Dahirel, F. Pelon, B. Bourachot, M. Cardon, P. Sirven, I. Magagna, L. Fuhrmann, C. Bernard, C. Bonneau, M. Kondratova, I. Kuperstein, A. Zinovyev, A.M. Givel, M.C. Parrini, V. Soumelis, A. Vincent-Salomon, F. Mechta-Grigoriou, Fibroblast Heterogeneity and Immunosuppressive Environment in Human Breast Cancer, Cancer Cell. 33 (2018) 463-479.e10.

[24] C. Kratochwil, P. Flechsig, T. Lindner, L. Abderrahim, A. Altmann, W. Mier, S. Adeberg, H. Rathke, M. Röhrich, H. Winter, P.K. Plinkert, F. Marme, M. Lang, H.U. Kauczor, D. Jäger, J. Debus, U. Haberkorn, F.L. Giesel, 68Ga-FAPI PET/CT: Tracer uptake in 28 different kinds of cancer, J. Nucl. Med. 60 (2019) 801–805.

[25] A. De Decker, G. Vliegen, D. Van Rompaey, A. Peeraer, A. Bracke, L. Verckist, K. Jansen, R. Geiss-Friedlander, K. Augustyns, H. De Winter, I. De Meester, A.M. Lambeir, P. Van Der Veken, Novel Small Molecule-Derived, Highly Selective Substrates for Fibroblast Activation Protein (FAP), ACS Med. Chem. Lett. 10 (2019) 1173–1179.

[26] A. Altmann, U. Haberkorn, J. Siveke, The latest developments in imaging of fibroblast activation protein, J. Nucl. Med. 62 (2021) 160–167.

[27] L. Xin, J. Gao, Z. Zheng, Y. Chen, S. Lv, Z. Zhao, C. Yu, X. Yang, R. Zhang, Fibroblast Activation Protein-α as a Target in the Bench-to-Bedside Diagnosis and Treatment of Tumors: A Narrative Review, Front. Oncol. 11 (2021).

[28] S. Kuyumcu, Y. Sanli, R.M. Subramaniam, Fibroblast-Activated Protein Inhibitor PET/CT: Cancer Diagnosis and Management, Front. Oncol. 11 (2021) 1–10.

[29] T. Lindner, A. Loktev, A. Altmann, F. Giesel, C. Kratochwil, J. Debus, D. Jäger, W. Mier, U. Haberkorn, Development of quinoline-based theranostic ligands for the targeting of fibroblast activation protein, J. Nucl. Med. 59 (2018) 1415–1422.

[30] A. Loktev, T. Lindner, E.M. Burger, A. Altmann, F. Giesel, C. Kratochwil, J. Debus, F. Marmé, D. Jäger, W. Mier, U. Haberkorn, Development of fibroblast activation protein-targeted radiotracers with improved tumor retention, J. Nucl. Med. 60 (2019) 1421–1429.

[31] S. Ballal, M.P. Yadav, V. Kramer, E.S. Moon, F. Roesch, M. Tripathi, S. Mallick, S.T. ArunRaj, C. Bal, A theranostic approach of [68Ga]Ga-DOTA.SA.FAPi PET/CT-guided [177Lu]Lu-DOTA.SA.FAPi radionuclide therapy in an end-stage breast cancer patient: new frontier in targeted radionuclide therapy, Eur. J. Nucl. Med. Mol. Imaging. (2020) 1–3.

Chapter 3

In vitro and *in vivo* validation of optical probes based on FAPI-46 for near-infrared fluorescence imaging

ABSTRACT

FAP (Fibroblast Activation Protein) is a pan-cancer target, useful for image ideally all epithelial cancers. This work aims to develop, characterize, in *vitro* and *in vivo* validate two novel FAP-targeted probes for optical imaging. IRDye800CW and FNIRTag were conjugated to the NH-precursor of the well-known FAP inhibitor FAPI-46, widely employed in nuclear medicine. Besides synthesis, UV-Vis and fluorometric measurements, the stability was checked (serum stability and photobleaching), the albumin binding was evaluated, the *in vitro* binding on FAP expressing cells was tested as well as the *in vivo* fluorescence imaging was performed on TUBO tumor-bearing mice.

INTRODUCTION

FAP (Fibroblast Activation Protein) is a leading theranostic biomarker since its crucial role in angiogenesis, growth and progression in cancer[1]. FAP is a transmembrane serine protease overexpressed by CAFs (Cancer Associated Fibroblasts) in more than 90% of epithelial cancers[2], including breast[3,4] colon[4,5] and pancreatic[4,6] tumour. Thus, FAP has been considered as a pan-cancer target in several preclinical approaches and clinical trials. Considering that, the development of diagnostic approaches by targeting FAP would be of great importance. Optical imaging is a non-invasive technique based on interaction of light with tissues that guide the clinician's decision making in real-time. In fact, between pre-operative imaging modalities and intra-operative reality, intra-operative imaging represents a key player to improve cancer surgical outcomes[7]. Surgical intervention remains a primary treatment for patients with solid tumors but incomplete resections or unnecessary removal of healthy tissues is significantly unbeneficial for the prognosis of patients. In breast cancer, for example, many of which are non-palpable, margin positivity rates range from 5 to 49%[8]. Tumor-targeted, near-infrared fluorescent (NIRF) imaging is an emerging field of real-time intraoperative cancer imaging based on tumor-targeted NIRF dyes and has become relevant also in breast cancer as demonstrated from clinical trials largely in phase 1-2[9]. Besides undeniable advantages such as the non-invasive nature, the immediate response during surgery intervention, the tunability of probes to obtain functional and molecular information, the use of non-ionizing radiation, optical imaging is affected by some criticisms. Among these, fluorophore conjugation often alters the properties of both the fluorophore and the molecule to which it is attached[10]. Specifically, important parameters such as brightness, target binding, *in vivo* stability, and pharmacokinetics (PK) are often impacted[11]. Thus, the development of novel tumor-targeted NIRF dyes has increased interest in the FGS (Fluorescence Guided Surgery) field. In an effort to identify a pan-tumor marker for use in imaging all solid tumors, several research groups have investigated FAP-targeting ligands for fluorescence imaging of tumors. Nevertheless, some of them suffer from unwanted accumulation in healthy tissues and still others exhibit short tumor retention times[12,13]. More recently, Mukkamala and coworkers[14] have successfully developed the FAP-conjugated S0456 dye (**Figure 1**) capable of imaging most solid tumors (human triple negative breast cancer, human colorectal cancer, human glioblastoma, human head and neck cancer, human pancreatic cancer, murine breast cancer and human nasopharyngeal cancer), demonstrating the notable relevance of FAP-imaging in the optical imaging field. To further exploit this need, we developed two novel fluorescent probes based on FAPI-46 structure, one of the most promising FAP-inhibitors showing nanomolar affinity for FAP and high tumour-to-background ratio in PET imaging[15]. The conjugated fluorophores object of this work were IRDye800CW and FNIRTag in account to their different charge (IRDye800CW has charge = -3 while FNIRTag has zwitterionic structure) and structure peculiarities. In particular, IRDye800CW has a polyanionic structure (charge = -3) and, although its widely used in clinical trials, suffer from aspecific *in vivo* binding that prevents to maximize the fluorescence intensity at the target site. FNIRTag has a zwitterionic structure which allows for an improved tumour-to-background ratio and a minimized affinity for serum proteins. On these premises, this work aims to synthesize and validate *in vitro* and *in vivo* two

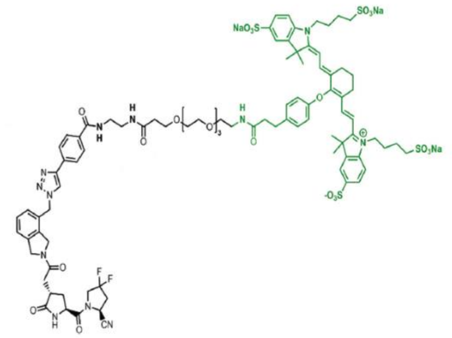

Figure 1 Chemical structure of FLT-S-S0456 developed by Mukkamala *et al.* [14]

novel FAP-targeting fluorescent probes for near-infrared fluorescence imaging applications.

EXPERIMENTAL SECTION

Chemicals

All chemicals were purchased from Sigma Aldrich. All solvents for UPLC-MS analysis and purification procedure were purchased from VWR. Activated NHS-esther cyanines (FNIR-Tag-NHS, IRDye800CW-NHS) were obtained from Bio-Techne. UPLC-MS analysis was obtained on Waters system (Acquity UPLC H class Plus). Purification procedures were performed on a AKTA Purifier HPLC System. See Appendix III for analytical and preparative methods information. UV/Vis spectrophotometric measurements were performed on a UV/Vis spectrophotometer (6715, Jenway). Fluorescence measurements were performed on a FluoroMax-4 Spectrofluorometer (Horiba Scientific).

Cells cultures and in vitro experiments

Seronorm™ (human serum) was purchased from Sero AS. Human serum albumin was purchased from Sigma Aldrich. Mammary carcinoma TUBO cells were kindly provided by Professor Cavallo research group. HEK293T-FAP stable transfected cells were kindly provided by Dr. Lidia Avalle (Professor Valeria Poli research group).

Animals

Balb-C female mice for *ex vivo* FAP assessment were obtained from the animal facility of the Department of Molecular Biotechnology and Health Sciences (University of Turin, Italy). Athymic mice for *in vivo* NIRF imaging and biodistribution studies were purchased from Envigo.

Synthesis and purification

The piperazine-precursor of FAPI-46, previously synthetized according to already published procedure (Chapter 2 – Appendix II), was conjugated *via* amidic bond with N-hydroxisuccinimidil-esther of IRDye800CW or FNIRTag fluorescent molecules (**Figure 2**). After evaporating the solvent under reduced pressure, 500 µl of purified water were added to the crude of reaction and the solution loaded into the preparative chromatographic column. For the detailed purification procedures see Appendix III at the end of this Chapter. The two synthetized molecules were obtained as green powder. The purity of compounds (> 99%) was assessed through UPLC-MS measurements (**Figure S1**).

UV-Vis, fluorescence measurements, and fluorescence phantom imaging

To quantify the obtained compounds, three different dilutions for each molecule were prepared in PBS and the relative absorbance values were measured. The Lambert-Beer equation was used to calculate the concentration of each solution by using the molar coefficient of the unconjugated fluorophore, upon the assumption that the conjugation of each fluorophore to the NH-precursor of FAPI-46 do not affect the ε value of the fluorophores (reported in **Table 1**).

The optical properties of these conjugates were analysed by spectrophotometric and fluorometric analysis. Absorption spectra were recorded at different concentration both in PBS pH=7.4 and in PBS:MeOH (1:1).

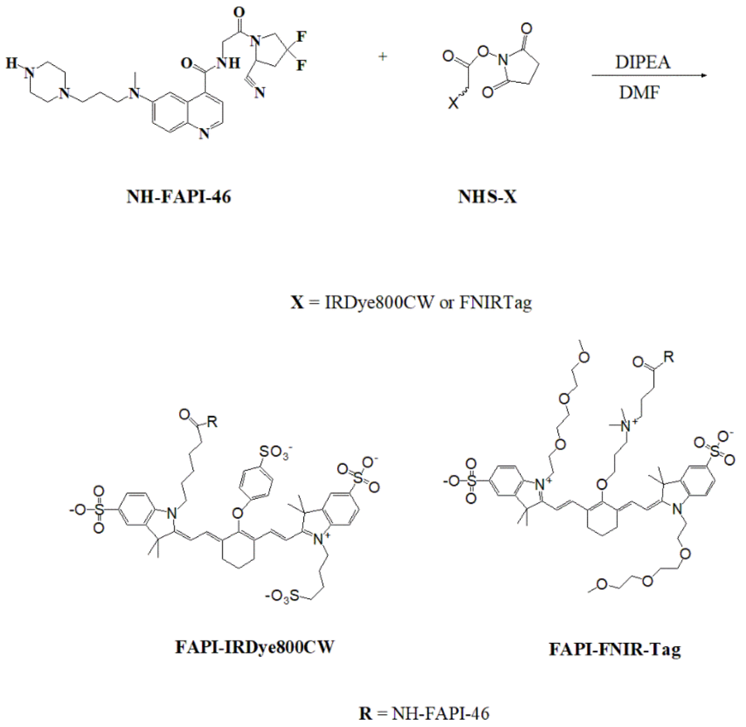

Figure 2 Synthetic protocol for FAPI-IRDye800CW and FAPI-FNIRTag. The reactions were conducted using 1 eq of fluorophore (NHS esther), 2.1 eq of FAPI-46 (NH precursor), 6 eq of DIPEA, DMF as solvent, at room temperature for 3 hours in the dark.

fluorescent dyes	ε PBS pH=7,4 ($M^{-1}cm^{-1}$)
FNIR-Tag	200000
IRDye800CW	240000

Table 1. Absorption coefficients used to quantify the two fluorescent-FAPI-46 compounds**.**

Fluorescence emission and excitation spectra were recorded at different concentrations both in PBS pH=7.4 and PBS:MeOH (1:1). The set wavelengths were listed in **Table 2**[16].

fluorescent dyes	λ_{abs}	λ_{em}	λ_{ex}
FNIR-Tag	765	788	730
IRDye800CW	774	790	740

Table 2. Absorption and excitation wavelengths of the fluorophores.

Phantom imaging of FAPI-IRDye800CW and FAPI-FNIRTag was performed into a 96-multiwell plate (0-500 nM) by employing an excitation filter of 740 nm and an emission filter of 790 nm (IVIS - Perkin Elmer). Fluorescence signals in average radiant efficiency [p/s/cm²/sr]/[µW/cm²] were plotted as a function of dyes concentration (6.25-500 nM).

Stability

Chemical stability was investigated by UPLC-MS measurements. Fluorescent compounds were incubated in human serum at 37°C. After selected incubation time (0, 2, 6, 24, 48 hours), acetonitrile was added for proteins precipitation, centrifugation was performed at 13000 rpm for 10 minutes and the supernatant was analysed by UPLC-MS. The fluorescent compounds final concentration was set to 5 µM. Serum UPLC-MS measurement was performed to consider the MS signals serum contribution.

Photostability was determined by irradiating the compounds for 2 h with a 200 W xenon lamp every 60 s (120 points). The photobleaching was evaluated through the decrement of fluorescence intensity by plotting the normalized intensity fluorescence (emission values divided by the initial fluorescence for each compound) as a function of irradiating time.

Albumin binding

Serum proteins binding measurements were performed using human serum albumin with a purity of ≥ 97% (Sigma Aldrich). The products were incubated at a final concentration of 0,15 µM with increasing concentrations of albumin (0 - 30 µM).

Incubation was conducted in PBS at room temperature for 1 h; subsequently, the fluorescence emission profile was recorded, employing the same protocol as described previously for fluorescence measurements. The normalized fluorescence emission for the maximum value found was plotted against albumin concentration. The data were fitted with the equation ($y=F_{bound}*(F_{bound}-F_{free}) + F_{free}*[dye]$) from which the bond dissociation constant was derived.

Cell lines

HEK293T-FAP transfected cells were maintained in DMEM 1 g/L glucose supplemented with 10% fetal bovine serum and 2µg/ml puromycin. HEK293T cells were maintained in DMEM 1 g/L glucose supplemented with 10% fetal bovine serum. TUBO cell lines were maintained in DMEM supplemented with 20% fetal bovine serum. Cells were grown in a humidified incubator with 5% CO_2 at 37 °C.

Animal studies

For the *ex vivo* assessment of FAP expression, 5-weeks old female Balb-C mice (n=5) were subcutaneously injected in the right shoulder with 10^5 TUBO cells suspended in 100 µl of PBS. Tumor growth was checked twice a week by a caliber and tumor tissues were excised when the tumor size reached 400 mm^3. For *in vivo* imaging (n=4) and biodistribution studies (n=3), 5-weeks old female athymic mice were subcutaneously injected in the right shoulder with 10^5 TUBO cells suspended in 100 µl of PBS. 5 nmol of FAPI-IRDye800CW and FAPI-FNIRTag were intravenously injected in the tail vein and fluorescence imaging (IVIS Spectrum, Perkin Elmer) was performed at different time points (0, 1, 2, 4, 6, 24, 48, 72, 96, 168 h p.i.). For biodistribution studies, 5 nmol of the dyes were intravenously injected in the tail vein, the mice were euthanized by cervical dislocation 24 h p.i., the main organs were excised, and the quantification of the signal was performed by measuring the average radiance efficiency by the IVIS Spectrum. ROI (region of interest) analysis was performed to obtain a fluorescence signal quantification.

Flow cytometry

For uptake experiments, 4×10^5 HEK293T-FAP cells were incubated with fluorescent compound (FAPI-IRDye800CW or FAPI-FNIRTag) at a final concentration of 0.5 µM or with mouse Fibroblast Activation Protein antibody (MAB9727) at a final concentration of 0.25 µg/10^6 cells. Donkey anti-Rat IgG (H+L) Highly Cross-Adsorbed Secondary Antibody, Alexa Fluor™ 488 was used as secondary antibody (1:2000). For competition experiments, NH-FAPI46 unconjugated was used (100x, 50 µM). HEK293T cell line was employed as negative control.

To assess FAP expression on tumor tissues, MAB9727 was used as anti-FAP Antibody (0,25 µg/10^6 cells) and A21208 Donkey anti-Rat IgG (H+L) Highly Cross-Adsorbed Alexa Fluor™ 488 was used as secondary antibody (1:1000).

Immunohistochemistry

To assess FAP expression, tumor tissues were incubated with anti-FAP antibody (ab207178) overnight at 4°C (1:100). Goat Anti-Rabbit IgG H&L (HRP) (ab97051) was incubated for 1h at room temperature (1:200).

RESULTS AND DISCUSSION

UV-Vis and fluorescence measurements

The photo-physical properties of the two developed compounds were investigated. Since it is known that conjugation of a fluorophore can often lead to modification of its properties[17], especially in terms of aggregation or quantum yield, two different solvents, PBS (50 mM, pH=7.4) and PBS:MeOH (1:1), were used. Through absorbance measurements, each synthesized product was also quantified, using the molar extinction coefficients known from the literature, upon the assumption that the ε values of the dyes were not affected by the conjugation.

As depicted in **Figure 3**, the emission spectra revealed a higher fluorescence for FAPI-FNIRTag than FAPI-IRDye800CW (**Figure 3B**) at the same concentrations. Moreover, the absorbance values are found to be higher in PBS:MeOH (**Figure S2**) for both of the dyes; this may be due to the action of methanol on breaking the hydrogen bonds present in the aggregates, as previously shown by Luciano et al. [16], or to a change in the chemical surroundings.

As for the excitation spectra (**Figures S3** and **S4**), however, it is possible to observe, as already shown by Luciano *et. al* [16], the presence of a hypsochromic band (shifted toward blue), probably related to the formation of small H-aggregates, at around 700 nm. The H-aggregates represent the most common aggregates for heptamethine cyanine dyes molecules due to the face-to-face stacking[18].

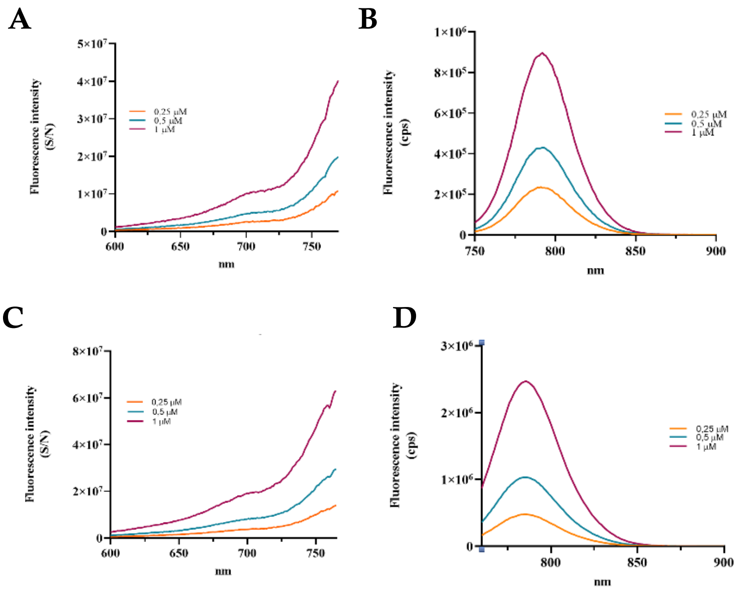

Figure 3 Fluorescence excitation spectra in PBS (pH=7.4) of (A) FAPI-IRDye800CW and (C) FAPI-FNIRTag. Fluorescence emission spectra in PBS (pH=7.4) of (B) FAPI-IRDye800CW and (D) FAPI-FNIRTag.

To investigate this band intensity behavior by increasing the dye concentration, the ratio of the hypsochromic band to the band due to the monomer of each compound was calculated in both [19,20] ratio is almost unchanged as the concentration increases so an increment in the aggregation phenomenon would not seem to be present at the investigated concentrations (0-1 µM).

Phantom imaging analysis confirmed the linear correlation between fluorescence and concentration (in the examined concentrations) and a higher fluorescence for FAPI-FNIRTag, as reported in **Figure 4A**. Moreover, the comparison between the FAPI-FNIRTag and the FAPI-IRDye800CW fluorescence was found to be comparable by two different instrument measurements and dyes solutions. If the data were fitted with a linear regression, the ratio between the slope for FAPI-FNIRTag and FAPI-IRDye800CW is around 3-fold higher. This is not surprising considering the results reported by Luciano and coworkers, who developed FNIRTag to enhance the brightness of bio-conjugates thanks to chemical structure modification at the C4' position (**Figure 5** – adapted from Luciano *et. al*, ACS Chem. Biol. 2019).

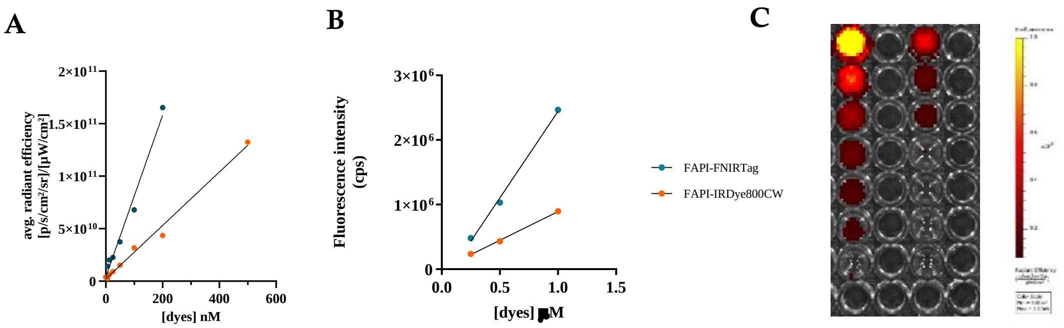

Figure 4 (A) Average radiance efficiency comparison between FAPI-FNIRTag and FAPI-IRDye800CW at different concentrations (IVIS measurements, phantom imaging). (B) Fluorescence emission comparison (cps) between FAPI-FNIRTag and FAPI-IRDye800CW from fluorimeter measurements. (C) Phantom imaging comparison between FAPI-FNIRTag (on the left) and FAPI-IRDye800CW (on the right) (λ_{ex}=740 nm, λ_{em}=790 nm).

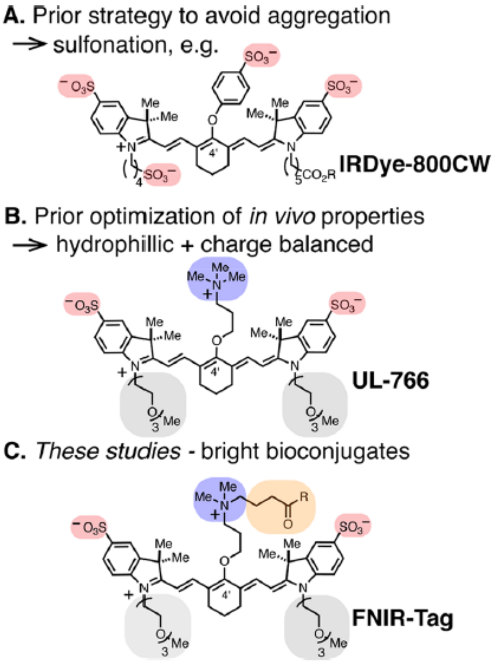

Figure 5 Chemical structure modification to insert a substituted alkyl ether at the C4′ position, that provide exceptionally aggregation-resistant fluorophores (adapted from Luciano *et al.*, ACS Chem. Biol. 2019).

Photo- and Chemical stability

Photostability represents a crucial parameter to verify a potential NIRF imaging probe and it involves diverse but frequently related phenomena. Different and not easily unified definitions have been developed for the photosensitization processes these molecules undergo. Degradations may involve oxygen or not[21], and may be triggered by light exposure or several other factors[20] (albumin exposure, diverse light sources, heat, etc.). The most common degradation processes are outlined in Type I and Type II sensitization reactions, both requiring molecular oxygen (**Scheme 1**)[22].

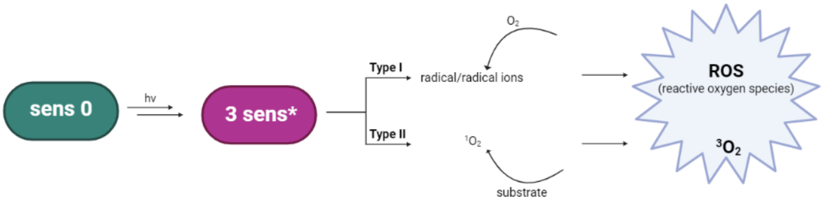

Scheme 1 Definitions of Type I and Type II photosensitized oxidation reactions proposed by Baptista *et al*.

Photobleaching of a heptamethine cyanine dye is primarily caused by a bimolecular reaction of the polyene with photo-generated singlet oxygen (dioxetane intermediate, **Scheme 2**). Moreover, a recent study conducted by Nani and coworkers demonstrated that only exogenously generated $^1O_2$ and no other common ROS, is capable of replicating this reaction pathway and that regioselective cleavage at only two positions of the polyene, C_2/C_1’ and C_2’$/C_3$’ (**Scheme 3**), can be interpreted as being a consequence of the overall energetics of the dioxetane intermediates[23].

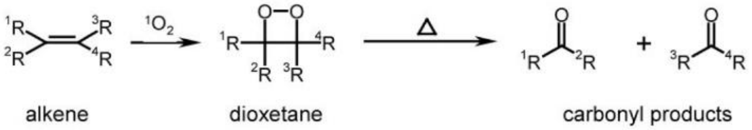

Scheme 2 Proposed decomposition mechanism of cyanine dyes. A general structure of an alkene (double bond in a polymethine chain) is shown, with 1R to 4R representing different functional groups. Adapted from Engel *et al.* [21].

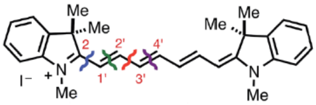

Scheme 3 The four possible cleavage pathways indicated by Nani *et al*. Blue, green, red, and indigo indicate cleavage at C_2/C_1’, C_1’$/C_2$’, C_2’/C3’, and C_3’$/C_4$’ sites, respectively. Adapted from Nani *et al.*[23].

Hence, to monitor the decrement in fluorescence emission during irradiation, measurements were performed, and data were obtained by recording emission measurements and were elaborated by normalizing the fluorescence intensity (S/N) to t=0.

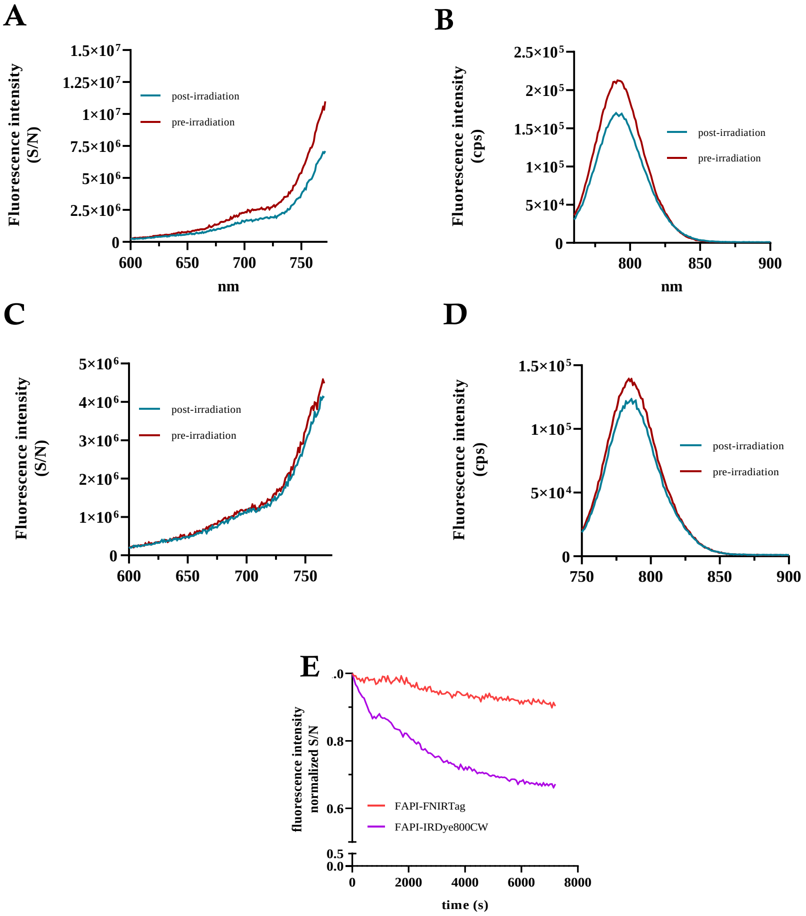

Figure 6 (A) FAPI-IRDYe800CW excitation spectra before and after irradiation. (B) FAPI-IRDYe800CW emission spectra before and after irradiation. (C) FAPI-FNIRTag excitation spectra before and after irradiation. (D) FAPI-FNIRTag emission spectra before and after irradiation. (E) Fluorescence intensity decrement after irradiation (2h, every 60s) for FAPI-FNIRTag and FAPI-IRDye800CW over time.

To check if light irradiation led to excitation and/or emission spectra profiles modification, both spectra were recorded before and after the irradiation process. As shown in **Figures 6A-E**, the two dyes reacted differently to light stimulation. In fact, while FAPI-FNIRTag preserved the 90% of its initial fluorescence, FAPI-IRDye800CW underwent most of the photobleaching in the first part of the irradiation (15% after 49 minutes), approaching the 60% at the end of the experiment. The latter observation could be due to a reduction in singlet oxygen quantum yield for FNIRTag relative to IRDye800CW.

Chemical stability in serum was checked because it has been reported the possible covalent substitution of the 4′-phenoxy group by biological nucleophiles to give undesired dye degradation products[24]. However, the UPLC-MS measurements (**Figures S5** and **S6** in Appendix III) did not reveal any peaks related to degradation products due to C-O bond breaking, as previously reported in literature studies [25]. Certainly, this finding does not ensure the same behavior *in vivo* where this possibility will be carefully evaluated. Although two peaks are found, they both belong to intact compounds, as confirmed from the identical SRM transition. The composition of serum (ionic strength, pH) might have modified the chromatographic retention process, thus leading to a double-peak [26].

Albumin binding

Albumin binding represents a useful parameter to preliminary consider the *in vivo* non-specific uptake and biodistribution of pharmaceuticals. **Figure 7** reports the dependence of the fluorescence intensity on the albumin concentration for the two dyes. From the values observed, it can be inferred that FAPI-IRDye800CW underwent a higher fluorescence enhancement (48% vs 27%) following the albumin interaction. However, by fitting the data with a proper binding isotherm equation, similar K_D constants were obtained, thus indicating that the two compounds do not show a marked difference in terms of albumin-binding strength.

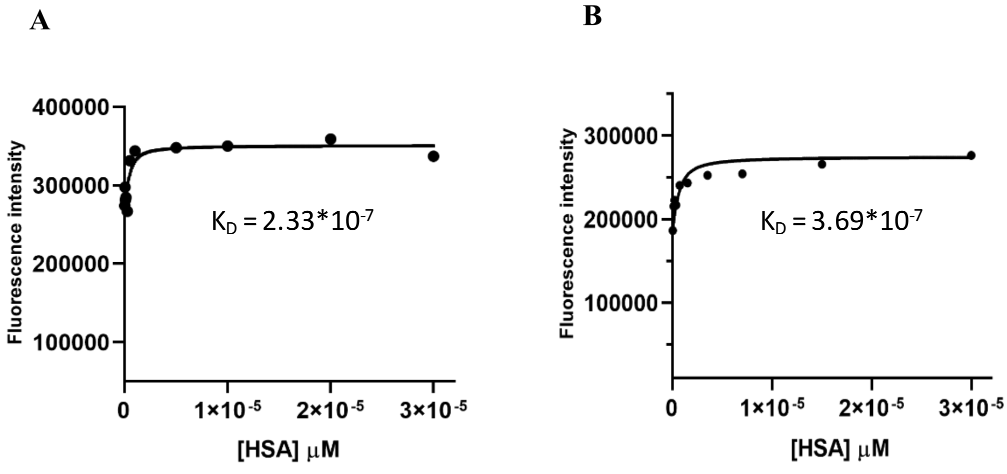

Figure 7 Albumin binding data after 1h-incubation ([dye]=0.15 μM, PBS pH=7.4) at RT. (A) FAPI-FNIRTag (B) FAPI-IRDye800CW.

In vitro uptake on FAP-expressing cells

Recognition of FAP by fluorescent dyes must be confirmed *in vitro* before moving on to preclinical investigation. Although *in vitro* behavior does not always reflect the *in vivo* fate of a probe, it certainly represents a clear starting point. To assess the *in vitro* FAP uptake, transfected cells were employed (a cell line containing a vector, as a plasmid, for the genetic insert) and the empty vector (the same cell line with no genetic insert) was used as control. In **Figure 8** the flow cytometry results as MFI (Mean Fluorescence Intensity) and related histograms were reported. For dot plots see Appendix III (**Figures S8** and **S9**). FAPI-IRDye800CW and FAPI-FNIRTag showed much higher MFI values than the control, indicating a high uptake of both the dyes on FAP-expressing cells. To confirm the target specificity, a blocking experiment was conducted, and the results demonstrated the specificity of the interaction between the dyes and the FAP protein *in vitro*, since the comparable uptake to control. As further confirmation, the uptake on FAP-negative cell lines was in line with the results observed for the control. The difference between MFI values in positive FAP+ cells (green) is due to the different dyes fluorescence.

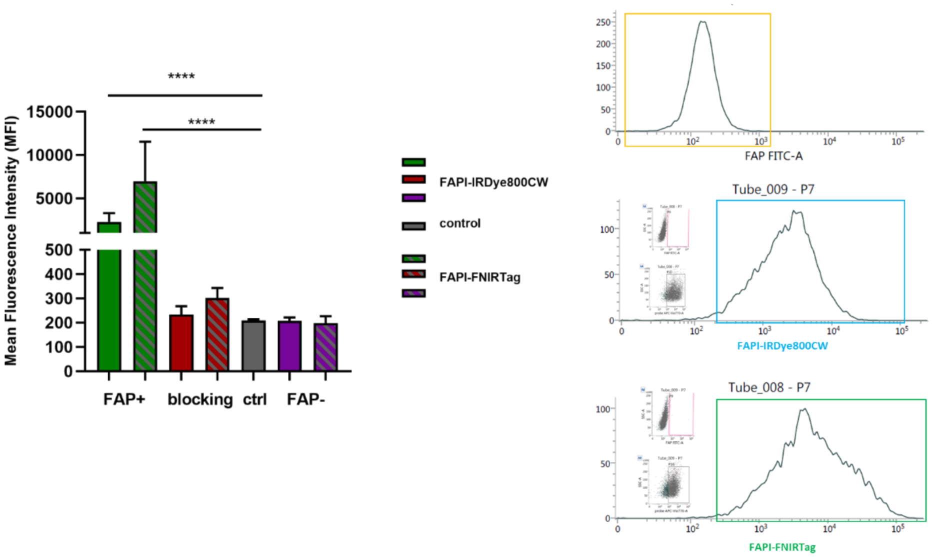

Figure 8 Fluorescence emission on FAP-expressing cells of dyes at 0,5 µM (green), dyes together with 100x excess of competitor (unconjugated FAPI-46) (red), without any dyes (grey), dyes on no-FAP-expressing cells (purple). Patterned histograms showed FAPI-FNIRTag data, monochromatic histograms showed FAPI-IRDye800CW data. Data were shown as means ± SD. **** $p < 0.0001$ (n = 3) *t*-test (α=0,05).

FAP assessment on TUBO tumor specimens by flow cytometry

Preliminary FAP expression investigation on TUBO tumor specimens was addressed by flow cytometry measurements and immunohistochemical staining.

Characterization of cells populations and individuations of FAP-positive cells subpopulations represent a key strategy to deeply understand the crosstalk between FAP and the tumor microenvironment, with beneficial consequences on understanding FAP clinical significance. This thesis does not aim to characterize the tumor model in question in such detail, however, an overview on FAP expression by flow cytometry was performed to provide a general characterization of the model. Being FAP almost ubiquitous, there would need to be a detailed discussion of the different models. This work aimed to test *in vivo* two novel NIRF dyes for breast cancer imaging, then we will focus on breast cancer. It is commonly known that breast cancer cells exhibit intra-tumoral heterogeneity and emerging evidence points toward breast cancer CAFs being equally heterogeneous. It has been shown that human breast tumors contain at least four CAF subpopulations[27], indicating that the heterogeneity of breast cancer CAFs is not limited to experimental cancer models. Venning and coworkers looked at the temporal composition of CAF subpopulations during the development of the breast tumour, by performing orthotopic implantation of syngeneic 4T1 or 4T07[28]. First, their findings showed that FAP^{+}CAF subsets change over time within each tumor type. Regarding FAP, they demonstrated that FAP and CD26 are the most prevalent subpopulations and that FAP change drastically in the first 14 days to then stabilizing (observations at days 7, 14 and 21). Flow cytometry measurements regarding FAP are mainly used for molecular biology to deeply characterize and understand cancer biology. For this reason, the main part of these studies is focused on CAFs population characterization and related subpopulation quantification, with a very few studies on imaging-related FAP quantification on the overall live cells. Basing on these poor examples, the % of FAP (on the live cells) in breast cancer tumor model (4T1, 4T07) settles down at around 1,5-2[28,29] After tumor digestion (See Appendix III for detailed protocol) and antibodies incubation, FACS analysis was performed on cell pellets to quantify FAP. As depicted in **Figure 9A**, the percentage of live cells stained for FAP is equal to 2,3% thus in line with the literature. **Figure 9B** reports a representative dots plot of FAP+ cells subpopulation. Following the same protocol, flow cytometry measurements of FAP abundance were performed after mice euthanasia on excised tumor tissues. Differently from the previous experiments, gating on our probes fluorescence was set up. The results are reported in **Figure 9C** and show a slightly different FAP abundance on overall live cells (**Figure S7**) in comparison to preliminary FAP assessment data (**Figure 9A**).

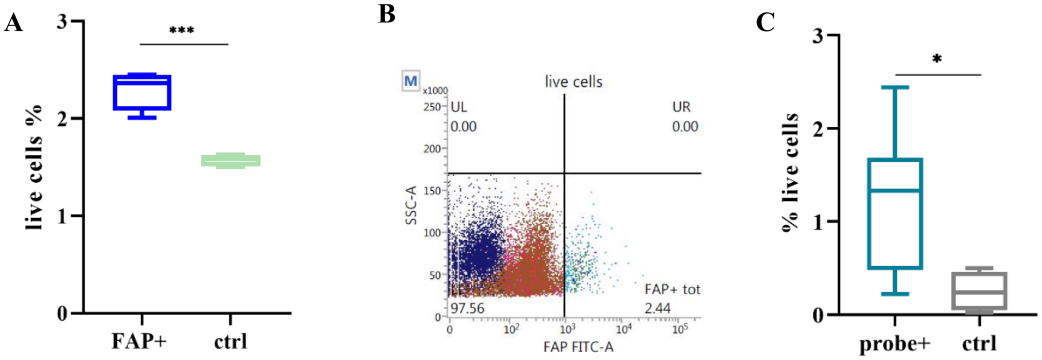

Figure 9 Flow cytometry results of FAP-expressing cells in TUBO tumors. (A) Percentage of FAP-expressing cells on live cells extracted from TUBO tumors in Balb/C mice. (B) Dots plot of TUBO tumor sample (BalB/C mice), gating on live cells. (C) Percentage of probe-positive cells on live cells extracted from TUBO tumors in athymic mice. *** p = 0,0005 (n=4); * p = 0,0372 (n=9); *t*-test (α=0,05).

However, it does not seem accurate to attribute this difference to a mis-quantification through our probes since the different excitation and emission wavelengths employed for FAP-expressing cells in the first case (FITC, λ_{ex}=494 nm, λ_{em}=517nm) perfectly fit the employed secondary antibody (Alexa Fluor 488, λ_{ex}=499 nm λ_{em}=520) while the probe-positive cells extracted after the *ex vivo* biodistribution studies (APC Vio 770, λ_{ex}=652 nm, λ_{em}=775 nm) result from the spectrum tail excitation of our fluorophores (**Table 2**). To better compare this breast cancer tumor model with others already employed in preclinical research (4T1, MDA-231, etc.) further FACS gating are needed, by including different CAFs biomarkers, for example a-SMA or CD26, in order to isolate them and easily compare the obtained results with already published data.

Immunohistochemistry

FAP expression was further verified by means of immunohistochemical staining of tumor tissues. The **Figure 10** reported two representative examples in which it is possible to appreciate the brown signal (DAB) which show the FAP-positive areas.

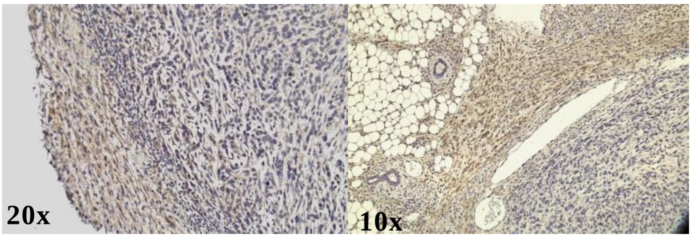

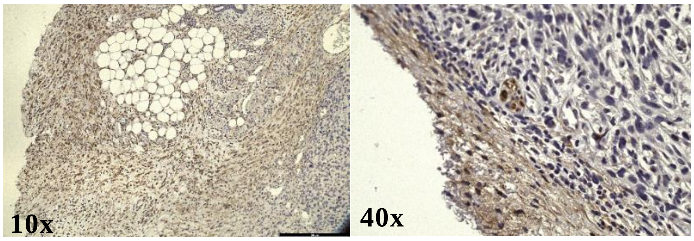

Figure 10 Immunohistochemical staining (anti-FAP) of excised tumor tissues from TUBO tumor-earing Balb/C mice. Brown signals correspond to anti-FAP staining; nuclei were counterstained with hematoxylin.

In vivo NIRF imaging and biodistribution studies

In vivo FAP imaging at preclinical level has been usually explored by means of animal models generated with FAP-transfected cell lines (mainly HT-1080-FAP, fibrosarcoma cell lines) or few other models including glioblastoma (U87) and breast cancer (4T1), but not limited to. In this work, we aimed to explore the *in vivo* imaging application of two NIRF FAP-targeting probes for breast cancer imaging purposes by employing the TUBO cell lines. To the best of our knowledge, this is the first approach to image this type of preclinical model by means of FAP targeting. For this reason, preliminary immunohistochemical evaluation and flow cytometry measurements were performed. After the intravenous injection of 5 nmoles of FAPI-IRDye800CW or FAPI-FNIRTag, NIRF imaging scans were acquired at different time points and ROI analysis was performed on tumor and muscle (background reference) to quantify the average radiance efficiency. **Figure 11** reports the kinetic of tumor (A) and muscle retention (B) within 7 days. The time evolution of the signal in both organs showed the same trend, preventing the observation of a clear tumor retention of the tumour-targeted dyes. Tumor-to-background (TBR) values were calculated at each time point (**Figure 11C**) and the results obtained did not allow to confirm an effective tumour FAP-targeting for both the dyes. To quantify the fluorescence in the main organs and to better understand the elimination kinetic, biodistribution studies were performed at the best imaging time point (24 h post injection), following 5 nmol injection of FAPI-conjugated dyes. After mice euthanasia by cervical dislocation, the main organs (tumor, kidneys, liver, heart, lung, pancreas, intestine, spleen) were excised and fluorescence signal was measured. **Figure 12A** depicts the *ex vivo* fluorescence imaging of the main organs excised, with their average radiance efficiency reported in **Figure 12C**. The data highlighted a clear liver uptake and kidney clearance, with a higher fluorescence measured for most of the organs (except tumour) for the FAPI-FNIRTag dye. As this dye showed *in vitro* a higher fluorescence than FAPI-IRDye800CW (see **Figure 4**), this observation appears consistent with the view that the two dyes share a similar biodistribution. To better clarify the elimination kinetic and blood half-life of the probes, biodistribution studies and blood collection at different time point should be planned. As well as TBR found *in vivo*, TBR values *ex vivo* found to be comparable for the two probes.

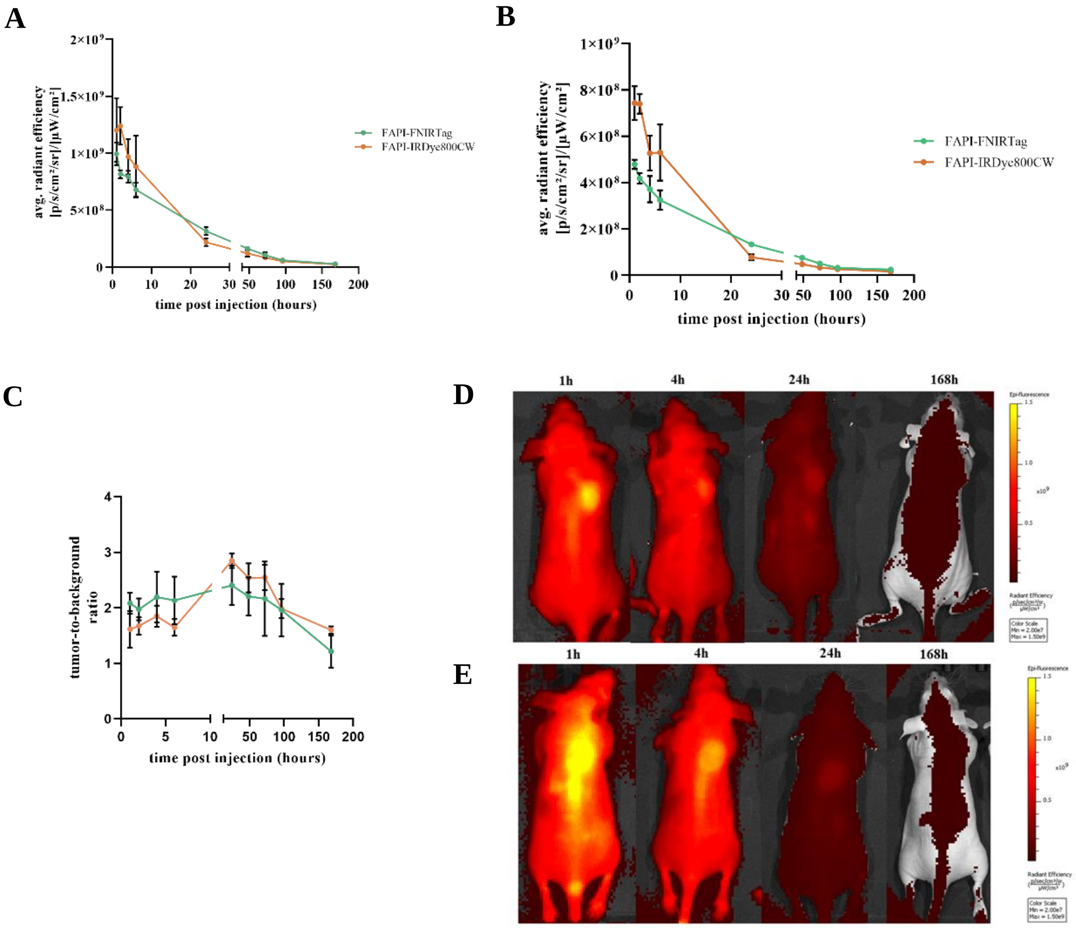

Figure 11 (A) Kinetic of *in vivo* average radiance efficiency found for tumor tissue and for (B) muscle (background). (C) Tumor-to-background ratio. (D) *In vivo* fluorescence imaging of TUBO tumor-bearing mice intravenously injected with 5 nmol of FAPI-FNIRTag. (E) *In vivo* fluorescence imaging of TUBO tumor-bearing mice intravenously injected with 5 nmol of FAPI-IRDye800CW.

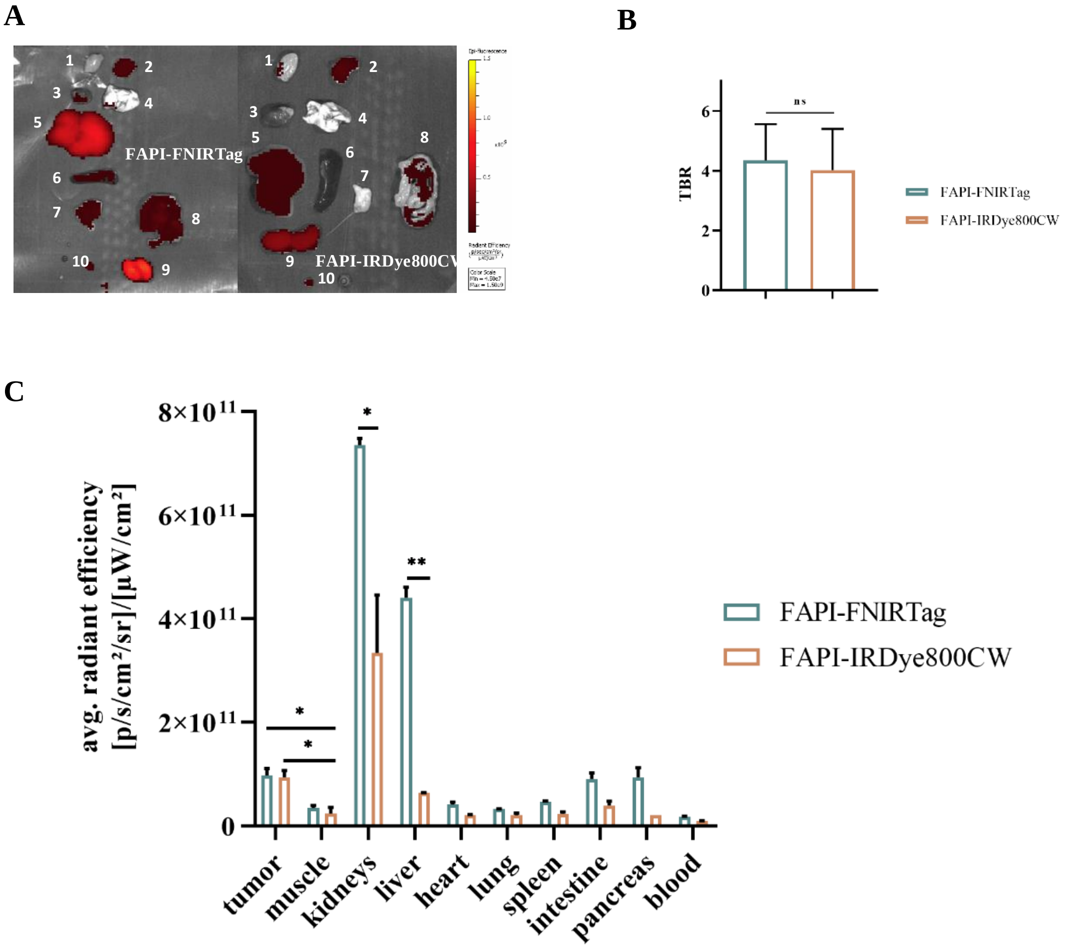

Figure 12 (A) *Ex vivo* fluorescence imaging of main organs excised from TUBO tumor-bearing mice *i.v.* injected with 5 nmol of FAPI-FNIRTag or FAPI-IRDye800CW (1: muscle, 2: tumor, 3: heart, 4: lung, 5: liver, 6: spleen, 7: pancreas, 8: intestine, 9: kidneys, 10: blood). (B) *Ex vivo* tumor-to-background ratio for the two investigated dyes (p=0,5589). (C) Biodistribution for FAPI-FNIRTag and FAPI-IRDye800CW (5 nmol) in TUBO tumor-bearing athymic mice 24 hours post injection. p=0,0161 for FAPI-FNIRTag tumor/muscle; p=0,0127 for FAPI-IRDye800CW tumor/muscle; p=0,0030 for kidneys comparison; p=0,0014 for liver comparison. (*t*-test α=0,05)

CONCLUSIONS

Implementation of diagnostic and intra-operative procedures to overcome the current limitations is still matter of interest in the oncological field. Certain types of cancers, including breast cancer, suffer from high recurrence rates due to incomplete tumor resection. Developing of new imaging probes and investigation of new stromal biomarkers represent a key strategy to examine. This work aimed to develop two novel NIRF imaging probes targeting the fibroblast activation protein for breast cancer management purposes. The two developed NIRF agents were characterized from the optical point of view, *in vitro* on FAP expressing cells and *in vivo* in an unexplored FAP-expressing preclinical tumor model. The conjugation of both the fluorophores with the FAP-inhibitor FAPI-46 did not disregard the expectations on fluorescence performances, since the higher fluorescence emission reported in literature for FNIRTag. The *in vitro* FAP recognition demonstrate that the conjugation of the FAPI-46-like inhibitor did not impact on FAP specificity. Regarding albumin binding and *in vivo* imaging studies, the results were not as expected. FNIRTag development started from the statement that IRDye800CW lead to a higher aspecific signal *in vivo*, also due to the higher albumin binding. Our albumin binding results did not highlight differences between the two probes in terms of binding strength and the obtained results *in vivo* did not indicate FNIRTag-conjugate as the most performing one in terms of higher TBR as expected. Some criticisms regarding FAP in preclinical models need to be pointed out. First, FAP imaging finds its main application in Positron Emission Tomography, imaging technique characterized by almost absent background signal while fluorescence imaging, although using NIRF fluorophores, suffer from some background signal. This aspect could influence the TBR values by using FAP-inhibitor targeting moiety. Moreover, it’s extremely difficult to compare our results with literature studies because of lack of NIRF imaging studies for targeting FAP. Basing on these conclusions, binding specificity need to be clarified. Given the ubiquity of FAP protein, another difficulty is represented by the impossibility to find a true “negative” FAP-negative tumor model. As an alternative, blocking experiments could be performed by co-inject an excess of competitor, being aware that it might be difficult to get a different signal given the low starting TBR. Further strategy to consider may involve a different FAP-inhibitor targeting moiety or a different FAP-targeting strategy such as peptides.

APPENDIX III

UPLC-UV/Vis-MS

The chromatographic runs were performed using an Acquity UPLC BEH C18 (130Å, 1.7 µm, 2.1 mm x 50 mm) column. The column oven was maintained at 25°C and the elution solvents were water/trifluoroacetic acid 0.1% (solvent A) and acetonitrile/trifluoroacetic acid 0.1% (solvent B) for FNIR-Tag and ammonium acetate 7mM (solvent A) and acetonitrile/trifluoroacetic acid 0.1% (solvent B) for IRDye800CW. The two different gradients were listed below in Table S1.

FAPI-IRDye800CW

t (min)	%A	%B
0	90	10
12	50	50
14	0	100

FAPI-FNIRTag

t (min)	%A	%B
0	95	5
11	60	40
14	0	100

Table S1 Gradients used for reversed-phase analytical runs of NH-FAPI-46 fluorescent conjugates.

The flow rate was 0.4 mL/min. The Waters Mass Detector was operated with an electrospray ion source in positive ion mode with a cone voltage of 20V. The intervals of mass scan were 50–1250 m/z. MS ions found were list below in Table S2. The chromatograms were reported in Figure S1.

	FAPI-IRDye800CW	FAPI-FNIRTag
$[M-H]^+$	-	-
$[M-2H]^+$	742.75	771.85
$[M-3H]^+$	-	514.95

Table S2 MS ions found for synthetized products.

UV/Vis spectra was recorded at 214 and 700 nm. The reported UV/Vis spectra (Figure S1) was recorded at 700 nm. The preparative chromatographic runs were performed on a AKTA Purifier System. XBridge Prep BEH300 column was used for IRDye800CW (A=ammonium acetate 7mM, B=CH_3CN) and FNIR-Tag conjugates purification (A=H_2O+TFA 0.1%, B=CH_3CN); the two different gradients were listed below in Table S3.

FAPI-IRDye800CW

t (min)	%A	%B
0	90	10
13	50	50
14	0	100

FAPI-FNIRTag

t (min)	%A	%B	
0	90	10	
2	90	10	
9	72	28	
15	72	28	
18	0	100	

Table S3 Gradients used for reversed-phase preparative runs.

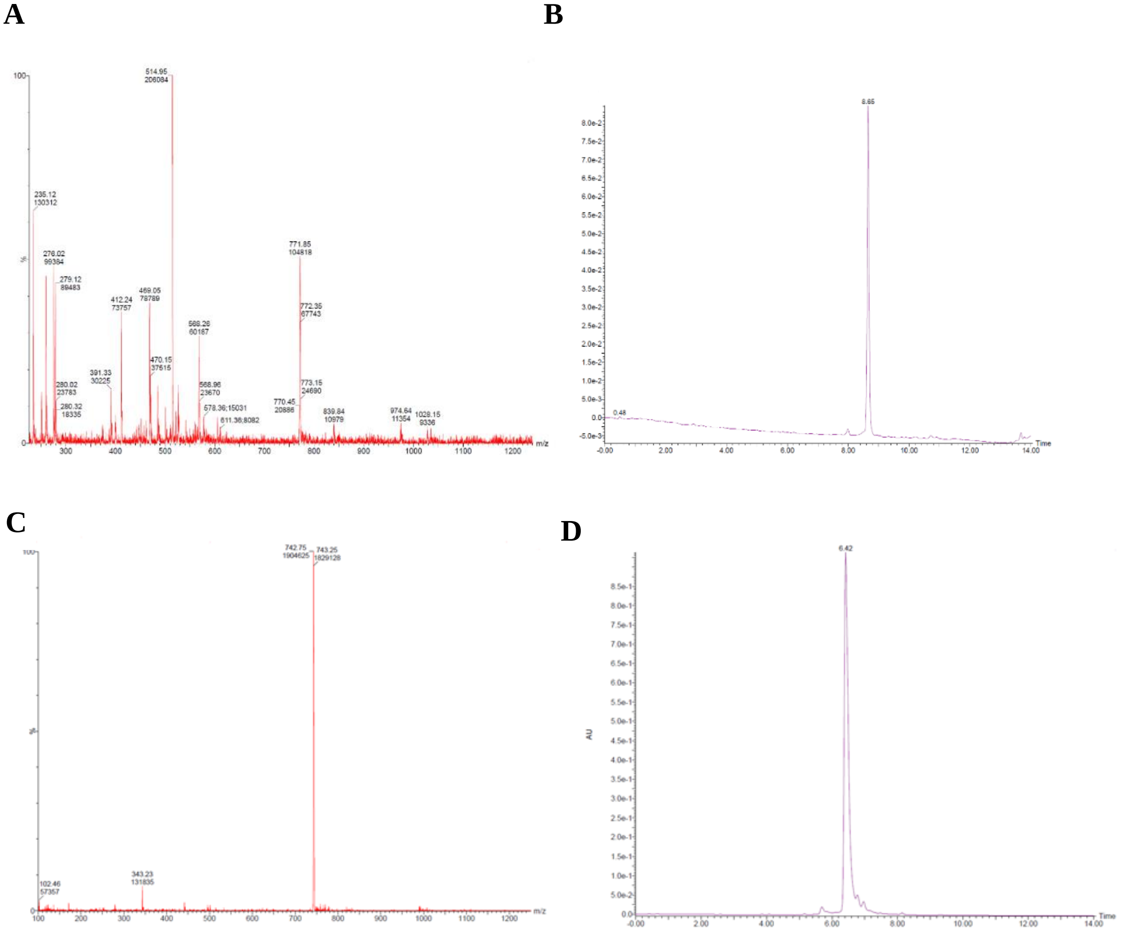

Figure S1 ESI-MS spectrum of (A) FAPI-FNIRTag, $[M\text{-}2H]^{2+} = 771.85$ m/z, $[M\text{-}3H]^{3+} = 514.95$ and (C) FAPI-IRDye800CW, $[M\text{-}2H]^{2+} = 742.75$ m/z. (B) UPLC-UV/Vis spectrum at 700 nm of FAPI-FNIRTag (purity > 99%) and (D) FAPI-IRDye800CW (purity% > 99%).

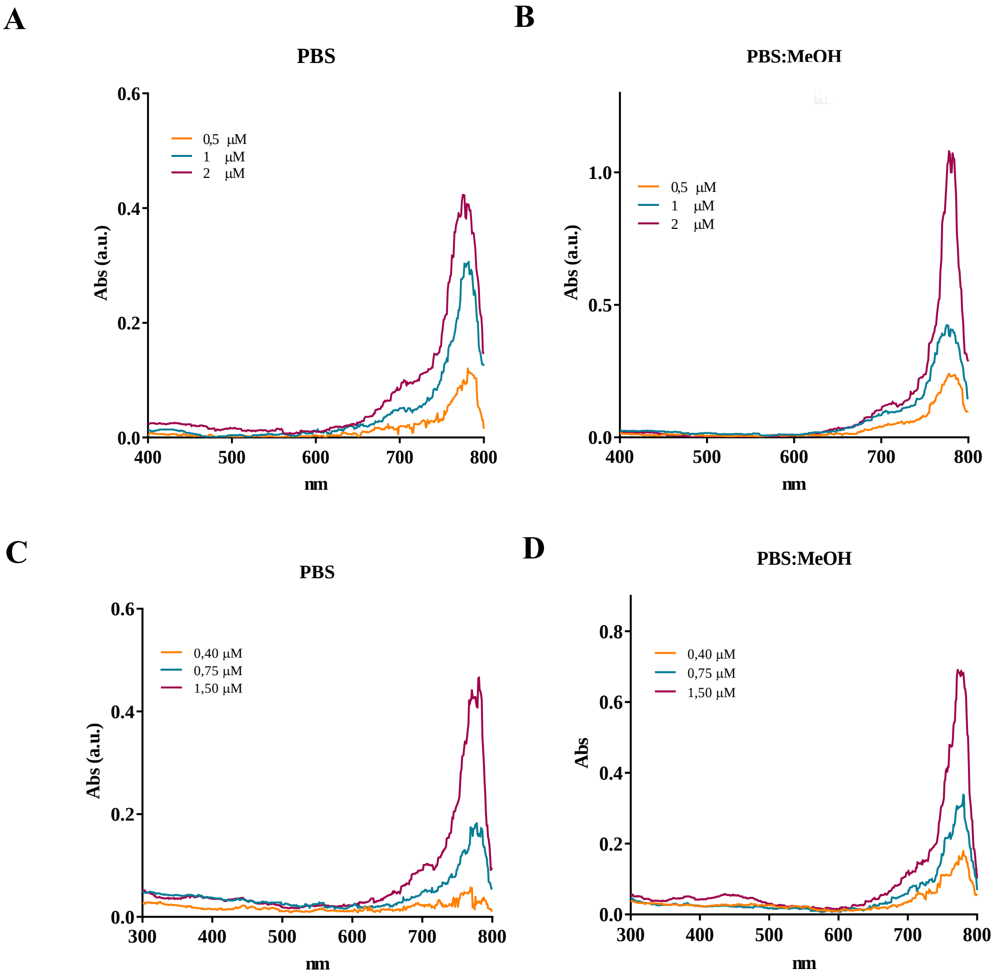

Figure S2 (A) Absorbance spectra of FAPI-IRDye800CW in PBS pH=7.4. **(B)** Absorbance spectra of FAPI-IRDye800CW in PBS:MeOH (1:1). **(C)** Absorbance spectra of FAPI-FNIRTag in PBS pH=7.4. **(D)** Absorbance spectra of FAPI-FNIRTag in PBS:MeOH (1:1).

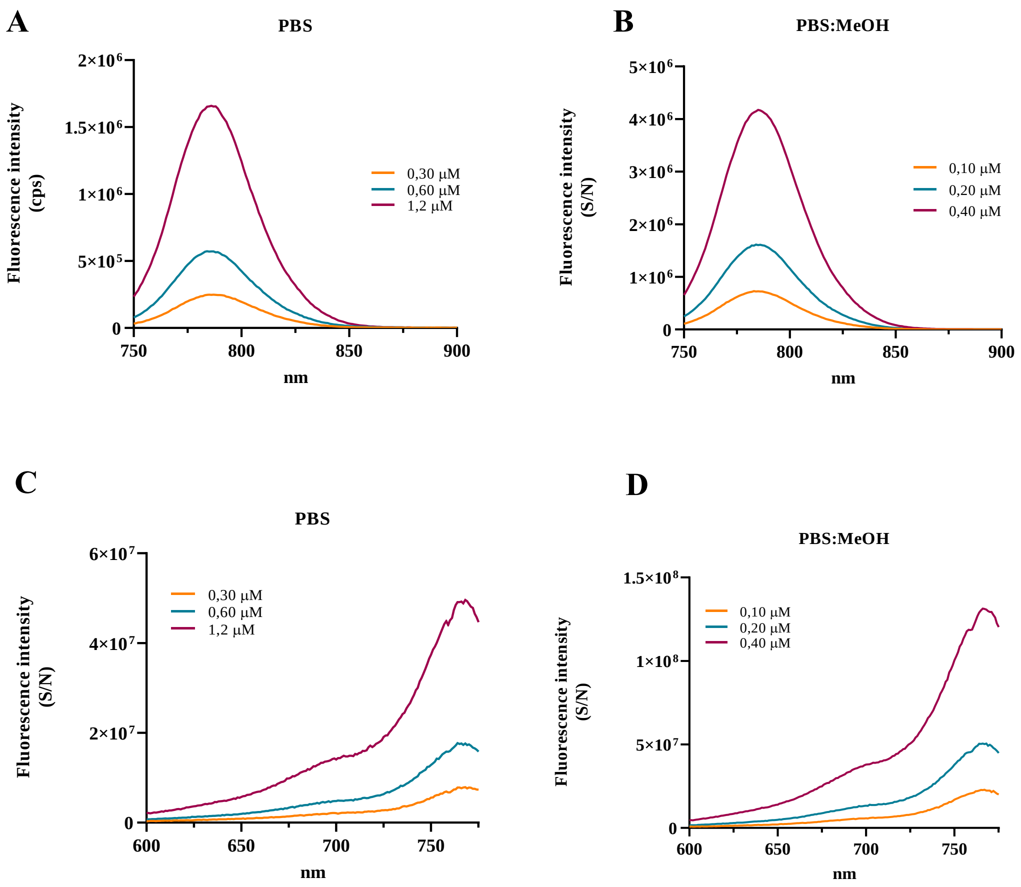

Figure S3 (A) Fluorescence emission spectra of FAPI-FNIRTag in PBS pH=7.4. **(B)** Fluorescence emission spectra of FAPI-FNIRTag in PBS:MeOH (1:1). **(C)** Fluorescence excitation spectra of FAPI-FNIRTag in PBS pH=7.4. **(D)** Fluorescence excitation spectra of FAPI-FNIRTag in PBS:MeOH.

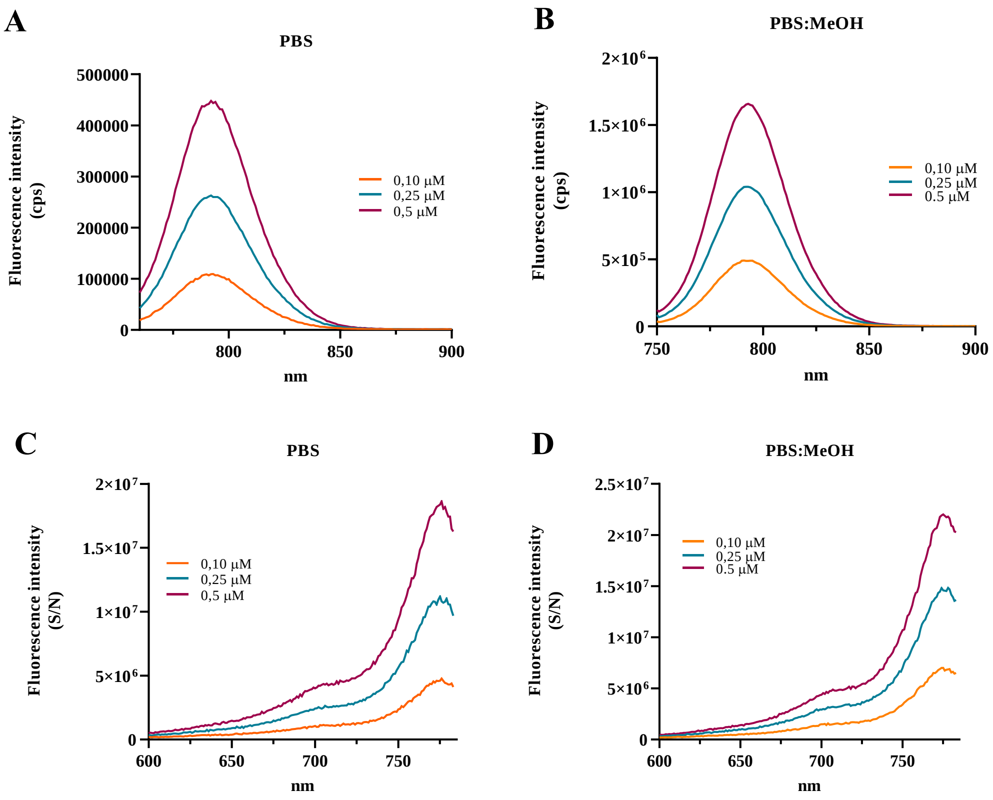

Figure S4 **(A)** Fluorescence emission spectra of FAPI-IRDye800CW in PBS pH=7.4. **(B)** Fluorescence emission spectra of FAPI-IRDye800CW in PBS:MeOH (1:1). **(C)** Fluorescence excitation spectra of FAPI-IRDye800CW in PBS pH=7.4. **(D)** Fluorescence excitation spectra of FAPI-IRDye800CW in PBS:MeOH.

Serum stability

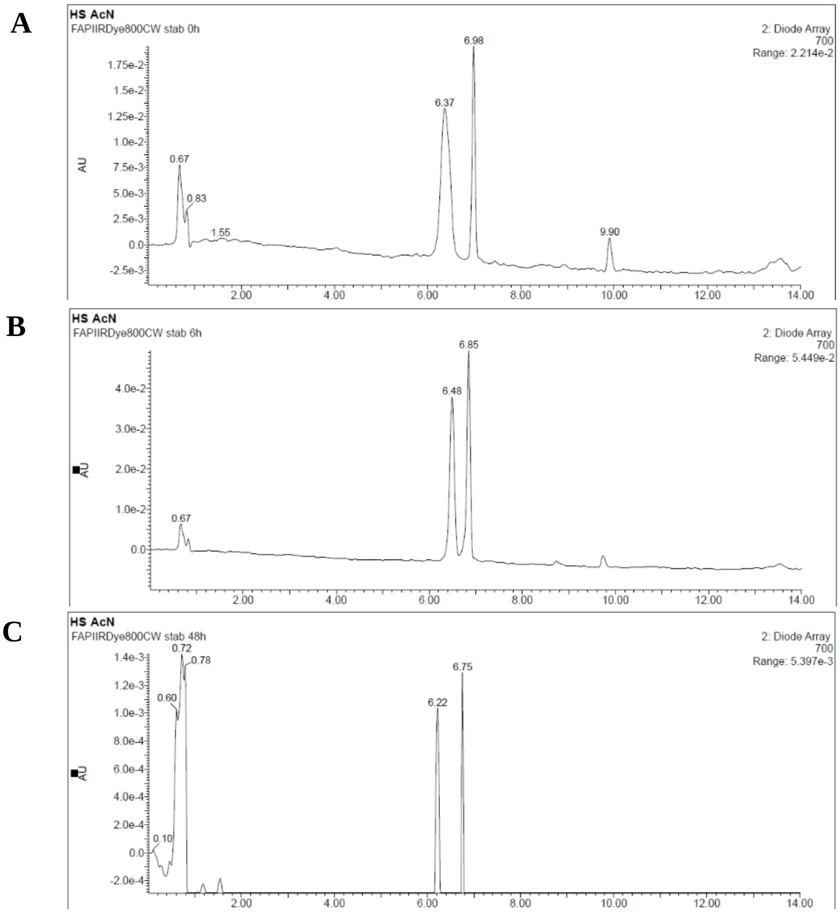

Figure S5 UPLC-UV/Vis spectrum at 700 nm of FAPI-IRDye800CW after 0, 6 and 48h incubation with human serum at 37°C. MS analysis of peak at lower retention time revealed the same mass pattern of product, hence no degradation was found. It is possible to attribute this peak to a matrix effect of the human serum on retention process (ions, pH).

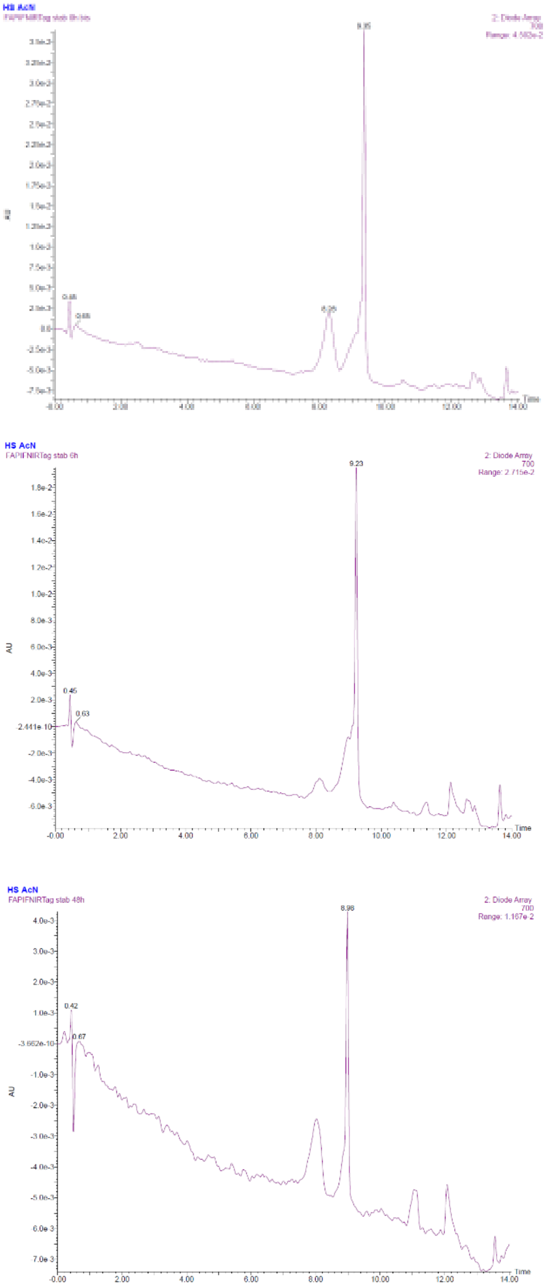

Figure S6 UPLC-UV/Vis spectrum at 700 nm of FAPI-FNIRTag after 0, 6 and 48h incubation with human serum at 37°C. MS analysis of peak at lower retention time revealed the same mass pattern of product, hence no degradation was found. It is possible to attribute this peak to a matrix effect of the human serum on retention process (ions, pH).

Preclinical model identification

Tumor digestion and flow cytometry

Anesthetized mice were sacrificed at day 35 through cervical dislocation. Tumor tissues were excised and divided into two parts to perform both flow cytometry analysis and immunohistochemical staining. For flow cytometry analysis, mushed tumor tissues were digested in DMEM added with dispase 3mg/ml (D4693 – Sigma Aldrich) and collagenase 1mg/ml (C0130 – Sigma Aldrich). Suspension was vortexed in orbital shaker for 30 minutes at 37°C, filtered with cell strainer (70 µm) and centrifuged (10 minutes, 1400 rpm). $1*10^6$ cells were pelleted for each condition tested. Incubation with anti-FAP primary antibody (1h at 4°C) was performed. After washing with PBS, secondary antibody was incubated for 30 minutes at 4°C.

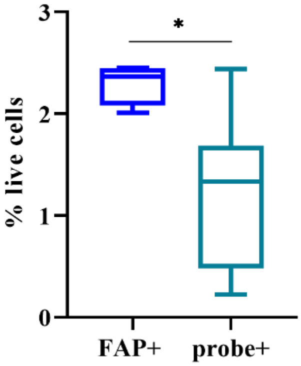

Figure S7 *t*-test performed on flow cytometry results between FAP-expressing cells extracted from TUBO tumors in Balb/C mice and probe-positive cells extracted from TUBO tumors in athymic mice. p = 0,0130 (α=0,05).

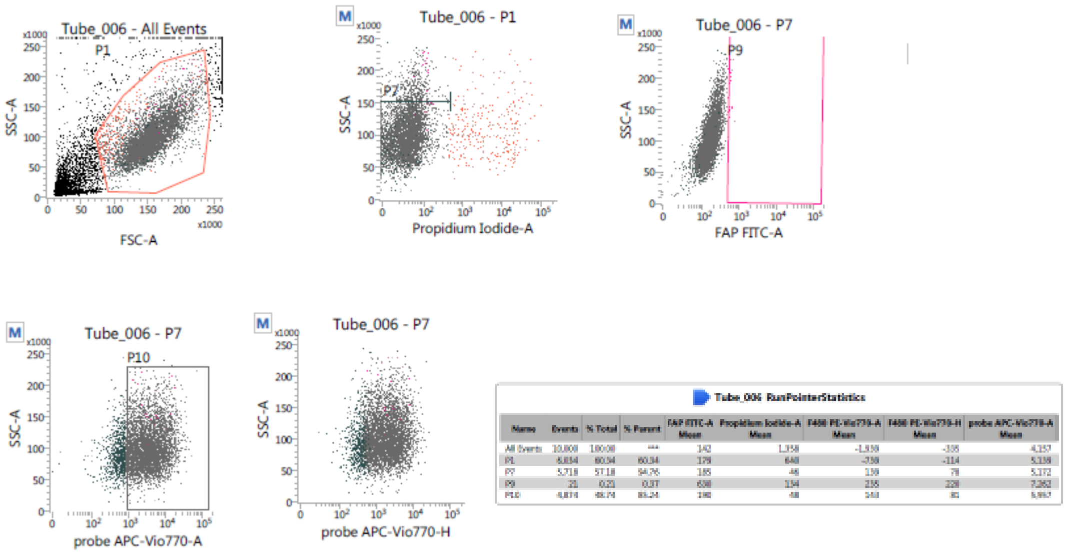

Tube_006 RunPointerStatistics

Name	Events	% Total	% Parent	FAP FITC-A Mean	Propidium Iodide-A Mean	F480 PE-Vio770-A Mean	F480 PE-Vio770-H Mean	probe APC-Vio770-A Mean
All Events	10,000	100.00	***	142	1,358	-1,359	-335	4,157
P1	6,034	60.34	60.34	179	640	-738	-114	5,138
P7	5,718	57.18	94.76	185	46	138	78	5,172
P9	21	0.21	0.37	608	134	235	228	7,262
P10	4,874	48.74	85.24	190	48	168	81	5,997

Figure S8 Flow cytometry results for FAPI-FNIRTag uptake on FAP-expressing cells (HEK293T-FAP) as dot plots.

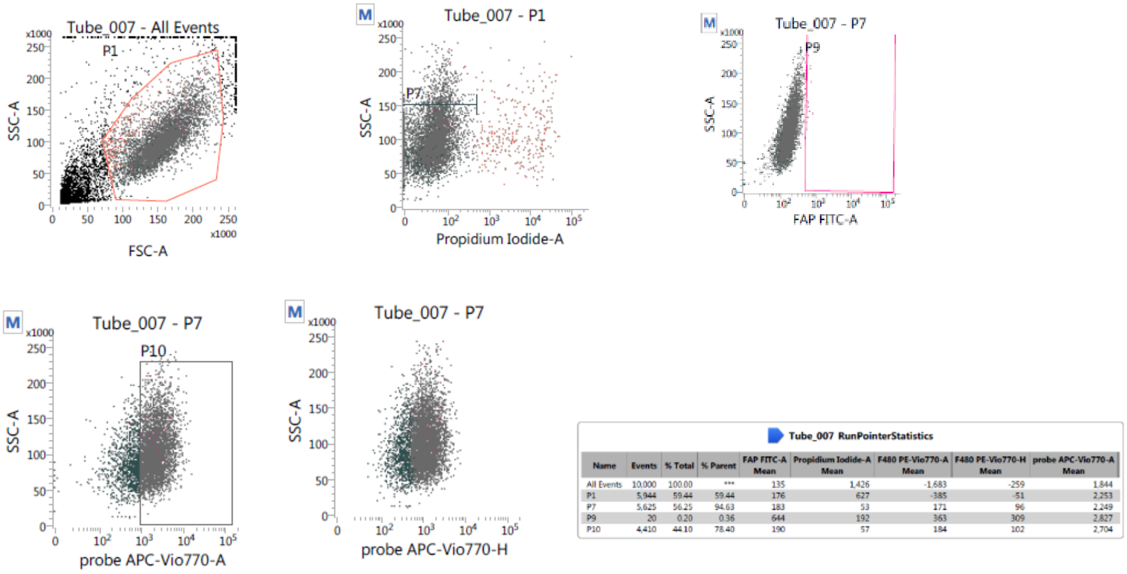

Tube_007 RunPointerStatistics

Name	Events	% Total	% Parent	FAP FITC-A Mean	Propidium Iodide-A Mean	F480 PE-Vio770-A Mean	F480 PE-Vio770-H Mean	probe APC-Vio770-A Mean
All Events	10,000	100.00	***	135	1,426	-1,683	-259	1,844
P1	5,944	59.44	59.44	176	627	-385	-51	2,253
P7	5,625	56.25	94.63	183	53	171	96	2,249
P9	20	0.20	0.36	644	192	363	309	2,827
P10	4,410	44.10	78.40	190	57	184	102	2,704

Figure S9 Flow cytometry results for FAPI-IRDye800CW uptake on FAP-expressing cells (HEK293T-FAP) as dot plots.

References

[1] L. Xin, J. Gao, Z. Zheng, Y. Chen, S. Lv, Z. Zhao, C. Yu, X. Yang, R. Zhang, Fibroblast Activation Protein-α as a Target in the Bench-to-Bedside Diagnosis and Treatment of Tumors: A Narrative Review, Front. Oncol. 11 (2021).

[2] J. Calais, FAP: The next billion dollar nuclear theranostics target?, J. Nucl. Med. 61 (2020) 163–165.

[3] X. Hua, L. Yu, X. Huang, Z. Liao, Q. Xian, Expression and role of fibroblast activation protein-alpha in microinvasive breast carcinoma, Diagn. Pathol. 6 (2011) 1–7.

[4] C. Kratochwil, P. Flechsig, T. Lindner, L. Abderrahim, A. Altmann, W. Mier, S. Adeberg, H. Rathke, M. Röhrich, H. Winter, P.K. Plinkert, F. Marme, M. Lang, H.U. Kauczor, D. Jäger, J. Debus, U. Haberkorn, F.L. Giesel, 68Ga-FAPI PET/CT: Tracer uptake in 28 different kinds of cancer, J. Nucl. Med. 60 (2019) 801–805.

[5] T.P. Sandberg, M.P.M.E. Stuart, J. Oosting, R.A.E.M. Tollenaar, C.F.M. Sier, W.E. Mesker, Increased expression of cancer-associated fibroblast markers at the invasive front and its association with tumor-stroma ratio in colorectal cancer, BMC Cancer. 19 (2019) 1–9.

[6] D.N. Dorst, E.M.M. Smeets, C. Klein, C. Frielink, D. Geijs, M. Trajkovic-Arsic, P.F.Y. Cheung, M.W.J. Stommel, M. Gotthardt, J.T. Siveke, E.H.J.G. Aarntzen, S.A.M. Van Lith, Fibroblast Activation Protein-Targeted Photodynamic Therapy of Cancer-Associated Fibroblasts in Murine Models for Pancreatic Ductal Adenocarcinoma, (2023).

[7] C.J.H. van de Vahrmeijer, Alexander L., Merlijn Hutteman, Joost R. van der Vorst, and J.V.F. Velde, Image-guided cancer surgery using near-infrared fluorescence, Nat. Rev. Clin. Oncol. 10 (2014) 507–518.

[8] R.G. Pleijhuis, M. Graafland, J. De Vries, J. Bart, J.S. De Jong, G.M. Van Dam, Obtaining adequate surgical margins in breast-conserving therapy for patients with early-stage breast cancer: Current modalities and future directions, Ann. Surg. Oncol. 16 (2009) 2717–2730.

[9] M. Kedrzycki, M. Leiloglou, P. Thiruchelvam, D. Elson, D. Leff, Fluorescence guided surgery in breast cancer: A systematic review of the literature, Eur. J. Surg. Oncol. 47 (2021) e309.

[10] J. Pauli, M. Grabolle, R. Brehm, M. Spieles, F.M. Hamann, M. Wenzel, I. Hilger, U. Resch-Genger, Suitable labels for molecular imaging - Influence of dye structure and hydrophilicity on the spectroscopic properties of IgG conjugates, Bioconjug. Chem. 22 (2011) 1298–1308.

[11] J.L. Kovar, M.A. Simpson, A. Schutz-Geschwender, D.M. Olive, A systematic approach to the development of fluorescent contrast agents for optical imaging of mouse cancer models, Anal. Biochem. 367 (2007) 1–12.

[12] S.L. Slania, D. Das, A. Lisok, Y. Du, Z. Jiang, R.C. Mease, S.P. Rowe, S. Nimmagadda, X. Yang, M.G. Pomper, Imaging of Fibroblast Activation Protein in Cancer Xenografts Using Novel (4-Quinolinoyl)-glycyl-2-cyanopyrrolidine-Based Small Molecules, J. Med. Chem. 64 (2021) 4059–4070.

[13] J. Roy, S.U. Hettiarachchi, M. Kaake, R. Mukkamala, P.S. Low, Design and validation of fibroblast activation protein alpha targeted imaging and therapeutic agents, Theranostics. 10

(2020) 5778–5789.

[14] R. Mukkamala, S.D. Lindeman, K.A. Kragness, I. Shahriar, M. Srinivasarao, P.S. Low, Design and characterization of fibroblast activation protein targeted pan-cancer imaging agent for fluorescence-guided surgery of solid tumors, J. Mater. Chem. B. 10 (2022) 2038–2046.

[15] A. Loktev, T. Lindner, E.M. Burger, A. Altmann, F. Giesel, C. Kratochwil, J. Debus, F. Marmé, D. Jäger, W. Mier, U. Haberkorn, Development of fibroblast activation protein-targeted radiotracers with improved tumor retention, J. Nucl. Med. 60 (2019) 1421–1429.

[16] M.P. Luciano, S.N. Crooke, S. Nourian, I. Dingle, R.R. Nani, G. Kline, N.L. Patel, C.M. Robinson, S. Difilippantonio, J.D. Kalen, M.G. Finn, M.J. Schnermann, A Nonaggregating Heptamethine Cyanine for Building Brighter Labeled Biomolecules, ACS Chem. Biol. 14 (2019) 934–940.

[17] S.M. Usama, E.R. Thapaliya, M.P. Luciano, M.J. Schnermann, Not so innocent: Impact of fluorophore chemistry on the in vivo properties of bioconjugates, Curr. Opin. Chem. Biol. 63 (2021) 38–45.

[18] S. Gadde, E.K. Batchelor, A.E. Kaifer, Controlling the formation of cyanine dye H- and J-aggregates with cucurbituril hosts in the presence of anionic polyelectrolytes, Chem. - A Eur. J. 15 (2009) 6025–6031.

[19] A. Jafari, A. Ghanadzadeh, H. Tajalli, M. Yeganeh, M. Moghadam, Electronic absorption spectra of cresyl violet acetate in anisotropic and isotropic solvents, Spectrochim. Acta - Part A Mol. Biomol. Spectrosc. 66 (2007) 717–725.

[20] E.D. Clutter, L.L. Chen, R.R. Wang, Role of photobleaching process of indocyanine green for killing neuroblastoma cells, Biochem. Biophys. Res. Commun. 589 (2022) 254–259.

[21] E. Engel, R. Schraml, T. Maisch, K. Kobuch, B. Konig, R.M. Szeimies, J. Hillenkamp, W. Baümler, R. Vasold, Light-induced decomposition of indocyanine green, Investig. Ophthalmol. Vis. Sci. 49 (2008) 1777–1783.

[22] M.S. Baptista, J. Cadet, P. Di Mascio, A.A. Ghogare, A. Greer, M.R. Hamblin, C. Lorente, S.C. Nunez, M.S. Ribeiro, A.H. Thomas, M. Vignoni, T.M. Yoshimura, Type I and Type II Photosensitized Oxidation Reactions: Guidelines and Mechanistic Pathways, Photochem. Photobiol. 93 (2017) 912–919.

[23] R.R. Nani, J.A. Kelley, J. Ivanic, M.J. Schnermann, Reactive species involved in the regioselective photooxidation of heptamethine cyanines, Chem. Sci. 6 (2015) 6556–6563.

[24] D.H. Li, C.L. Schreiber, B.D. Smith, Sterically Shielded Heptamethine Cyanine Dyes for Bioconjugation and High Performance Near-Infrared Fluorescence Imaging, Angew. Chemie - Int. Ed. 59 (2020) 12154–12161.

[25] V.G. Bandi, M.P. Luciano, M. Saccomano, N.L. Patel, T.S. Bischof, J.G.P. Lingg, P.T. Tsrunchev, M.N. Nix, B. Ruehle, C. Sanders, L. Riffle, C.M. Robinson, S. Difilippantonio, J.D. Kalen, U. Resch-Genger, J. Ivanic, O.T. Bruns, M.J. Schnermann, Targeted multicolor in vivo imaging over 1,000 nm enabled by nonamethine cyanines, Nat. Methods. 19 (2022) 353–358.

[26] S.H. Chang, C.C. Chang, L.J. Wang, W.C. Chen, S.Y. Fan, C.Z. Zang, Y.H. Hsu, M.C. Lin, S.H. Tseng, D.Y. Wang, A multi-analyte lc-ms/ms method for screening and quantification of nitrosamines in sartans, J. Food Drug Anal. 28 (2020) 292–301.

[27] A. Costa, Y. Kieffer, A. Scholer-Dahirel, F. Pelon, B. Bourachot, M. Cardon, P. Sirven, I. Magagna, L. Fuhrmann, C. Bernard, C. Bonneau, M. Kondratova, I. Kuperstein, A. Zinovyev, A.M. Givel, M.C. Parrini, V. Soumelis, A. Vincent-Salomon, F. Mechta-Grigoriou, Fibroblast Heterogeneity and Immunosuppressive Environment in Human Breast Cancer, Cancer Cell. 33 (2018) 463-479.e10.

[28] F.A. Venning, K.W. Zornhagen, L. Wullkopf, J. Sjölund, C. Rodriguez-Cupello, P. Kjellman, M. Morsing, M.C. Hajkarim, K.J. Won, J.T. Erler, C.D. Madsen, Deciphering the temporal heterogeneity of cancer-associated fibroblast subpopulations in breast cancer, J. Exp. Clin. Cancer Res. 40 (2021) 1–21.

[29] J. Jin, J.D. Barnett, B. Krishnamachary, Y. Mironchik, C.K. Luo, H. Kobayashi, Z.M. Bhujwalla, Evaluating near-infrared photoimmunotherapy for targeting fibroblast activation protein-α expressing cells in vitro and in vivo, Cancer Sci. 114 (2023) 236–246.

GENERAL CONCLUSIONS

The definition of Molecular Imaging by the Society of Nuclear Medicine and Molecular Imaging gives an insight on the huge progress scientists have made over the past two decades in allied fields, such as chemistry, physics, biology, medicine, engineering, and many others. Although initially focused on Nuclear Medicine, Molecular Imaging expansion to other imaging modalities (Optical Imaging, Magnetic Resonance Imaging, Computed Tomography) has been greatly accelerated. The development of cancer-targeted diagnostic agents is a tridimensional problem since the implication of the affinity (more precisely K_d/B_{max}), biodistribution/clearance and effect size. Then, optimizing a contrast agent or radiotracer in all three dimensions is extremely challenging and represents one of the major issues in advancing in cancer imaging performances.

This doctoral thesis investigated the Molecular Imaging potentialities by developing three imaging probes for Computed Tomography (Chapter 1), Positron Emission Tomography (Chapter 2) and Fluorescence Imaging (Chapter 3).

Computed Tomography is the youngest Molecular Imaging technique; in **Chapter 1** we focused on the development of a bismuth-based small molecule as CT contrast agent. In Molecular Imaging field, nanoparticle systems take over the field. Although these systems show outstanding imaging performances, they involve plenty of criticisms that have to be managed. Hence, the investigation of novel potential imaging system continues to be of great interest. Both the *in vitro* (phantom imaging) and *in vivo* (healthy mice) imaging performances have been investigated, besides proofing the *in vitro* (toxicity in cell culture, stability in different media) and *in vivo* (damaging effect in main organs) safety of the developed tracer. The achieved results may serve as basis for future bismuth-based molecular imaging tracer. Thus, having found promising imaging contrast capabilities as potential kidneys contrast applications, further investigations in that direction are needed to test the imaging contrast performances with an impaired kidney system.

In **Chapter 2**, the development of a novel FAP-targeting PET probe was discussed. The probe was developed by substituting the DOTA chelator of the already developed FAPI-46 with the AAZTA chelator, achieving a high-yield mild protocol for the production of a new gallium-68 PET tracer. The improvement in the labelling procedure in terms of feasibility did not affect the *in vitro* FAP recognition of FAP protein by FAP-inhibitor FAPI-46 like, confirming the affinity in the nanomolar range, as well as the internalization rates. Furthermore, the introduction of the AAZTA chelator might lead to potential theranostic applications of the tracer, by labelling it with therapeutic radioisotopes as ^{177}Lu. Giving the high clinical impact of FAPi radiopharmaceuticals, the preclinical validation of the probe will be pivotal. Hence, the clear advantages achieved with the ambient-temperature and fast radiolabelling procedure, should preserve the optimal *in vivo* biodistribution of FAPI-46 PET agent.

By conjugating two different heptamethine cyanines to the same FAP-inhibitor FAPI-46-like, the development of two novel NIRF probes for fluorescence imaging and fluorescence guided surgery has been discussed in **Chapter 3**. As well as for the previously cited PET tracer, the conjugation of both the fluorophores with the FAP-inhibitor FAPI-46-like, did not impact the *in vitro* FAP-inhibitor binding properties. The *in vivo* fluorescence imaging performances were investigated in breast tumor-bearing mice, achieving modest results in terms of tumor-to-background ratio. As mentioned before, the development of a contrast agent able to improve both tumor enhancement and clearance from the organism is extremely challenging and did not require simply a conjugation between the targeting mojety and the detecting part. Further investigations are needed to improve the imaging performances of those tracer in terms of pharmacokinetic and tumor-to-background ratio.

As a general conclusion, this thesis shows the Molecular Imaging potentiality as a teamwork: each single imaging technique may lead to an improvement in imaging management, both for diagnosis, surgery, and therapy follow-up purposes.